Scholars' Mine

Doctoral Dissertations   Student Theses and Dissertations

Spring 2019

Modeling and simulation of micro/nano-rod distribution in micro channel flows

Saman Monjezi

Recommended Citation

MODELING AND SIMULATION OF MICRO/NANO-ROD DISTRIBUTION IN

MICRO CHANNEL FLOWS

by

SAMAN MONJEZI

A DISSERTATION

Presented to the Faculty of the Graduate School of the

MISSOURI UNIVERSITY OF SCIENCE AND TECHNOLOGY

In Partial Fulfillment of the Requirements for the Degree

DOCTOR OF PHILOSOPHY

in

CHEMICAL ENGINEERING

2019

Approved by:

Joontaek Park, Advisor
Parthasakha Neogi
Jee-Ching Wang
Dipak Barua
Cheng Wang

PUBLICATION DISSERTATION OPTION

This dissertation has been prepared using the Publication Option.

Paper I, "The Effect of Weak Confinement on the Orientation of Nanorods under Shear Flows," was published in Nanomaterials and can be found on pages 8-40.

Paper II, "A Model for the Depletion Layer Prediction in a Dilute Suspension of Rigid Rod-like Particles under Shear Flows in the Entire Range of Peclet Numbers," was published in Chemical Engineering Science and can be found on pages 41-57.

Paper III, "The Shape Effect on The Retention Behaviors of Ellipsoidal Particles in Field-Flow Fractionation: Theoretical Model Derivation Considering the Steric-Entropic Mode," was submitted to Journal of Chromatography A and can be found on pages 58-84.

Paper IV, "Computational Studies of DNA Separations in Micro-Fabricated Devices: Review of General Approaches and Recent Applications," was published in Advances in Chemical Engineering and Science and can be found on pages 85-131.

Paper V, "Dynamic Simulation of a Polymer Molecule Using COMSOL Multiphysics: DNA Separation in a Microchannel," was published in COMSOL Conference Proceedings and can be found on pages 132-144.

ABSTRACT

The behavior of a typical nanorod particle in microscale flows was theoretically investigated, considering the effect of the wall on the rotational and translation motions of the non-spherical particle. Initially, a systematic method using Brownian dynamics simulation of the rotational motion of nanorod was performed to obtain the average orientation distribution of a nanorod in various range of Peclet number and position from the confining wall. Subsequently, the results of the angle distributions simulation were employed to generate a universal mathematical model for the particle orientation distribution, which our model of concentration distribution of high aspect ratio nanorods in the microchannel was later built on. We identified three different rod-wall interaction mechanisms in the entire rages of Pe. Then, the model was extended to study low and high aspect ratio ellipsoidal nanorod particle separation in a Field Flow Fractionation channel. The model can describe the aspect ratio dependent elution behavior.

In addition, Brownian dynamics simulation of microchannel separation of differently sized DNA chains driven by electrophoretic properties of DNA in an electric field was studied. COMSOL Multiphysics®, a popular science and engineering simulation software based on the finite element method, was used to perform the bead-spring dynamic simulation of the semi-flexible chain. The simulation results for DNA migration in an array of entropic traps were validated with the previous findings.

ACKNOWLEDGMENTS

TABLE OF CONTENTS

LIST OF ILLUSTRATIONS

Page

SECTION

1. INTRODUCTION

1.1. NUMERICAL ANALYSIS OF AVERAGE ORIENTATION OF A ROD-LIKE PARTICLE IN SHEAR FLOWS WITH THE EFFECT OF CHANNEL WALL

Application of nanorod particles (e.g. gold and silver nanorods, carbon nanotubes, and ZnO nanorods) throughout various medical and industrial fields is rapidly growing. Gold and ZnO nanorods with specific surface properties have been investigated in drug delivery systems [1-4]. Silver and ZnO nanorods have been studied to develop molecular sensors [5-7]. Distinctive structural and electrical properties of carbon nanotubes have made it a suitable candidate for many applications such as capacitors, Li-ion batteries, catalysts, sensors, and adsorption [8-12]. Shape and size of the nanoparticles significantly affect their physical and chemical properties [13, 14]. In drug delivery systems, shape and size of the particles are very important factors to determine their kinetic properties [15]. Similarly, optical properties of metallic nanoparticles are a strong function of particle shape and size [13]. Thus, in many applications, it is beneficial to reduce variation in geometrical properties of particles of interest. Many efforts have been made to fully control the geometrical features of nanoparticles in the early stages of their production [16, 17]. Despite that, controlling the parameters affecting the growth of the particles is not always easy, and most of the time nanoparticle synthesis methods are not always that predictive and accurate. Therefore, often a post-production separation and sorting step is inevitable to reduce variation in the size and shape of the nanoparticles. Furthermore, the size distribution of nanoparticles requires an analytical separation method. Also, many

biological microorganisms naturally have cell shape of a rod, and thus the process of cell purification for them follows the same principles of rod-like particle separation [18, 19].

Various nanoparticle separation methods have been studied, numerically and experimentally, and developed for specific applications to this date [14]. A vast majority of those methods involves a microchannel flow. Therefore, the particle motion and interaction in the flow has a great impact on the mechanism of separation. Unfortunately, most of those methods were investigated for separation of spherical particles, and for many of the applications, the separation mechanism of non-spherical particles has still remained an unknown area.

The motion of non-spherical particles, such as nanorods, is much more complicated due to their rotational behavior and their direction-dependent diffusional properties. Therefore, understanding the parameters that manipulate the orientation of the particle is an essential step to unlock comprehending particle motion in the surrounding flow. Nanorod orientation can be affected by the Brownian rotation of the particle as an internal force, as well as external forces such as hydrodynamic field or electrical field. Furthermore, the presence of solid objects, such as channel walls can influence the rotational motion of rod-like particles. Before completion of this research, there has not been a systematic approach to obtain a complete model for the average orientation of nanorods in near-wall regions. This part of the dissertation aims to address that problem by proposing a systematic method that uses the basics of Brownian dynamics simulation of the nanorod to define the relationship between its average orientation, and shear and Brownian forces, as well as entropic restriction of the channel wall.

1.2. MODEL DERIVATION FOR THE DEPLETION LAYER IN A DILUTE SUSPENSION OF ROD-LIKE PARTICLES UNDER SHEAR FLOWS

In the previous section the effect of the solid wall on nanorod orientation was investigated. The interaction of the nanorod with the channel wall and the surrounding fluid also influences the particle distribution in the near-wall region through several mechanisms. Consequently, the nanoparticle concentration in the near-wall region is lower than the freely rotating particles in the bulk region, as it has been previously observed in experiments [20]. Since then, a number of attempts have been made to find a model to describe the phenomenon [21-24]. However, due to a lack of understanding of the parameters involved in particle orientation determination, obtaining a complete model to account for the different range of shear flow, particle aspect ratio, and the effect of distance from the wall has failed.

Obtaining nanoparticles distribution in a channel is an essential step to develop and optimize a specific separation device. It also helps to understand the feasibility of the separation process and elution order of the particles of different shape and size in an existing method. Moreover, knowledge about the distribution of the nanorod particles is a crucial step to define rheological properties of the suspension.

In this section, the development steps to the derivation of a model for cross-sectional nanorod distribution have been discussed in detail. The comparison between the result of this work and a previous simulation [25] shows that the model can successfully predict the depletion layer of nanorod, over low, intermediate, and high ranges of Peclet numbers (the ratio of shear rate over rotational diffusion coefficient), where the mechanisms influencing the depletion pattern in each range are entirely different.

1.3. THEORETICAL MODEL FOR THE RETENTION BEHAVIOR OF ELLIPSOIDAL PARTICLES IN FIELD-FLOW FRACTIONATION

As mentioned before, precise sorting/purification (inorganic particles, colloidal particles, macromolecules, biological cells, etc) is essential in defining the chemical and physical properties of various types of particles. Hence, the number of studies on the development of new techniques, and enhancing existing methods is constantly growing. Field flow fractionation (FFF) is a single-phase analytical particle separation technique [24, 26]. Generally, the FFF device is comprised of a microchannel with an axial and cross-sectional hydrodynamic field, although, it can be designed in a way that the external cross-sectional force field is alternatively powered by an electrical, thermal, magnetic, centrifugal or gravitational force field [27]. There have been many studies on FFF theory for spherical particles [28, 29]. However, as this field is emerging for separation of non-spherical particles, we feel there is a lack of study on theoretical separation principles of non-spherical particles using FFF. For instance, a recent elution order of low aspect ratio of gold nanorods could not be explained by previous studies.

In this part, development of a theoretical model for ellipsoidal particle separation using FFF has been discussed in detail. This model is based on previous theoretical studies of high aspect ratio nanorods, which can be found in Sections 1.1 and 1.2. This study shows how different factors affecting the separation mechanisms were overlooked in previous works. The theoretical model sheds light on a previously observed unusual elution order of the low aspect ratio nanorods [30]. Lastly, a comparison between the results of the model and previously reported nanorod separation experimental data is reported. The results of the model showed strong agreement with experimental data.

1.4. BROWNIAN DYNAMICS SIMULATION STUDIES OF DNA SEPARATIONS IN MICRO-FABRICATED CHANNELS

Most biological molecules, such as DNA, naturally carry a negative charge. Hence, in the presence of an electric field, they will migrate towards the positively charged electrode (electrophoresis) [31]. Due to having a similar charge to mass ratio for different chain sizes of DNA, the mobility of the molecule in a free solution is not strongly affected by its size [32]. Therefore, a secondary separation mechanism is needed to distinguish molecules by their size. It has been discovered that physical and electrical interaction of DNA molecules with complex geometries can be used as a means for the creation of size-dependent mobility [33-35]. The most common separation method is to use a gel solution as a porous medium, with many physical barriers that force the DNA chain to change conformation while migrating through the gel. However, precise and rapid lithography methods of the microfluidic device make them more attractive for use in such separation techniques. Nevertheless, cost of the geometry optimization of a microfluidic device as a result of new fabrications might create a lot of limitation in the study. Therefore, computer simulations can be used instead to provide detailed information of the experiments, which can help to understand different mechanisms of separation.

In this study, first we completed a review of current techniques and advances in computational methods of DNA migration. Subsequently, we approached the problem with simulation of a semi-flexible chain (such as λ-DNA, but it can also be any polymeric molecule) using the popular engineering software COMSOL Multiphysics®. In the first part we validated the result of the simulation with previous experimental works. In an ongoing project, we are trying to use that knowledge to simulate a

separation process (using streaming flow for separation of non-spherical particles) and also a DNA stretching method (using dielectrophoretic characteristics of DNA molecules), which has never been done before. We are very positive that the simulation will show good potential for both uses, therefore making an impact in the field of DNA separation.

1.5. ORGANIZATION OF DISSERTATION

The first paper focuses on an approach to a systematic method of obtaining average orientation moments of a nanorod exposed to a shear flow. In this approach, the effect of the wall on the orientation of nanorod was investigated. In this work, all possible combinations of average double and quadruple moments as a function of a wide range of Pe's (shear rate divided by orientational diffusion) and position of the particle in the near wall region were obtained [36].

The second paper introduces a theoretical model for the center-of-mass distribution of nanorods across the microchannel hydrodynamic field using slender-body theory for nanorods (particle aspect ratio (Ar)>5). The model was derived using the average orientation moments of the rod-like particle obtained from the first paper as a fitted model. Several nanorod-wall interaction mechanisms were found, that would each be triggered at a certain range of Pe [37].

In the third paper, separation of a dilute ellipsoidal nanorod solution using a Field Flow Fractionation (FFF) device was modeled. This study extended the second paper for a broad range of aspect ratio of nanorods (1>Ar>5 as well as Ar>1). The model was validated with previously reported experimental data and was able to explain an anomaly

observed in recent experiments that could not be explained by currently proposed models [38].

In the fourth paper, the current challenges and recent advances in numerical studies on DNA separation and sorting method were discussed. Various methods of simulation, and their advantages and weak spots were investigated. New suggestions were made to develop current methods and to propose new applications in DNA separation.

The fifth paper introduces the use of COMSOL Multiphysics® software in the field of nano-sized semi-flexible particles. Migration of λ-DNA strains in an array of entropic traps was simulated. The validity of the simulation results was confirmed using previous experimental data. This paper could open a new window to the field of Brownian dynamics simulation of semi-flexible particles [39, 40].

The last section of this dissertation contains conclusions of these studies and provides suggestions for future work in this area.

PAPER

I. THE EFFECT OF WEAK CONFINEMENT ON THE ORIENTATION OF NANORODS UNDER SHEAR FLOWS[1]

Saman Monjezi [1], James D. Jones [1], Alyssa K. Nelson [1] and Joontaek Park [1,*]

[1] The Department of Chemical & Biochemical Engineering, Missouri University of

Science & Technology, Rolla, MO, 65409, USA; saman.monjezi@mst.edu

* Correspondence: parkjoon@mst.edu; Tel.: +1 (573) 341-7633

ABSTRACT

We performed a numerical analysis to study the orientation distribution of a dilute

suspension of thin, rigid, rod-like nanoparticles under shearing flow near a solid

boundary of weak confinement. Brownian dynamics simulation of a rod was performed

under various ratios of shear rate and rod diffusivity (Peclet number), as well as the

center-of-mass position (wall confinement). We discuss the effects of Peclet number and

wall confinement on the angle distributions, Jeffery orbit distribution, and average

orientation moments. The average orientation moments, obtained as a function of Peclet

number and wall confinement, can be used to improve a shear-induced migration model

[Phys. Rev. E. (2007) 76: 04081]. We demonstrate that the improved model can give

excellent prediction of the orientation moment distributions in a microchannel flow.

Keywords: Rod-like Particle, Nanorod, Orientation Distribution, Orientation Moments,

Microchannel Flow

---

1. INTRODUCTION

There have been multiple studies performed on the orientation dynamics and distributions of rod-like micro/nanoparticles in shear flow because these affect the center-of-mass distributions and rheological properties of the suspension of rod-like particles [1,2]. With rapidly advancing applications of micro/nanoparticles, which have shape-specific properties, it is becoming increasingly important to understand the structure and dynamics of micro or nano-sized rod-like particles or macromolecules in microscale flow systems [3-8]. However, in contrast to the various studies on the orientation and distribution of rod-like particles, theories on the distribution of rod-like particles near solid boundaries of a microscale flow are not enough to clarify abnormal experimental behaviors. For example, the elution order of gold nanorods in field-flow fractionation, which is a particle separation technique [9], is not clearly understood yet [10,11]. Therefore, a more accurate calculation of rod distribution under consideration of the steric effect of a wall is required for the prediction of the dynamics and elution behaviors in such a system [12,13] . In this work, we focus on the steric effect of a wall on the rod orientation distribution, more specifically confined in a channel, of which height is larger than the long axis length of a rod.

Rotation of a non-Brownian rod in an unbounded shear flow was found to follow a trajectory called Jeffery orbit [14]. Several works have shown that the Jeffery orbit is affected by hydrodynamic and mechanical interactions with other rods, Brownian motion, and inertia [15-19]. For Brownian rods in a shear flow, Boeder [20] suggests an equation to describe the orientation distribution of a rod. That distribution can be characterized by

the ratio between the shear rate, $\dot{\gamma}$, and the rotational diffusivity of the rod, D_R, which is defined as Peclet number:

$$Pe \equiv \frac{\dot{\gamma}}{D_R} \qquad (1)$$

The orientation distribution can be numerically solved as a function of Pe [21]. The average values of orientation moments (the products of the orientation vector components) of a Brownian spheroid as a function of Pe were calculated, as well as derived in a form of harmonic potential [22,23]. It was also shown that the average orientation moments obtained by performing Brownian rod simulation of a slender body are very similar to those of a spheroid [24]. The average orientation moments were also used in a model equation for predicting the center-of-mass distribution influenced by shear-induced migration [25-27]. However, the average orientation moments when considering the effect of the wall were not available, which resulted in a discrepancy between the simulated and the analytically derived distributions [25,26] , also shown in Figure 16.

The steric hindrance effect on the rod orientation was studied for a strongly confined channel with very narrow height (less than the long axis length of a rod) [28]. However, the study for a weakly confined channel with a wide height (larger than the long axis length of a rod) gives only limited information which is not enough to be applied to the aforementioned predictions of rod behaviors [29]. Moreover, these studies were performed on an assumption that rod rotation is on a 2D plane, excluding the vorticity direction. There were also studies performed on rod orientation and its effect on the distributions in limited flow conditions, such as low Pe [30-32].

The lack of study on this issue is likely because the effect is not easily characterized by the distance between a rod's center-of-mass and the wall surface, r_c, due to the combined translational and rotational motion as a response to a collision with the wall. For example, once the tip of a rod touches the wall, two types of behavior are possible: either its r_c changes, or its r_c remains the same with a change in its orientation. Hijazi and Khater studied both cases (named "surface restitution") via Brownian dynamics simulation and suggested that the response having a change in r_c is the more reasonable of the two outcomes [28,29]. Additionally, it has been known that a rod under a shear flow near a wall shows "pole-vault" type rotation, which accompanies the lift of r_c due to the excluded volume effect of the wall [33-35].

Our study will systematically show the orientation distributions in terms of normalized probability distribution functions of various angles in wide ranges of Pe. The details of our simulation algorithm will be described in the next section. The simulation results will be presented in terms of various orientation distributions and the average orientation moments as a function of Pe with various confinements (i.e. given values of r_c). Finally, it will be demonstrated that our study can be applied to show an improved prediction of the average orientation of a Brownian rod flowing in a microchannel than the previous works [24-26].

2. NUMERICAL METHOD

2.1. DEFINITIONS OF THE VARIABLES FOR A ROD CONFIGURATION

For the investigation of a rod orientation restricted by a wall, we performed Brownian dynamics simulation of a thin, neutrally buoyant, rigid rod near a wall in a

simple shear flow. As shown in Figure 1, a rod with its principal axis length, $L=2a$, and its diameter, $d=2b$, is under a flow with a shear rate of $\dot{\gamma}$. The Cartesian coordinate system is set so that the flow is in the x-direction, the velocity gradient is in the y-direction, and the vorticity is in the z-direction. It is assumed that the channel height, H, is larger than $2L$ so that the rod orientation is only restricted by the bottom wall ($y=0$). The channel width is much larger than the channel height so that the steric effect in the z-direction is ignored. The unit vector describing rod orientation is $\mathbf{p}$ and has p_x, p_y, and p_z components in the respective x, y, and z directions. The rod configuration is approximated as a slender-body [36], and thus its rotational diffusivity can be written as follows:

$$D_R = \frac{3k_B T}{8\pi\mu a^3} \ln\left(\frac{2a}{b}\right) \tag{2}$$

Here, k_B is the Boltzman constant, T is the absolute temperature, and μ is the solvent viscosity.

Figure 2 demonstrates the angles that were investigated: θ is the angle between a rod's principal axis and the flow direction on the xy- plane and ψ is the angle between a rod's principal axis and the shear direction (y). We focus on the distributions of θ and ψ which show characteristic rod orientation behaviors. However, we also define the other angles: φ is the angle between a rod's principal axis and the vorticity direction (z), χ is the angle between a rod's principal axis and the flow direction on the xz- plane. Note here that χ is not affected by the confinement. The relations between these angles and the vector components of $\mathbf{p}$ can be written as shown below:

$$\theta = \tan^{-1}\left(\frac{p_y}{p_x}\right), \quad \varphi = \cos^{-1}(p_z), \quad \chi = \tan^{-1}\left(\frac{p_z}{p_x}\right), \text{ and } \psi = \cos^{-1}(p_y) \tag{3}$$
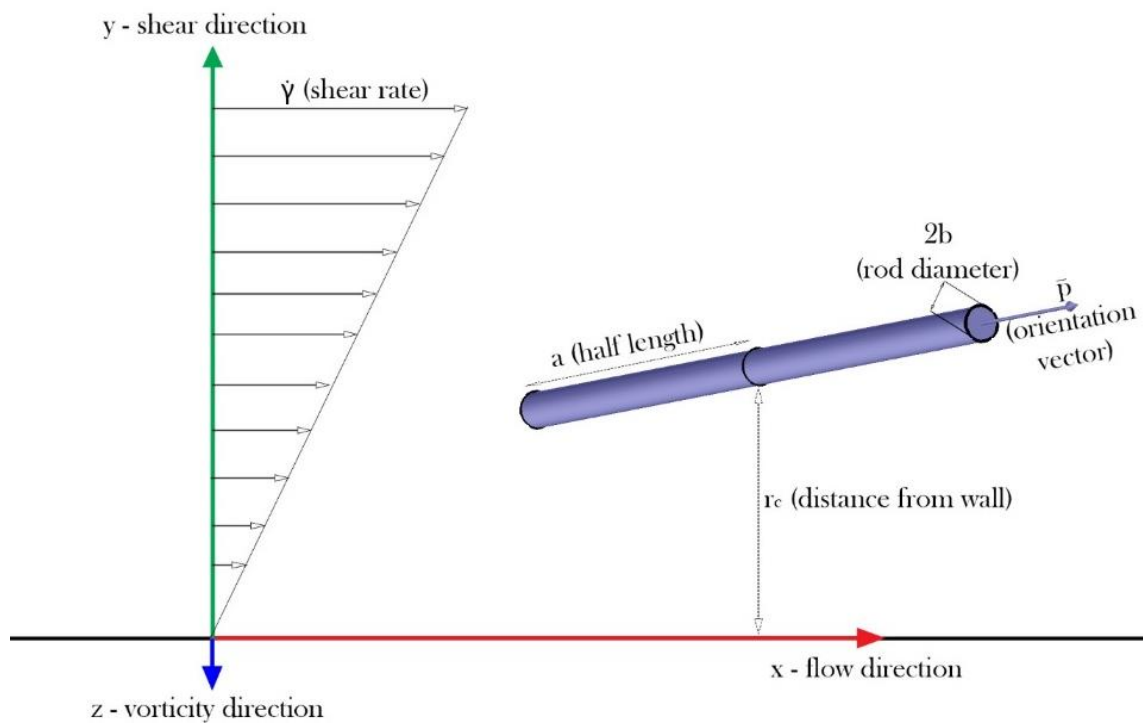
Figure 1. Schematic diagram of a rod under shear flow near a wall.
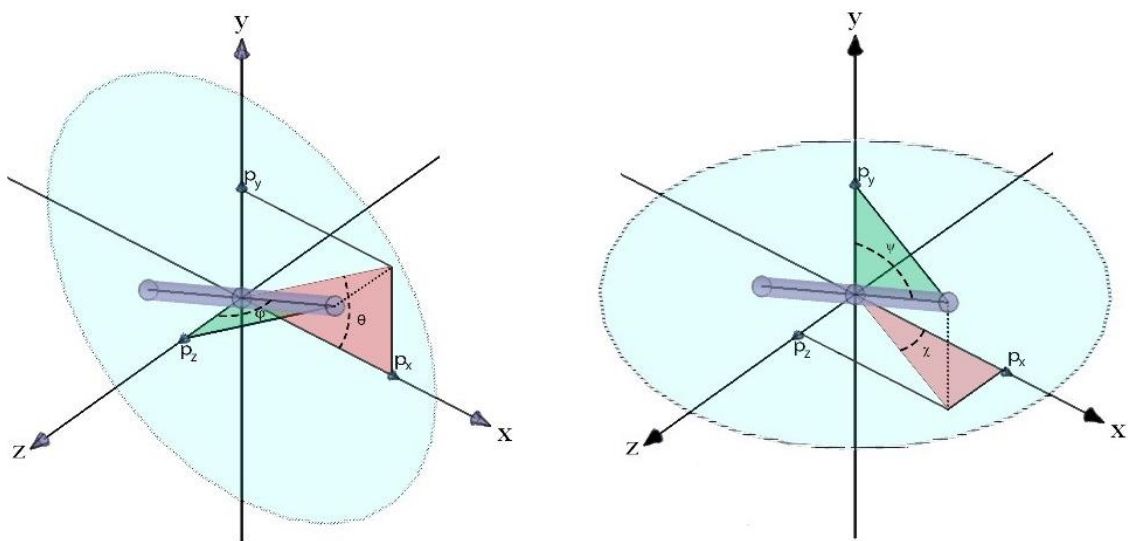
Figure 2. The orientation variables for a rod configuration.

(Left) θ and φ as well as (Right) ψ and χ. Note that either set of θ and φ or ψ and χ determines the rod orientation **p**. The distribution of θ gives a unique feature (asymmetric distribution) of Brownian rod under shear flow. The distribution of ψ is directly related to the geometrical constraint by the weak confinement.

2.2. SIMULATION APPROACH AND ASSUMPTIONS

For a Brownian rod experiencing a weakly confined channel flow, its r_c continues to change dynamically due to Brownian translational motion and collisions with the wall (see Figure 3). Therefore, the proper algorithm must be implemented to correctly characterize the wall confinement effect on the rod orientation in terms of $r_c = \alpha$, the given position of interest.

Theories and simulation approaches for Brownian dynamics of rods have been developed by many researchers [37,38]. Park & Butler (2009) performed a simulation of a Brownian rod in a microchannel shear flow while considering long-range as well as short-range (lubrication) hydrodynamic interactions between a rod and the walls. The main purpose of the simulation was to confirm the center-of-mass distribution in the cross-sectional direction predicted by a previous analytical model. The orientation distribution in the cross-sectional direction was also investigated using the simulation data. Comparing the simulation results that both considered and ignored hydrodynamic interactions, it was found that the average orientation moments did not show any noticeable differences, even in the near-wall region. It was conjectured that the excluded volume effect on particle distribution is more dominant than the hydrodynamic interaction in the near-wall region. This result suggests that although the hydrodynamic

interaction affects each rod's motion the resulting averaged orientation distribution is not affected. Moreover, our interest is more focused on the steric effect on the orientation distribution and moments. Therefore, hydrodynamic interaction is not considered in our simulation method.

A rod in the near-wall region ($0<r_c<a$) can collide with a wall due to either Brownian motion or shear flow. Hijazi and Khater [28,29] classified the types of rod collisions with a wall as Brownian collision and shear collision in their "surface restitution" study. They also investigated how the rod translation and rotation are changed by the collisions. They showed that it is plausible for the Brownian collision, either caused by Brownian translation or rotation, to result in a rod translation away from a wall (lift of r_c), as shown in Figure 4, considering a theoretical center-of-mass distribution. They also claimed that their experiment observed the shear collision to result in the pole-vault type, as also observed by others [33-35], rotation which lifts r_c to a, as shown in Figure 5. Either collision results in the lift of r_c: the orientation after the lift is no longer equal to the orientation at the original rod position of interest, $r_c=\alpha$. Furthermore, the lifted rod comes back to the original position $r_c=\alpha$ by Brownian translation later in the simulation, which is expected to make the orientation at collision and at returning more unrelated.

Based on those two arguments, considering the relative frame on a rod, we propose to study the steric effect of a wall on the rod orientation distribution by investigating the rod orientation data collected through the simulation of Brownian rotation of a rigid rod of which r_c is fixed at a chosen position, $r_c=\alpha$. During the simulation, if the tip of a rod invades the boundary ($|p_y|>\alpha/a$), the resulting configuration

data will not be collected for analysis (shown in Figure 6). Our assumption is that the

orientation data collected in the previous simulation method (Figure 3) and our proposed

method (Figure 6) are equivalent or at least acceptably close. We chose the proposed

method to investigate the effect of the distance from a wall, α, on the orientation

distribution and average moments more systematically and efficiently. The previous

simulation had a difficulty in collecting enough number of data because the probability

for a rod existence (the center-of-mass distribution) in the near-wall region is lower due

to the shear-induced migration. The resulting orientation distributions from this

simulation and the previous simulation will be compared with each other to confirm the

validation of the assumption stated above, which will be shown in the Results &

Discussion section. It is also important to mention that we tried multiple different

simulation methods. For example, we applied excluded volume force or re-assign a

random orientation after a collision. Although those methods seem intuitively reasonable,

they all gave unphysical results, which imply the validation of our proposed method.
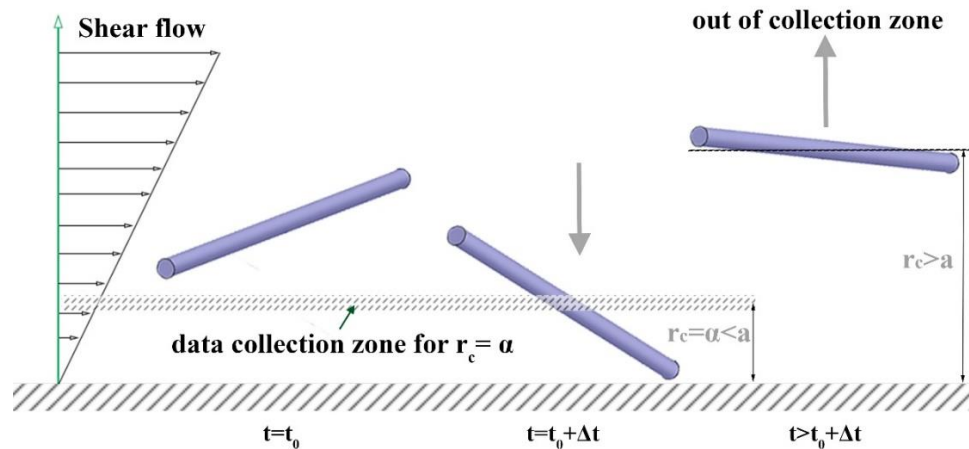
Figure 3. Schematic demonstration of a rod movement in a microchannel near a wall and the rod orientation data collection algorithm in the previous simulation by Park & Butler (2009).
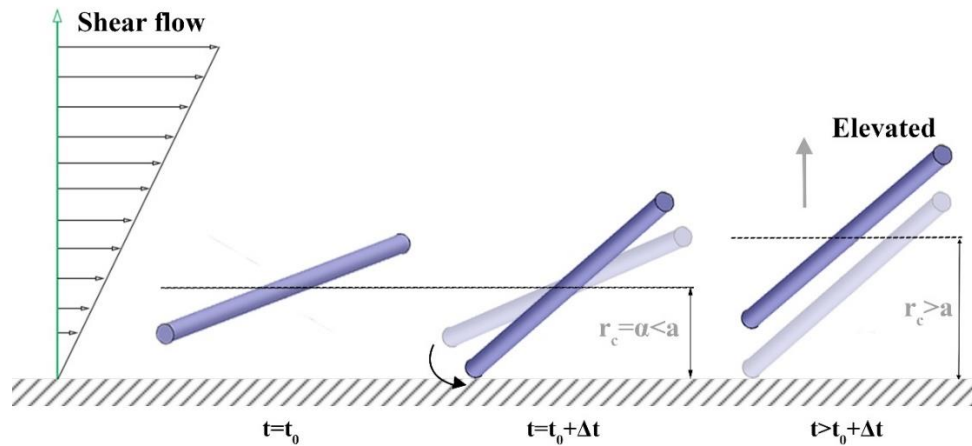
Figure 4. Schematic description for the "Brownian collision" event: Once a tip of a rod invades a boundary, the rc of the rod is lifted without changing its p.
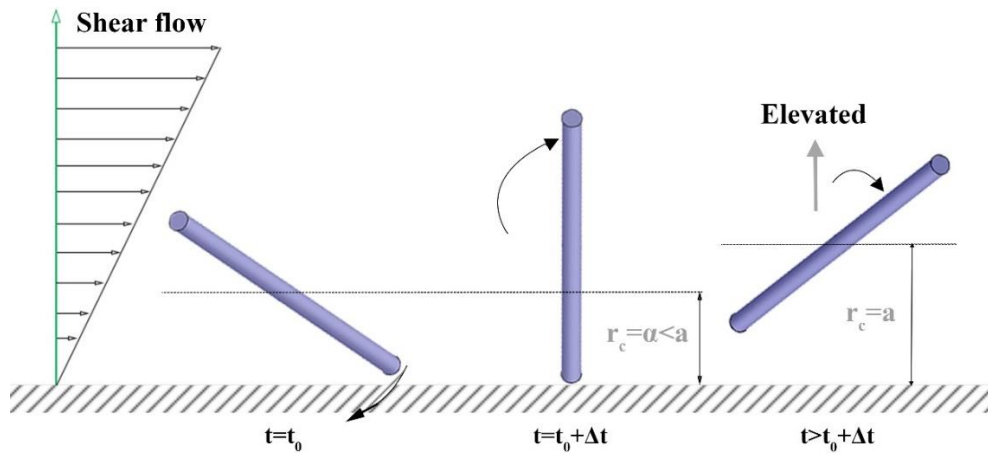
Figure 5. Schematic description for the "shear collision" event and the subsequent "pole-vault motion". This motion suddenly pushes r_c from α to a.

2.3. INITIAL CONFIGURATION

For each simulation $r_c = \alpha$ is chosen to be between 0 and a, and Pe is chosen to be between 10^{-3} and 10^4. Furthermore, an initial orientation of a rod is randomly determined through the following stepwise procedure [39]:

(1) p_x, p_y, and p_z are assigned a random number between -1 and 1.

(2) If |**p**|>1, repeat step (1). Otherwise, normalize p_x, p_y, and p_z with the magnitude of new **p, |p|**.

If the normalized p_y is not between $-\alpha/a$ and $+\alpha/a$, repeat steps (1) and (2) until p_y is correctly constrained ($-\alpha/a \leq p_y \leq +\alpha/a$).
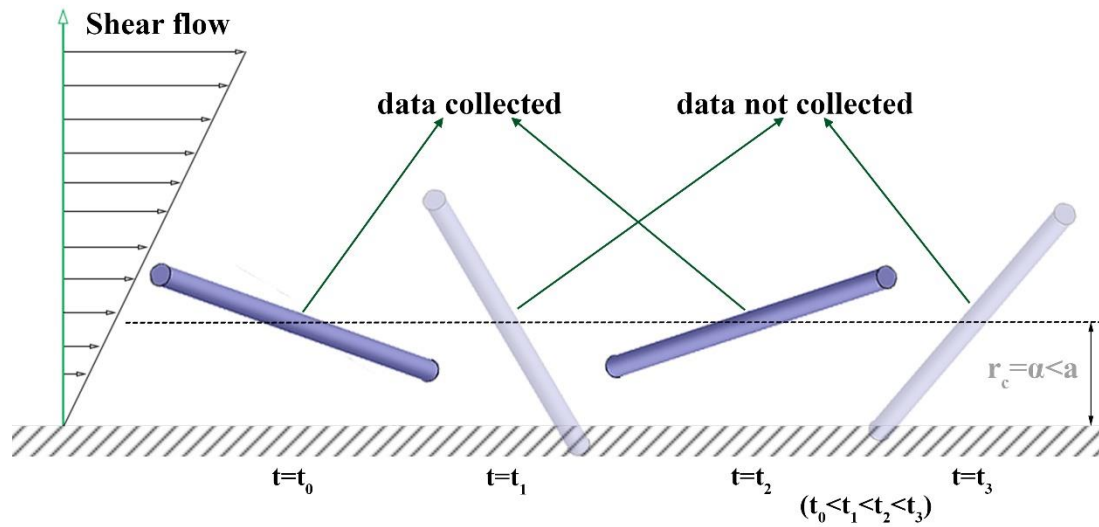
Figure 6. Schematic demonstration for the data collection algorithm in the simulation method proposed in this study.

2.4. EQUATION OF MOTION

The rotation of a Brownian rod under a shear flow can be described by the following equation:

$$\dot{\boldsymbol{p}} = \dot{\gamma}p_y(\hat{x} - p_y\boldsymbol{p}) + \frac{3}{\pi\mu L^3}\ln\left(\frac{2L}{d}\right)[\boldsymbol{\mathcal{T}} \times \boldsymbol{p}] \qquad (4)$$

Here, $\hat{x}$ is a unit vector in the x-direction. Brownian torque is denoted as $\boldsymbol{\mathcal{T}}$. With some manipulation, as described in the previous work by Park [26], a new orientation can be calculated numerically at each time step by integrating the following equation.

$$\dot{\boldsymbol{p}} = p_y(\hat{x} - p_y\boldsymbol{p}) + \sqrt{\frac{2}{Pe\Delta t}}(\boldsymbol{I} - \boldsymbol{pp}) \cdot \boldsymbol{w} - \frac{2\boldsymbol{p}}{Pe} \tag{5}$$

Here, t is a dimensionless time in terms of a characteristic time of $1/\dot{\gamma}$. The identity matrix is $\boldsymbol{I}$. A random vector, $\boldsymbol{w}$, has a mean of zero and one unit variance [39]. The third term on the right hand side is a correction term for numerical integration by a modified Euler method, which reduces computational time because it does not require correction at the intermediate time step [40].

2.5. SAMPLING DATA DURING DYNAMIC SIMULATION

The integration of Eq. 5 is repeated from $t=0$ to t_{end}, the end time for one particle simulation. It is then repeated for N particles. During that "one simulation set" over N particles for each period of t_{end}, a rod configuration is sampled in terms of $\boldsymbol{p}$ at each m-th sampling time for the n-th particle, $t_{n,m}$. If the sampled $|p_y(t_{n,m})|$ is less than α/a (i.e. the rod configuration is within the confinement), the orientation data is collected for analysis (see Figure 6). We confirmed that the effects of the chosen simulation parameters give convergent results. It is also important to note here that the invasion of the wall boundary is evaluated based on the rod center line, neglecting the rod diameter. Details of a rod geometry (such as cylinder or spheroid) may be only important for low values of $a/b<10$. For thin slender rods, $a/b>10$, the diameter can be neglected or adjusted easily, which will be shown in the application to modification of a shear-induced migration model.

2.6. ORIENTATION DISTRIBUTION

Rod orientation distributions were investigated by plotting the rod angles from the collected orientation data determined from the Brownian dynamics simulation. The

collected rod configuration data, $\mathbf{p}(t_{n,m})$, was converted for each angle via Eq. 3 to obtain

probability distribution functions (PDFs). The converted angle data, $\theta(t_{n,m})$ and $\varphi(t_{n,m})$,

are counted on each unit area ($\Delta\theta=1°$ by $\Delta\varphi=1°$) on a spherical surface spanned by the

tips of a rod. The counted bins on each unit area are then normalized by the total number

of the collected sampled data to give the PDF on the spherical surface. In other words,

integration of the PDF on the whole range gives 1. Additionally, each angle is counted on

unit interval ($\Delta angle=1°$) and then normalized to give the PDF of the corresponding

angle. The simulation parameters were chosen as $\Delta t=5\times10^{-7}$, $t_{end}=100$, and $N=1000$. The

sampling was made at each time step.

2.7. AVERAGE ORIENTATION MOMENTS CALCULATION

Orientation moments were averaged over the collected orientation data, $\mathbf{p}(t_{n,m})$.

For example, an ensemble average of one of the second-order orientation moments,

$<p_x p_y>$, obtained from the one simulation set is:

$$\langle p_x p_y \rangle = \frac{1}{N}\sum_n^N \frac{1}{M(n)}\sum_m^{M(n)} p_x(t_{n,m})p_y(t_{n,m}) \tag{6}$$

Here, $M(n)$ is the total number of the collected orientation data sets falling within the

boundary for the n-th particle simulation. The average values from Eq. 6 typically have

large standard deviations for low Pe's due to the broad orientation distribution. Because

we intend to extract a model for each of the average moments in terms of Pe and α, a

different approach was adapted to get more convergent values with smaller standard

deviations. We used $\Delta t=5\times10^{-7}$, $t_{end}=1000$, and $N=100$. Data was sampled at every 200th

time step. The determination of this "one simulation set" was repeated until five

ensemble average values were obtained using Eq. 6. These five values were then

averaged again. Most of the resulting standard deviations determined from this method were less than 2% of the average values.

We calculated all of the possible combinations of the second-order and the fourth-order orientation moments. However, we only display $<p_xp_y>$, $<p_y^2>$, and $<p_xp_y^3>$, which are related to a theoretical model equation for shear-induced rod migration [12,13,25,26].

3. RESULTS AND DISCUSSION

3.1. ORIENTATION DISTRIBUTION NEAR A WALL

PDFs of θ, φ, ψ and χ were obtained from each simulation, as well as PDFs of the spherical surface spanned by the tips of a rod for various values of Pe and α. Figures 7 and 8 show PDFs at Pe=0.001. At this very low value of Pe the effect of shear on each PDF is negligible, and the effect of Brownian rotation dominates the PDF. Figure 7 shows the spherical PDF(θ,φ) at Pe=0.001. If there is no confinement, ($\alpha/a \geq 1$), the PDF becomes almost evenly distributed over the spherical surface due to Brownian rotation. As the confinement is varied with α/a=0.1, 0.5, 0.9 and 1.0, the PDF gets restricted within the confinement, but the restricted distribution is still even.

Figure 8 shows PDFs for θ and ψ defined in Eq. 3. Figure 8a shows the PDF(θ) at Pe=0.001. For the unbounded case of α/a=1.0, the PDF(θ) is also almost evenly distributed. As α/a decreases, the values of PDF between confinement angles, $\sin^{-1}(-\alpha/a) < \theta < \sin^{-1}(+\alpha/a)$, increase in height but is still almost evenly distributed. Less probable distribution outside of the confined angle region is possible for the configurations near the z-axis. For example, although $\mathbf{p}$=(0,0.5,0.866) has θ=90$^\mathrm{o}$, this orientation can exist out of any θ confinement region. The PDF(ψ) is only non-zero

inside of the confinement angle range, $\cos^{-1}(+\alpha/a) < \psi < \cos^{-1}(-\alpha/a)$. Therefore,

the PDF(ψ) at each confinement looks similar to squares within that confinement range.
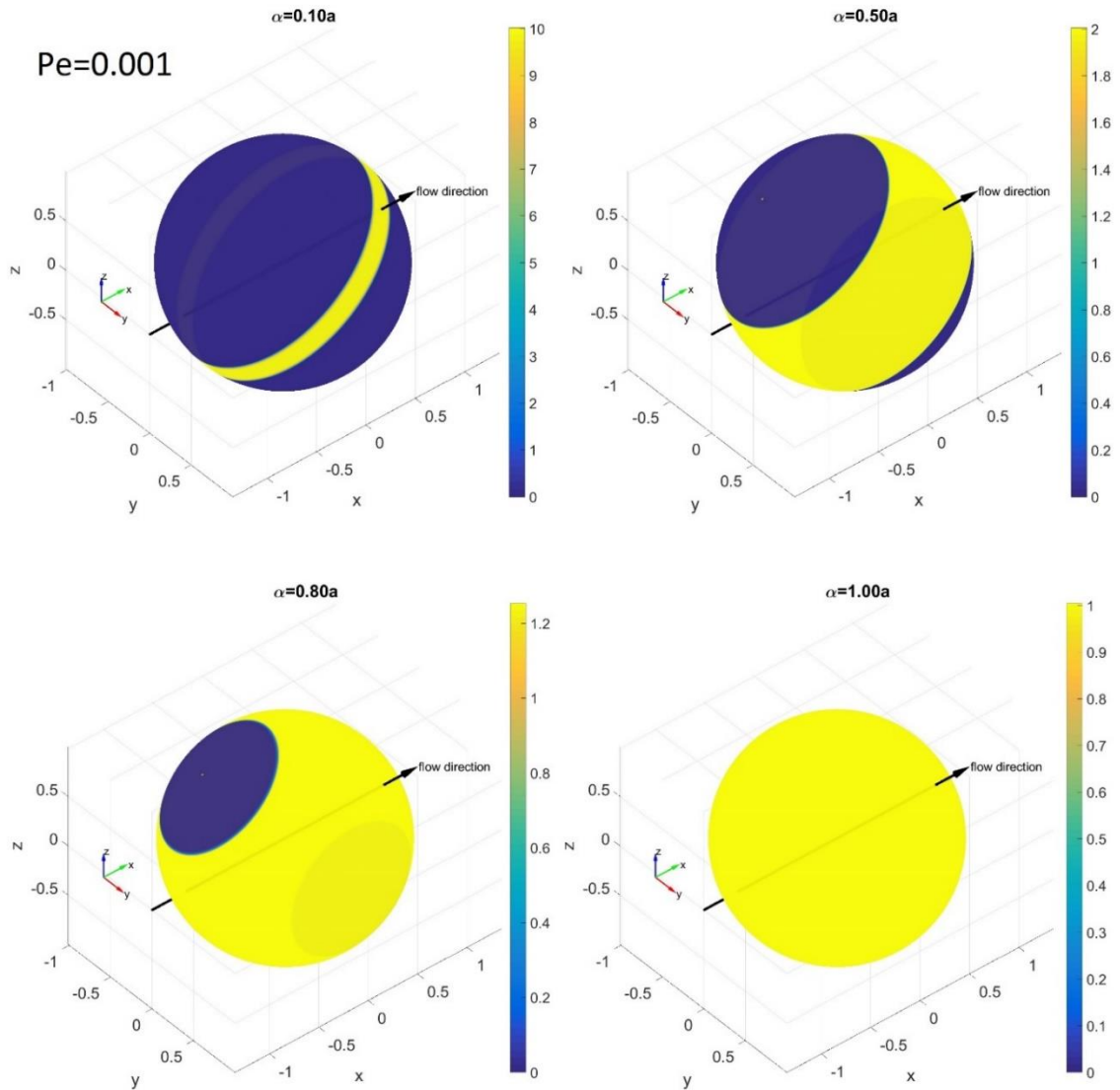
Figure 7. Simulation results for the PDF(θ,φ) on the spherical surface of the tips of a rod at *Pe*=0.001 with α/a=0.1, 0.5, 0.9, and 1.0. The color bars represent the probability density levels of each PDF from yellow (highest probability) to dark blue (lowest probability) (color online).
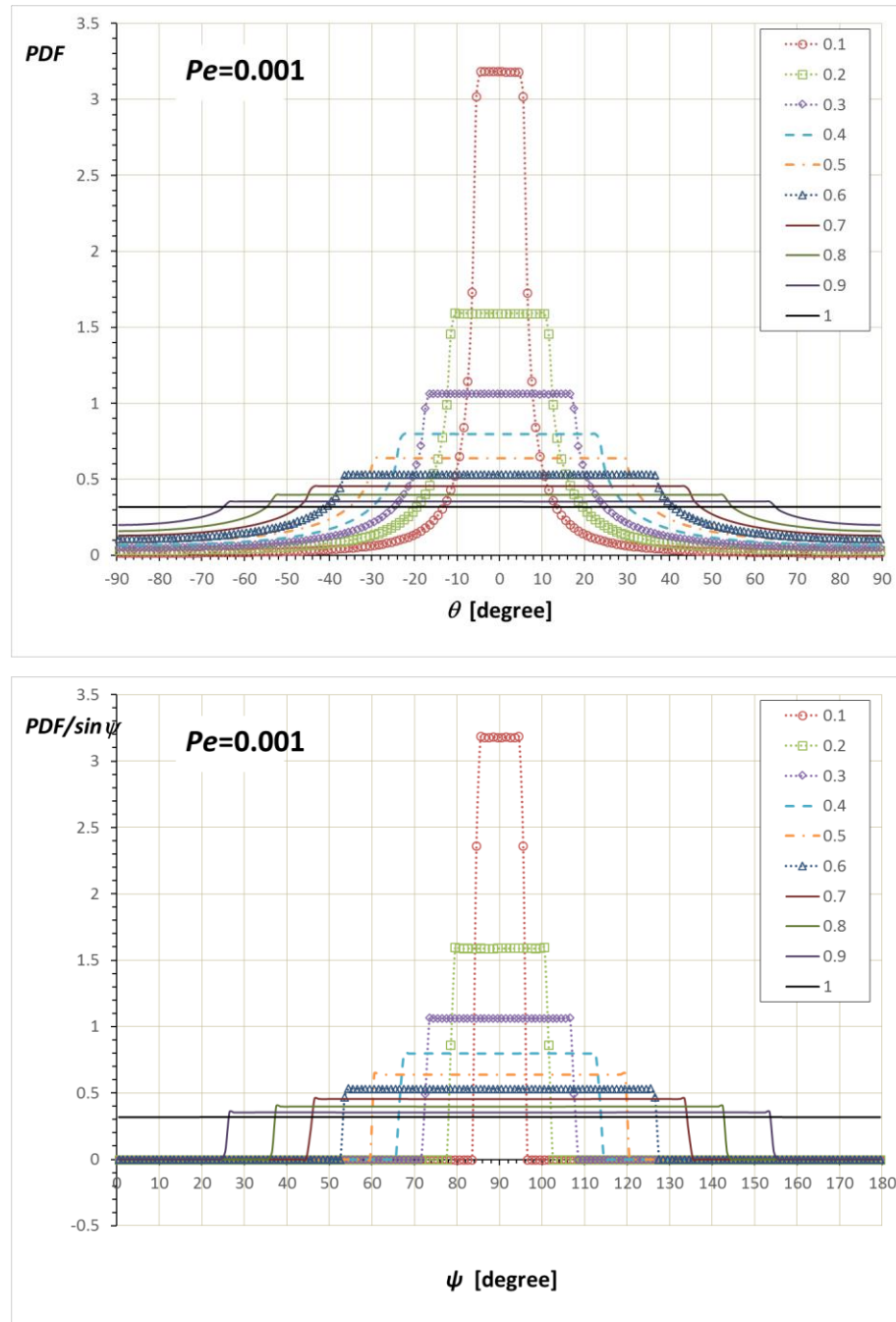
Figure 8. Simulation results for the (a:Top) PDF(θ) and (b:Bottom) PDF(ψ)/sinψ at Pe=0.001 with various α/a.

In contrast to the PDFs at low Pe values where Brownian rotation makes the distribution even within a confined angle region, PDFs at higher Pe values show

distinctive concentrated densities on a certain angle region. We chose to present the results at $Pe=10$ for the convenience of describing this distinctive feature. Figure 9 shows the spherical PDF(θ,φ) at $Pe=10$. The unconfined PDF(θ,φ) at $\alpha/a \geq 1$ shows a concentrated density along the x-axis; however, it is shifted towards the y-axis. This distinctive distribution of Brownian rods under shear flow at $Pe>1$ is explained by Jeffery orbit rotation, as well as the competition between rod orientation relaxation from the Brownian rotation and rod alignment from shear flow [21].

At $\alpha/a=0.8$, the confinement does not affect the maximum density region. Therefore, the PDF(θ,φ) is only sliced at the confinement, and the overall shape is not changed much. However, as α/a becomes smaller than 0.4, the maximum density region at $\alpha/a>0.4$ begins to reside out of the confinement region. As a result, the distribution becomes more concentrated towards one side of the confinement region.

Figure 10a shows the PDF(θ) at $Pe=10$ and various α/a's. At $\alpha/a=1$, where rod rotation is not restricted by a wall, the PDF(θ) shows the off-center maximum, which is well known for a Brownian rod under shear flow [21]. The off-center maximum is found to be at $\theta_{max} \approx 25^{\circ}$ for $Pe=10$. As α/a is reduced and the confinement angle region remains larger than $\theta_{max} < \sin^{-1}(\alpha/a)$ (i.e. $0.43<\alpha/a<1$), the off-center maximum is not affected, but the distribution is sliced at $\sin^{-1}(\pm\alpha/a)$. However, at $\alpha/a<0.43$, the distribution becomes concentrated at the positive limit of the confinement, which is expected because the rod cannot be distributed towards the maximum density region at the unconfined condition. Figure 10b shows the PDF(ψ)/$\sin\psi$ at $Pe=10$. The unconfined PDF(ψ)/$\sin\psi$ at $Pe=10$ shows a curved distribution. As in the case of the PDF(θ), the PDF(ψ)/$\sin\psi$ at

0.43<α/a<1 shows the cutoff at $\sin^{-1}(\pm\alpha/a)$, whereas the PDF(ψ)/sinψ at 0<α/a<0.43

shows square-like shape as in the low *Pe* case.
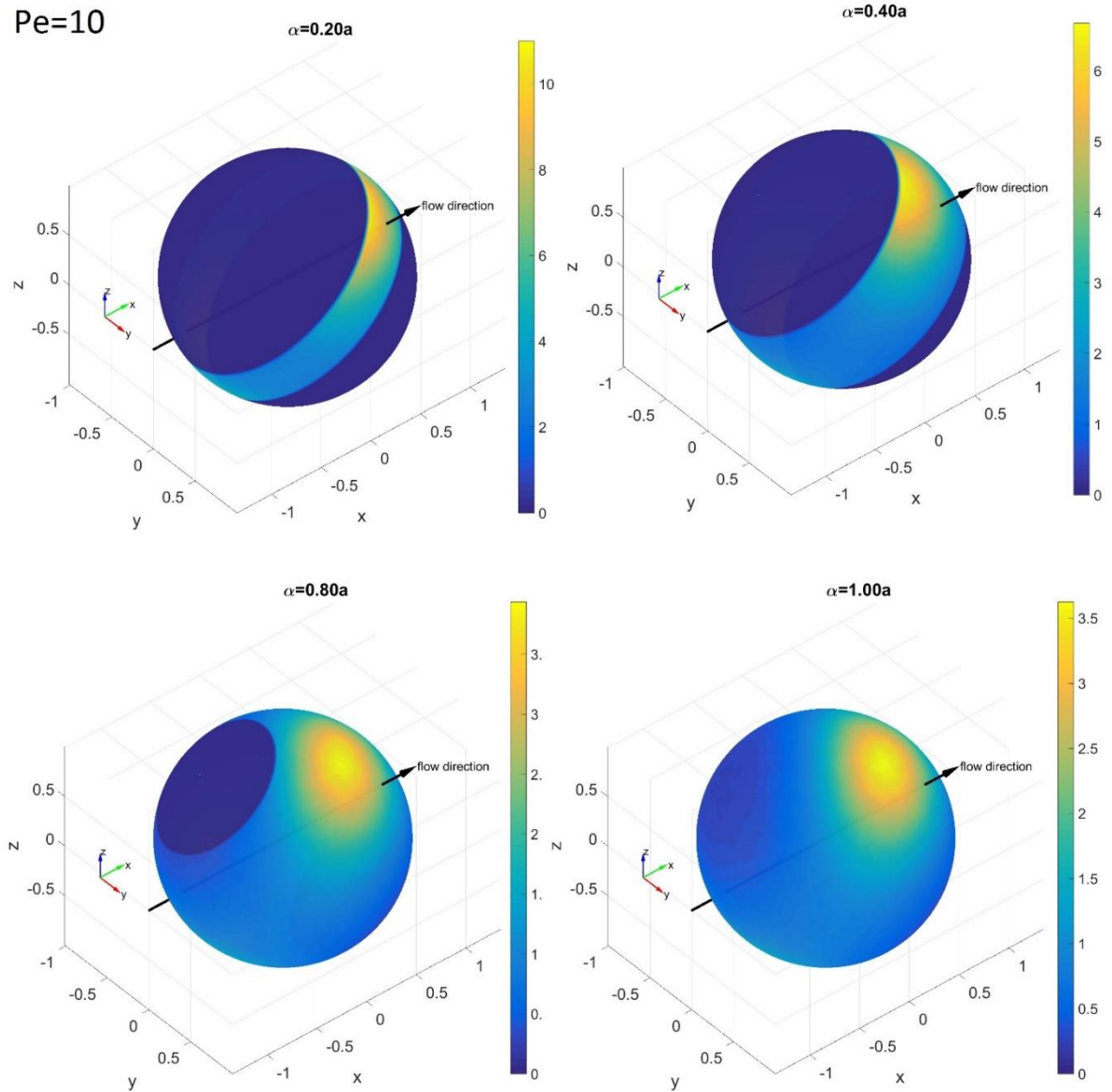
Figure 9. Simulation results for the PDF(θ,φ) on the spherical surface of the tips of a rod at Pe=10 with α/a=0.2, 0.4, 0.8 and 1.0. The color bars represent the probability density levels of each PDF from yellow (highest probability) to dark blue (lowest probability) (color online).

Note here that PDFs at Pe=1.0 simply show that the distribution patterns are in between those of Pe=0.001 and Pe=10.0. For example, the off-center maximum is found to be at $\theta_{max}\approx40.5^o$ for Pe=1.0. The confinement, $\sin 40.5^o=0.65<\alpha/a<1$, gives PDF($\theta$)s
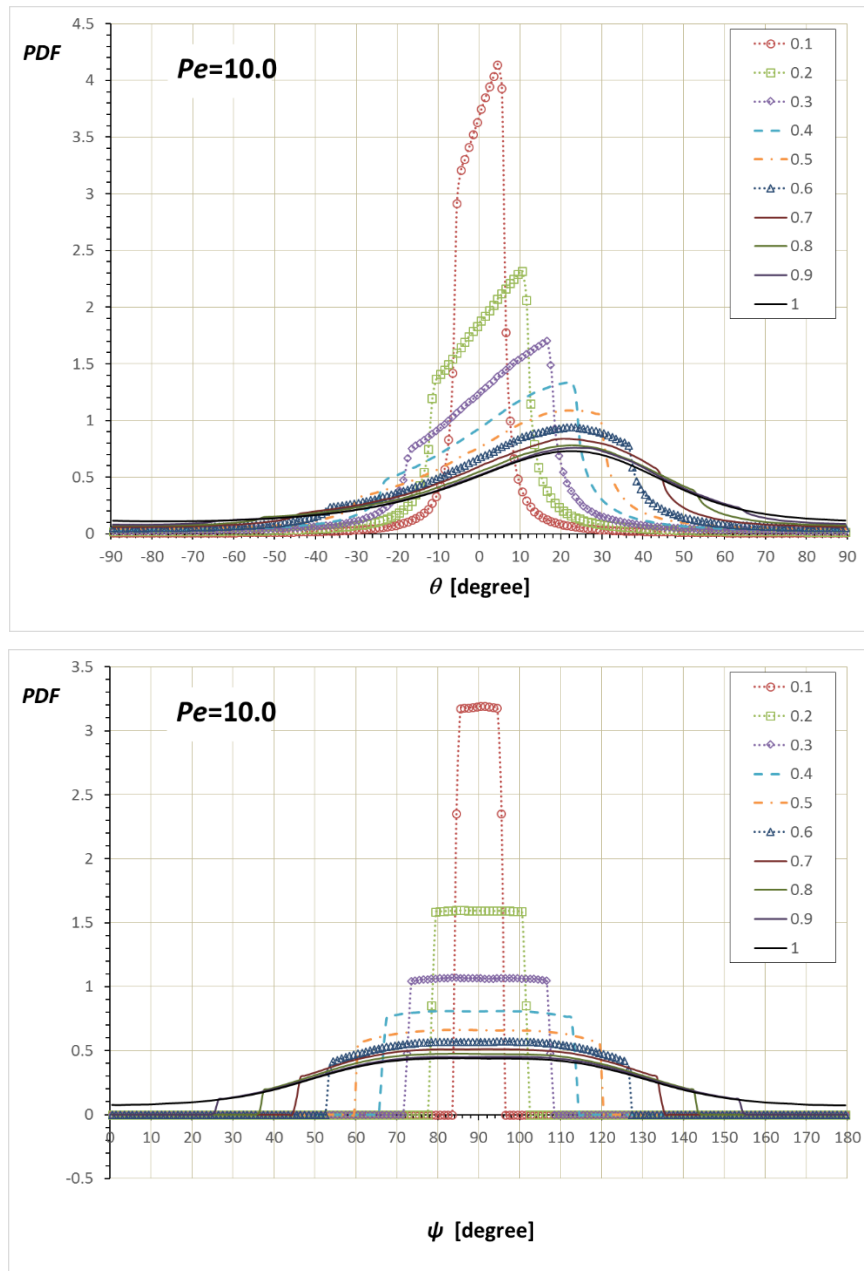
Figure 10. Simulation results for the (a:Top) PDF(θ) and (b:Bottom) PDF(ψ)/$\sin\psi$ at Pe=10 with various α/a. It is seen that $\theta_{max}\approx25^o$, which corresponds to α=0.43a.

which maintain $\theta_{max}\approx40.5^o$, while the other confinement, $\alpha/a<0.65$, results in the distribution being concentrated at the positive limit (data not shown).

Figures 11 and 12 show PDFs at $Pe=1000$. At this high value of Pe, most of the distributions are aligned along the x-axis with the off-center maximum at $\theta_{max}\approx4.5^o$. The wide range of the confinement, $\sin 4.5^o=0.078<\alpha/a<1$, gives PDF($\theta$)s which maintain $\theta_{max}\approx4.5^o$. As in the PDFs shown so far, the pattern change happens when the confinement becomes narrower than the θ_{max} ($\sin 4.5^o=0.078>\alpha/a$).
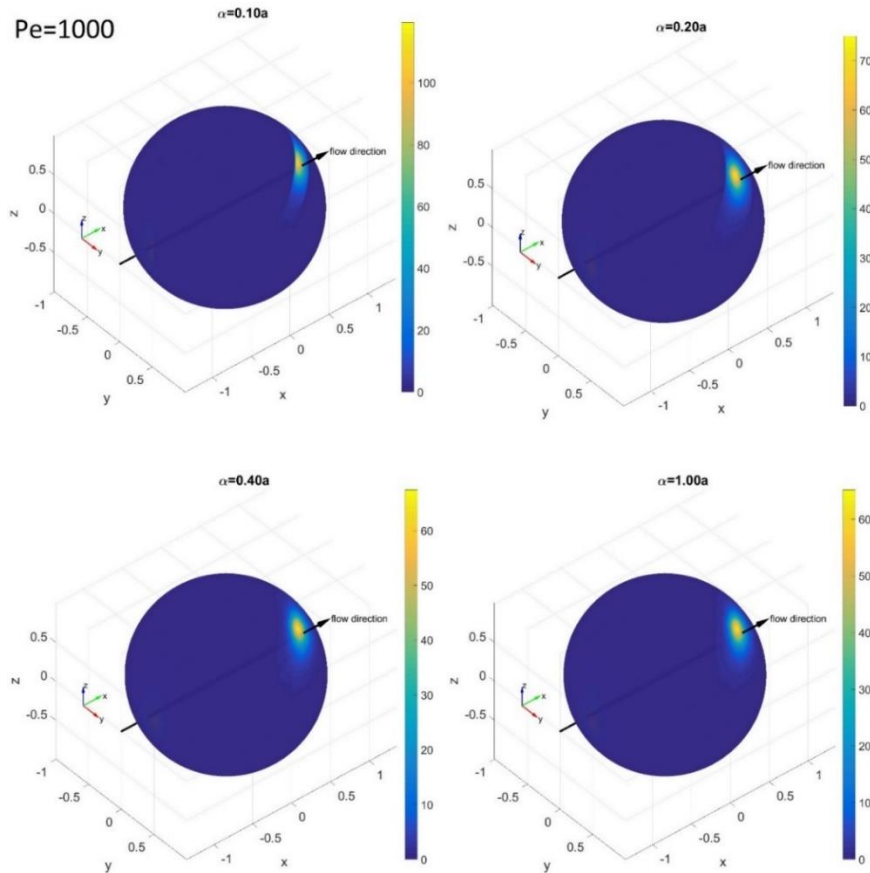
Figure 11. Simulation results for the PDF(θ,φ) on the spherical surface of the tips of a rod at $Pe=1000$ with $\alpha/a=0.1$, 0.2, 0.4 and 1.0. The color bars represent the probability density levels of each PDF from yellow (highest probability) to dark blue (lowest probability) (color online).
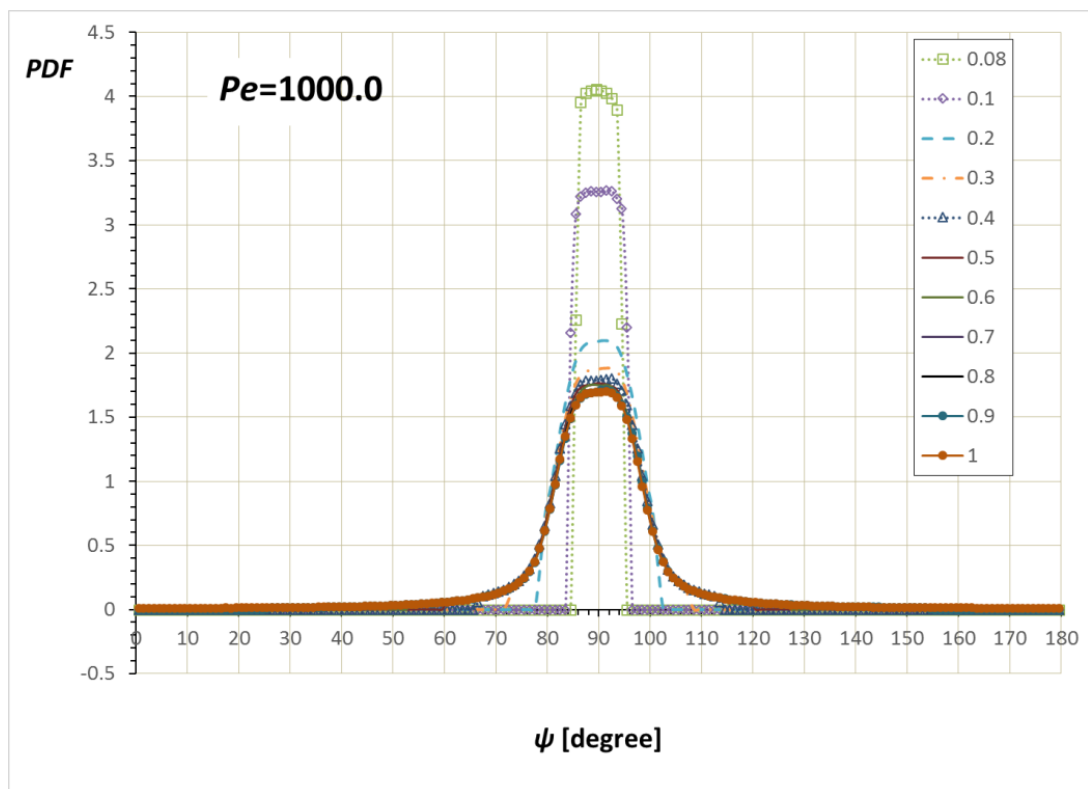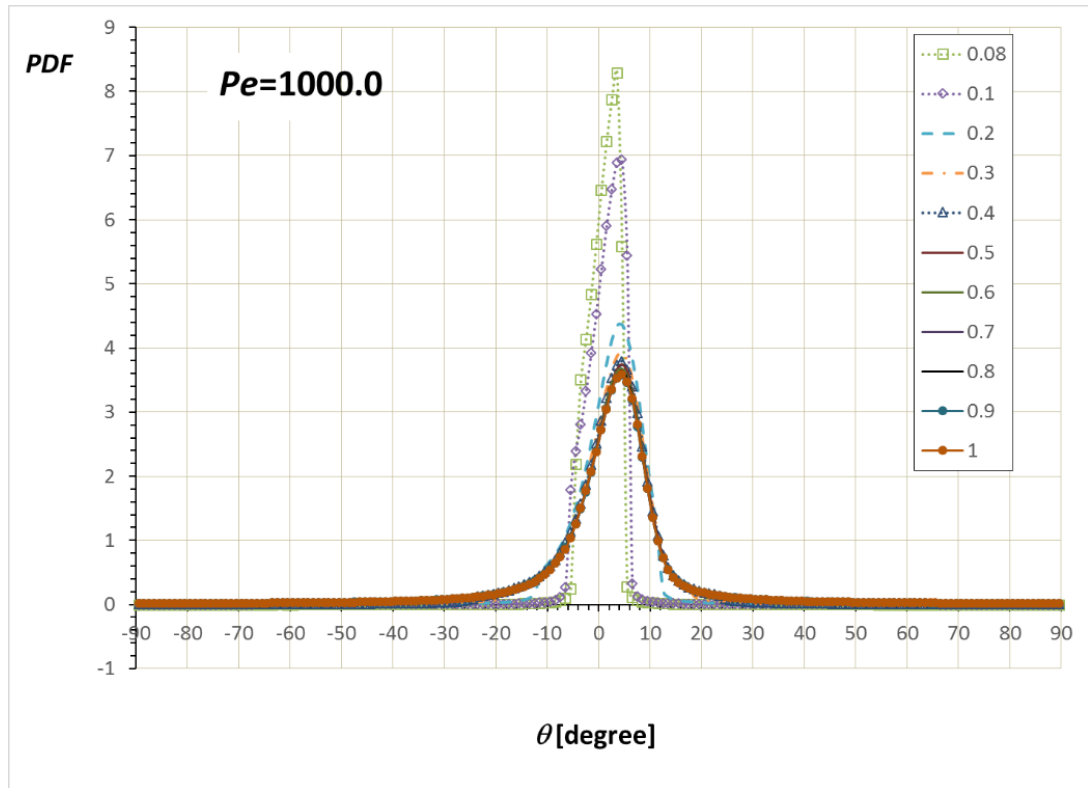
Figure 12. Simulation results for the (a:Top) PDF(θ) and (b:Bottom) PDF(ψ)/sinψ at Pe=1000 with various α/a. It is seen that θmax≈4.5o, which corresponds to α=0.078a.

Comparing with the previous work by Hijazi and Khater [29], our PDF(θ) seems reasonably similar. Although the previous work used a different method for normalization and presented PDF(θ)s only at *Pe*=2 and *Pe*=200, qualitatively it is enough to compare our results inferred between *Pe*=0.001 and *Pe*=10 as well as between *Pe*=10 and *Pe*=1000. For the PDF(θ) at low *Pe*, the trend of the shape of the PDF(θ) being sliced at confinement appears the same. For the PDF(θ) at high *Pe*, the overall trends also seem the same, except α/a=0.2. The difference is unclear due to the normalization method used in the previous work. Additionally, it should be pointed out that our PDFs are based on 3D simulation, whereas the previous work was based on 2D simulation.

3.2. AVERAGE ORIENTATION MOMENTS NEAR A WALL

Figures 13-15 are resulting from the simulation performed and show the average orientation moments, $<p_x p_y>$, $<p_y^2>$, and $<p_x p_y^3>$, as a function of *Pe* for various values for α. The average orientation moments at α/a=1 (unbounded) reproduce previously determined results [26]. As α decreases (more confined), all the values are decreased. As can be inferred from Eq. 3, $<p_x p_y>$ is related to the PDF(θ) and $<p_y^2>$ is related to the PDF(φ). As a PDF is narrowed by confinement, the related average orientation moments are reduced. The relations among *Pe*, α, and each orientation moment in Figures 13-15 can be used to calculate any transport variables of rods near boundaries. Although no formulas to express all of the values in the entire *Pe* and α ranges have been derived, interpolation between the obtained data points can give reasonable approximation to the

values at arbitrary *Pe* and α. One application of utilizing the orientation moments is demonstrated in the next section.
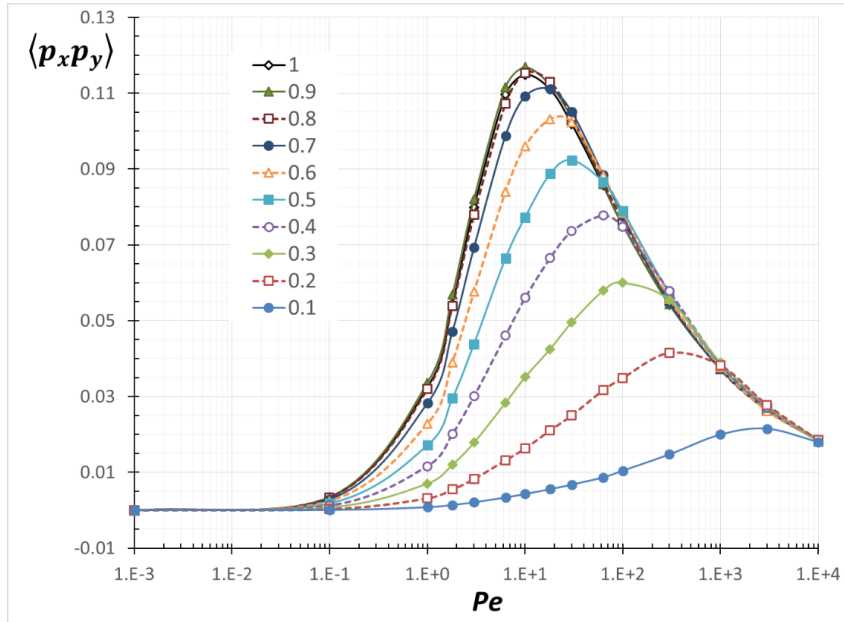
Figure 13. Average orientation moment $<p_x p_y>$ as a function of *Pe* with various α/a.
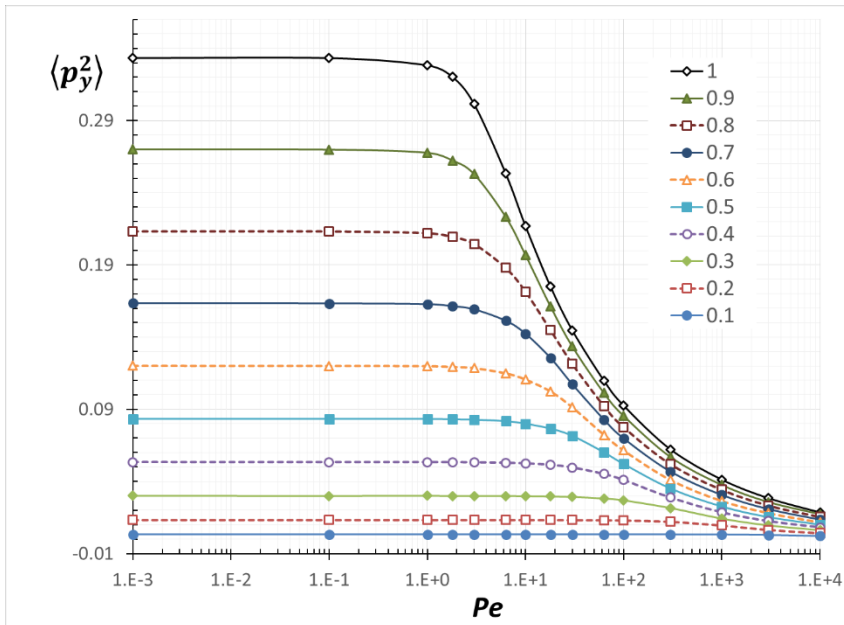
Figure 14. Average orientation moment $<p_y^2>$ as a function of *Pe* with various α/a.
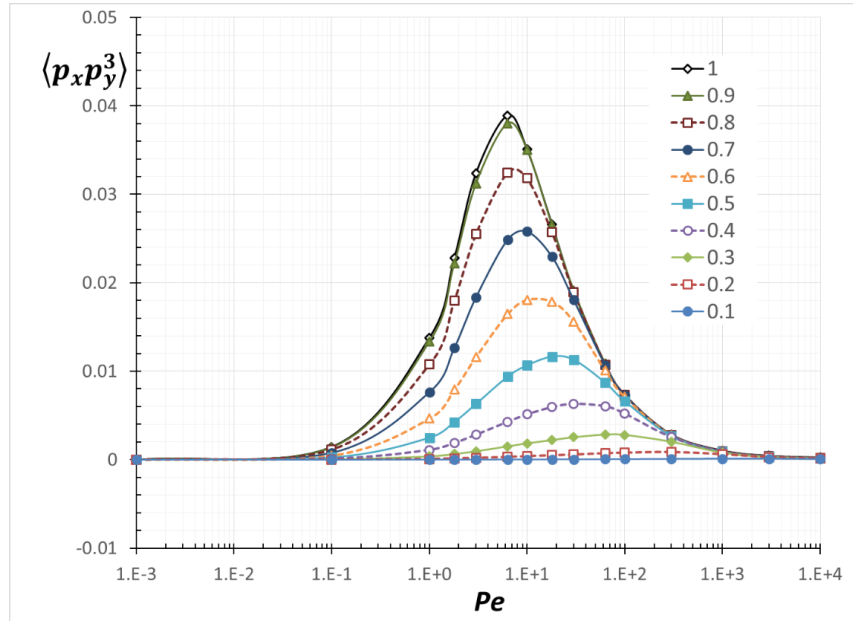
Figure 15. Average orientation moment $<p_x p_y^3>$ as a function of Pe with various α/a.

3.3. APPLICATION TO IMPROVING A SHEAR-INDUCED MIGRATION THEORY

A previous model equation for a shear-induced migration of a rod-like particle under shear flow near a boundary [25] did not consider the rod orientation dependence on the wall steric effect in the near-wall region. Therefore, the rod configurations in the near-wall region predicted by the model equation showed discrepancy from the result from the previous simulation. For example, Figure 14 compares the profiles of $<p_y^2>$ as a function of r_c/a for the case of $Pe^*=0$ (no flow), as well as a pressure-driven flow with $Pe^*=100$ in a microchannel of $H=12a$. Note that this assigned value of Pe^* for a pressure-driven flow is based on the cross-sectional average shear rate in the channel. Therefore, we distinguish the local $Pe(y)$, which is dependent on y-position for pressure-driven flow:

$$Pe(y) = 2Pe^* \left| \frac{2y}{H} - 1 \right| \tag{7}$$
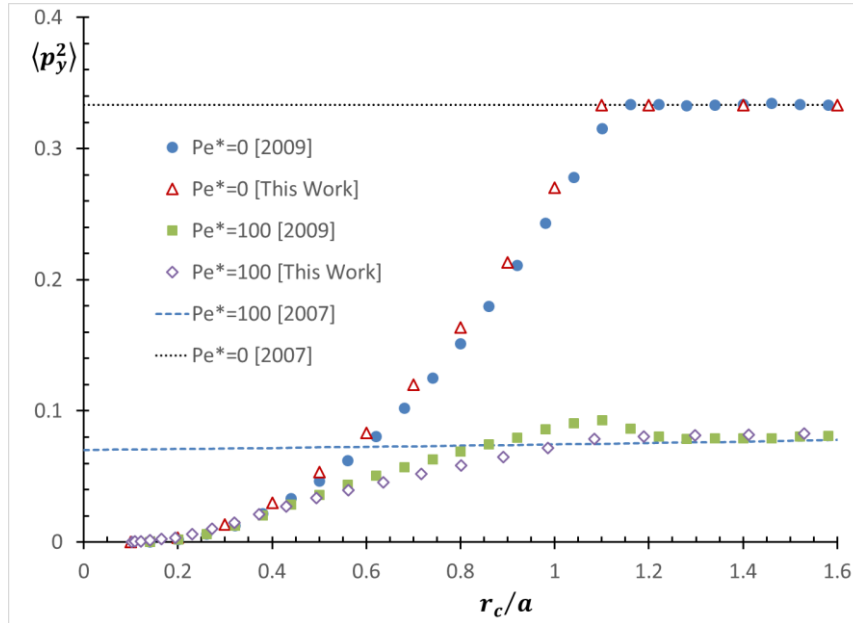
Figure 16. The $<p_y^2>$ profile as a function of r_c/a for a shear flow in a channel with $H = 12a$. Predictions from this work [open symbols], from the previous model [lines] by Park et al. (2007)[25] and the previous simulation results [solid symbols] by Park and Butler (2009)[24] are compared. Note that the half rod length distance from a wall is at $1.1a$ due to the rod diameter. The small discrepancy between the previous bulk values at $r_c > 1.1a$ and the values from this work are from the interpolation.

Since the previous model did not consider the wall confinement effect on the orientation distribution, the values of $<p_y^2>$ in the channel were assumed to follow $Pe(y)$ from Eq. 7, even near the wall (see Figure 14). However, the previous simulation showed the reduction of $<p_y^2>$ values at $r_c<1.1a$, due to the wall confinement. The reason why the confinement region is $r_c<1.1a$ and not $r_c<1.0a$, is due to the assumption that the closest position where the rod tip can be located in the previous simulation was set to $r_c=0.1a$, considering its diameter.

Our new prediction of $<p_y^2>$ in Figure 14 can be applied to predict the $<p_y^2>$ distributions in the channel. The results are also compared with the previous results in Figure 16. As mentioned in an earlier section, our prediction is shifted by the same

amount in order to match the closest available position. The profiles of $\langle p_y^2 \rangle$ obtained through our new results match those from the previous simulation for $Pe^*=0$. This indicates that our assumption made in our proposed simulation method is valid for the low Pe condition.

The newly predicted profile of $\langle p_y^2 \rangle$ at $Pe^*=100$ shows good agreement with the previous simulation results at $r_c<0.9a$. We believe that this is the first time the orientation moments near a wall have been calculated. Furthermore, this result shows that our orientation moment which was calculated under simple shear flow can be applied to pressure-driven flow. This also supports Stover and Cohen's argument [16], that shear gradient in pressure-driven flow does not affect the orientation distribution. However, there is some quantitative disagreement around $r_c=1.1a$, as the values of $\langle p_y^2 \rangle$ from the previous simulation are slightly higher. This discrepancy can be explained by the pole-vault motion. As shown in Figure 5, the p_y component becomes larger while the pole-vault motion results in an increasing r_c, which results in the increase of $\langle p_y^2 \rangle$ values. Since this effect is not considered in our simulation and the pole-vault motion only happens under shear flow, it can be inferred that the pole-vault motion was the cause of the bumps in the curvature of the graphed simulation results. Although some discrepancy was detected around $r_c=1.1a$ and high Pe, we claim that that discrepancy is not severe and our model can predict the rod orientation fairly well in the near-wall region.

4. CONCLUSIONS

We investigate the wall confinement effect on the orientation distribution for a rod near a wall (within a half rod length distance from a wall) under a shear flow.

Brownian dynamics simulations were performed by only considering the rod rotation with given various values of Pe and α. This simulation method is proposed based on the previous simulation studies findings that rod-wall hydrodynamic interaction did not affect the orientation distribution and the rod-wall collision causes the rod translation not the rod rotation.

The simulation results were analyzed to give the orientation angle distributions, Jeffery orbit distributions, and the average orientation moments for various values of Pe and α. The PDF(θ) showed that if a wall confinement ($\sin^{-1}(\alpha/a)$) is smaller than the characteristic $\theta_{\max}$, then the distribution becomes concentrated at $\sin^{-1}(\alpha/a)$. The average orientation moments values were decreased with more confinement compared to the values under non-confinement ($\alpha/a \geq 1.0$).

The average orientation moments obtained from this study were applied to improve a shear-induced migration theory for rod-like particles in a microchannel flow. The original theory did not take into consideration the wall confinement effect on the orientation moments. Comparison of the orientation moment distribution in the cross-sectional direction from the new prediction and the previous simulation confirmed the following: (1) The rod translation due to Brownian collision does not affect the rod orientation, which agrees with the finding by Hijazi and Khater [28,29]. (2) The pole-vault motion slightly affects the rod orientation near the position of the half rod length, but not to a severe level. Future calculations of the orientation moments in this study will be improved by considering the pole-vault motion, as well as details of rod shape, such as spheroid or cylinder.

The orientation distribution and moments newly obtained from our study can be applied to improve the prediction of flow behaviors or structural configurations of rod-like particle in various flow systems. The model equations in the shear-induced rod migration theory and the subsequent theories on particle separation contains the terms of the average orientation moments [12,13]. A typical approach for evaluating the particle distribution in a flow system is to use the convective-diffusion equation, where diffusivity is usually assumed to be isotropic and constant in the channel [41].

ACKNOWLEDGMENTS

NOTATION

a: the half length of the long principal axis of a rod

b: the half length of the short principal axis of a rod

d: the length of the short principal axis (diameter or thickness) of a rod

D_R: Rotational diffusivity of a rod

I: identity matrix

k_B: Boltzmann constant

L: the length of the long principal axis of a rod

m: index of the sample time

$M(n)$: the total number of sampled orientation data for the n-th particle.

n: index of a particle

N: the number of particles in each set of simulation

r_c*:* the rod center-of-mass position

p: rod orientation vector with a magnitude of unity

p_i: the i-direction component of **p**

PDF*:* probability distribution function (normalized so that its integration gives 1)

Pe: rotational Peclet number

Pe*: rotational Peclet number averaged over cross section for a pressure driven flow

Pe(y): local rotational Peclet number at a cross sectional position y in a pressure driven flow

t: dimensionless time

$t_{m,n}$: the *m*-th sampling time for the *n*-th particle

$\mathcal{T}$: Brownian torque

T: Absolute temperature of the flow

w: random vector with zero mean and variance of 1

$\hat{x}$: a unit vector in the x-direction

x: flow direction in the Cartesian coordinate system

y: shear direction in the Cartesian coordinate system

z: vorticity direction in the Cartesian coordinate system

Greek Letters

$\dot{\gamma}$: shear rate

α: wall confinement (distance from the wall surface to the rod center-of-mass position)

θ : the angle between a rod's principal axis and the flow direction on the xy-plane

φ : the angle between a rod's principal axis and the vorticity direction (z)

χ : the angle between a rod's principal axis and the flow direction on the xz-plane

ψ : the angle between a rod's principal axis and the shear direction (y).

μ: solvent viscosity

REFERENCES

[1]   Agarwal, U.; Dutta, A.; Mashelkar, R. Migration of macromolecules under flow: The physical origin and engineering implications. *Chem. Eng. Sci.* **1994**, *49*, 1693-1717, 10.1016/0009-2509(94)80057-X.

[2]   Petrie, C.J. The rheology of fibre suspensions. *J. NonNewton. Fluid Mech.* **1999**, *87*, 369-402, 10.1016/S0377-0257(99)00069-5.

[3]   Sharma, V.; Park, K.; Srinivasarao, M. Colloidal dispersion of gold nanorods: Historical background, optical properties, seed-mediated synthesis, shape separation and self-assembly. *Mater. Sci. Eng., R* **2009**, *65*, 1-38, 10.1016/j.mser.2009.02.002.

[4]   Lee, G.; Cho, Y.-S.; Park, S.; Yi, G.-R. Synthesis and assembly of anisotropic nanoparticles. *Korean J. Chem. Eng.* **2011**, *28*, 1641-1650, 10.1007/s11814-011-0183-5.

[5]   Berthet, H. Single and collective fiber dynamics in confined microflows. PhD Thesis, Université Pierre et Marie Curie, Paris, France, 2012.

[6]   Barua, S.; Mitragotri, S. Synergistic targeting of cell membrane, cytoplasm, and nucleus of cancer cells using rod-shaped nanoparticles. *ACS nano* **2013**, *7*, 9558-9570, 10.1021/nn403913k.

[7]   Monjezi, S.; Bhedani, B.; Palaniappan, M.B.; Jones, J.D.; Park, J. Computational studies of DNA separations in micro-fabricated devices: Review of general approaches and recent applications. *Adv. Chem. Eng. Sci.* **2017**, *7*, 362-393.

[8]   Hjerrild, N.E.; Taylor, R.A. Boosting solar energy conversion with nanofluids. *Phys. Today* **2017**, *70*, 40-45, 10.1063/Pt.3.3790.

[9]   Schimpf, M.E.; Caldwell, K.; Giddings, J.C. *Field-flow fractionation handbook*. John Wiley & Sons: New York, USA, 2000; p 616, ISBN. 0471184306.

[10]   Gigault, J.; Cho, T.J.; MacCuspie, R.I.; Hackley, V.A. Gold nanorod separation and characterization by asymmetric-flow field flow fractionation with uv–vis detection. *Anal. Bioanal. Chem.* **2013**, *405*, 1-12, 10.1007/s00216-012-6547-9.

[11]   Nguyen, T.M.; Liu, J.; Hackley, V.A. Fractionation and characterization of high aspect ratio gold nanorods using asymmetric-flow field flow fractionation and single particle inductively coupled plasma mass spectrometry. *Chromatography* **2015**, *2*, 422-435, 10.3390/chromatography2030422.

[12]   Alfi, M.; Park, J. Theoretical analysis of the local orientation effect and the lift-hyperlayer mode of rodlike particles in field-flow fractionation. *J. Sep. Sci.* **2014**, *37*, 876-883, 10.1002/jssc.201300902.

[13]   Park, J.; Mittal, A. An improved model for the steric-entropic effect on the retention of rod-like particles in field-flow fractionation: Discussion of aspect ratio-based separation. *Chromatography* **2015**, *2*, 472-487, 10.3390/chromatography2030472.

[14]   Jeffery, G.B. In *The motion of ellipsoidal particles immersed in a viscous fluid*, Proceedings of the royal society of London A: Mathematical, physical and engineering sciences, London, UK, 1922; The Royal Society: London, UK, pp 161-179.

[15]   Sundararajakumar, R.; Koch, D.L. Structure and properties of sheared fiber suspensions with mechanical contacts. *J. NonNewton. Fluid Mech.* **1997**, *73*, 205-239, 10.1016/S0377-0257(97)00043-8.

[16]   Stover, C.A.; Koch, D.L.; Cohen, C. Observations of fibre orientation in simple shear flow of semi-dilute suspensions. *J. Fluid Mech.* **1992**, *238*, 277-296, 10.1017/s002211209200171x.

[17]   Rahnama, M.; Koch, D.L.; Shaqfeh, E.S. The effect of hydrodynamic interactions on the orientation distribution in a fiber suspension subject to simple shear flow. *Phys. Fluids* **1995**, *7*, 487-506, 10.1063/1.868647.

[18]   Leal, L.; Hinch, E. The effect of weak brownian rotations on particles in shear flow. *J. Fluid Mech.* **1971**, *46*, 685-703, 10.1017/s0022112071000788.

[19]   Einarsson, J.; Candelier, F.; Lundell, F.; Angilella, J.; Mehlig, B. Rotation of a spheroid in a simple shear at small reynolds number. *Phys. Fluids* **2015**, *27*, 063301, 10.1063/1.4921543.

[20]   Boeder, P. Über strömungsdoppelbrechung. *Zeitschrift für Physik A Hadrons and Nuclei* **1932**, *75*, 258-281.

[21]   Hijazi, A.; Zoaeter, M. Brownian dynamics simulations for rod-like particles in dilute flowing solution. *Eur. Polym. J.* **2002**, *38*, 2207-2211, 10.1016/S0014-3057(02)00130-1.

[22]   Chen, S.B.; Jiang, L. Orientation distribution in a dilute suspension of fibers subject to simple shear flow. *Phys. Fluids* **1999**, *11*, 2878-2890, 10.1063/1.870146.

[23]   Asokan, K.; Ramamohan, T.; Kumaran, V. A novel approach to computing the orientation moments of spheroids in simple shear flow at arbitrary peclet number. *Phys. Fluids* **2002**, *14*, 75-84, 10.1063/1.1426391.

[24]   Park, J.; Butler, J.E. Inhomogeneous distribution of a rigid fibre undergoing rectilinear flow between parallel walls at high peclet numbers. *J. Fluid Mech.* **2009**, *630*, 267-298, 10.1017/S0022112009006545.

[25]   Park, J.; Bricker, J.M.; Butler, J.E. Cross-stream migration in dilute solutions of rigid polymers undergoing rectilinear flow near a wall. *Phys. Rev. E* **2007**, *76*, 040801, 10.1103/PhysRevE.76.040801.

[26]   Park, J. Dynamics of suspensions of rodlike polymers with hydrodynamic interactions. PhD Thesis, University of Florida, Gainesville, FL, 2009.

[27]   Park, J.; Butler, J.E. Analysis of the migration of rigid polymers and nanorods in a rotating viscometric flow. *Macromolecules* **2010**, *43*, 2535-2543, 10.1021/ma901369a.

[28]   Hijazi, A.; Khater, A. Brownian dynamics simulations of rigid rod-like macromolecular particles flowing in bounded channels. *Comput. Mater. Sci* **2001**, *22*, 279-290, 10.1016/S0927-0256(01)00241-5.

[29]   Hijazi, A.; Khater, A. Simulations of distribution functions for rod-like macromolecules in linear flow near solid surfaces. *Comput. Mater. Sci* **2001**, *20*, 213-227, 10.1016/S0927-0256(00)00178-6.

[30]   Schiek, R.L.; Shaqfeh, E.S. A nonlocal theory for stress in bound, brownian suspensions of slender, rigid fibres. *J. Fluid Mech.* **1995**, *296*, 271-324, 10.1017/S0022112095002138.

[31]   Schiek, R.L.; Shaqfeh, E.S. Cross-streamline migration of slender brownian fibres in plane poiseuille flow. *J. Fluid Mech.* **1997**, *332*, 23-39, 10.1017/s0022112096003291.

[32]   Nitsche, L.C.; Hinch, E. Shear-induced lateral migration of brownian rigid rods in parabolic channel flow. *J. Fluid Mech.* **1997**, *332*, 1-21, 10.1017/s0022112096003369.

[33] Stover, C.A.; Cohen, C. The motion of rodlike particles in the pressure-driven flow between two flat plates. *Rheol. Acta* **1990**, *29*, 192-203, 10.1007/bf01331355.

[34] Holm, R.; Söderberg, D. Shear influence on fibre orientation. *Rheol. Acta* **2007**, *46*, 721-729, 10.1007/s00397-007-0166-y.

[35] Kaya, T.; Koser, H. Characterization of hydrodynamic surface interactions of escherichia coli cell bodies in shear flow. *Phys. Rev. Lett.* **2009**, *103*, 138103, 10.1103/PhysRevLett.103.138103.

[36] Batchelor, G. Slender-body theory for particles of arbitrary cross-section in stokes flow. *J. Fluid Mech.* **1970**, *44*, 419-440, 10.1017/s002211207000191x.

[37] Doi, M.; Edwards, S.F. *The theory of polymer dynamics*. Oxford university press: Oxford, UK, 1988; Vol. 73, p 408, ISBN. 0198520336.

[38] Larson, R.G. *The structure and rheology of complex fluids*. Oxford university press: New York, USA, 1999; p 663, ISBN. 019512197X.

[39] Allen, M.P.; Tildesley, D.J. *Computer simulation of liquids*. Oxford university press: Oxford, UK, 1989; p 408, ISBN. 0198556454.

[40] Cobb, P.D.; Butler, J.E. Simulations of concentrated suspensions of rigid fibers: Relationship between short-time diffusivities and the long-time rotational diffusion. *J. Chem. Phys* **2005**, *123*, 054908, 10.1063/1.1997149.

[41] Vidal-Meza, M.P.; Zhou, R.; Barua, S.; Wang, C.; Park, J. In *Simulation of interstitial nanoparticle flow for development of tumor-on-a-chip device*, The Proceedings of 2016 COMSOL Conference, Boston, October, 2016; COMSOL: Boston.

II. A MODEL FOR THE DEPLETION LAYER PREDICTION IN A DILUTE SUSPENSION OF RIGID ROD-LIKE PARTICLES UNDER SHEAR FLOWS IN THE ENTIRE RANGE OF PECLET NUMBERS[2]

Saman Monjezi[a], Alyssa K. Nelson[a], Joontaek Park[a],*

[a] Department of Chemical and Biochemical Engineering, Missouri University of Science

and Technology

Rolla, MO, 65409, USA

ABSTRACT

We derived a model to predict the concentration profile, or the center-of-mass distribution, of rod-like particles near a wall under shear flows. Various excluded volume mechanisms of a rod near a wall for each Peclet number (a ratio of shear rate and diffusivity) regime were incorporated into the model through a steric factor concept. At low and moderate Peclet numbers, the steric factor is mainly determined by the ratio of the restricted/unrestricted rod orientation distributions. However, at high Peclet number, the ratio between the rod penetration time in a depletion layer and the Jeffery orbit frequency mainly affects the steric factor. The predicted concentration profiles showed a good agreement with the results from previous works.

Keywords: Rod-like Particle, Orientation Distribution, Depletion Layer, Excluded volume effect, Microchannel Flow

2010 MSC: 82-80, 76-10, 76D07, 76T70

---
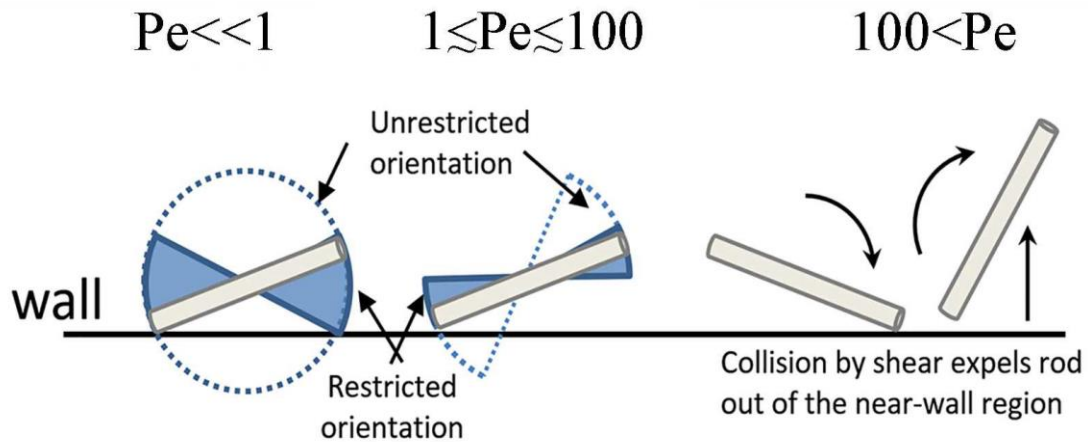
1. INTRODUCTION

A depletion layer is where particle concentration near a solid wall becomes lower than the average cross-sectional concentration. Since such depletion layers have been observed in rod-like particle suspension flows (Ausserré et al., 1991), many studies have been performed on the lateral cross-stream migration and the center-of-mass distribution (concentration profile) of rod-like particles in channel flows (Agarwal et al., 1994). Simulations based on Brownian dynamics (BD) have been performed to obtain the concentration profile in the depletion layer under simple shear flows. A work by Pablo et al. (1992) identified the profile change in terms of Pe (*Pe*: Peclet number is defined as the ratio between the shear rate, $\dot{\gamma}$ and the rotational diffusivity, D_R) (Pablo et al., 1992). Although a later work showed a different trend because it was performed only on a shear plane (Hijazi and Khater, 2001), both works showed that the depletion layer increases with *Pe* in a high *Pe* range. There was a series of theoretical works on the profile in parabolic channel flows (Schiek and Shaqfeh, 1997, Nitsche and Hinch, 1997). However, those predictions focused on the migration due to the rod anisotropic diffusivity and the profile in the low *Pe* range. The mechanism causing the depletion layer in those earlier

works is mainly the excluded volume effect. Therefore, the depletion layer is formed within a half rod length from a wall (near-wall region). Hydrodynamic interaction (HI) between a wall and a rod is considered in a model by Park et al. (2007), which shows that shear-induced migration extends the depletion beyond the near-wall region in a high Pe range. However, if Pe is not high enough for rods to migrate away from the near-wall region, the predicted profile shows discrepancy from the profile obtained from the BD simulation (Park and Butler, 2009). This is because the model from Park et al. (2007) did not consider the excluded volume effect.

As reviewed above, there is no single analytical model to predict the profile in the depletion layer for the entire range of Pe. While many applications of micro- or nanorods have been developed, the incompleteness of the depletion layer prediction prevents further development. For example, the abnormal elution order of gold nanorods in a field-flow fraction, a particle separation device, has not yet been explained (Gigault et al., 2012, Nguyen et al., 2015, Park and Mittal, 2015).

2. MODEL DEVELOPMENT

Fig. 1 schematically illustrates the variables to describe our problem. This study assumes that a dilute suspension of neutrally buoyant rigid rod-like particles is flowing in a channel with the Stokes flow condition. The fluid is also assumed as isothermal and Newtonian. The channel height, H, is larger than two rod lengths (H>2L: weakly confined system) and the channel width is much wider than H. The excluded volume effect will be mainly considered in our derivation but it will be demonstrated that our model can be incorporated into the model with HI.
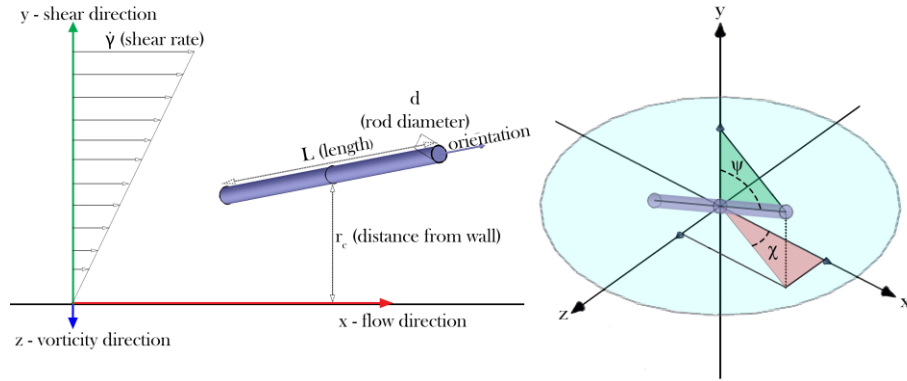
Figure 1. Schematic diagrams and definitions of variables: A rigid rod with its aspect ratio, $Ar = L/d$ (L: length and d: diameter), is flowing in a channel with a shear rate of $\dot{\gamma}$. The flow, shear, and vorticity directions are in x,y,z directions, respectively. The distance between the center-of-mass position and the wall surface (y=0) is r_c. The inset demonstrates that a rod orientation is specified with an angle between a rod tip and the y-axis (ψ) and an azimuthal angle on the xz-plane with the x-axis as a reference (χ).

We adopt an approach of "steric factor" used in the prediction of a rod concentration profile in field-flow fractionation (Beckett and Giddings, 1997). The steric factor of a rod at $y = r_c$, $S_B(y)$, is defined as the ratio of the numbers of rod configurations restricted/unrestricted at y=rc. The concentration profile obtained without considering the steric restriction by the wall, $c_0(y)$, is corrected by the steric factor to give the concentration profile considering the wall confinement, $c(y)$:

$$c(y) = C_N c_0(y) S_B(y). \tag{1}$$

Note that $c(y)$ is normalized by C_N. The range of $S_B(y)$ spans from $S_B(y = 0, H) = 0$ to $S_B(0.5L < y < H - 0.5L) = 1$ so that the excluded volume effect corrects c_0(y) in the near-wall region ($0 < y < 0.5L$ or $H - 0.5L < y < H$). As seen in Fig. 2, if S_B(y) in the original theory is just the area ratio between the restricted sphere surface and the whole sphere surface, then:

$$S_B(y) = \frac{\pi L^2 \sin\left[\frac{\pi}{2} - \psi_1\right]}{\pi L^2} = \frac{2y}{L}. \tag{2}$$
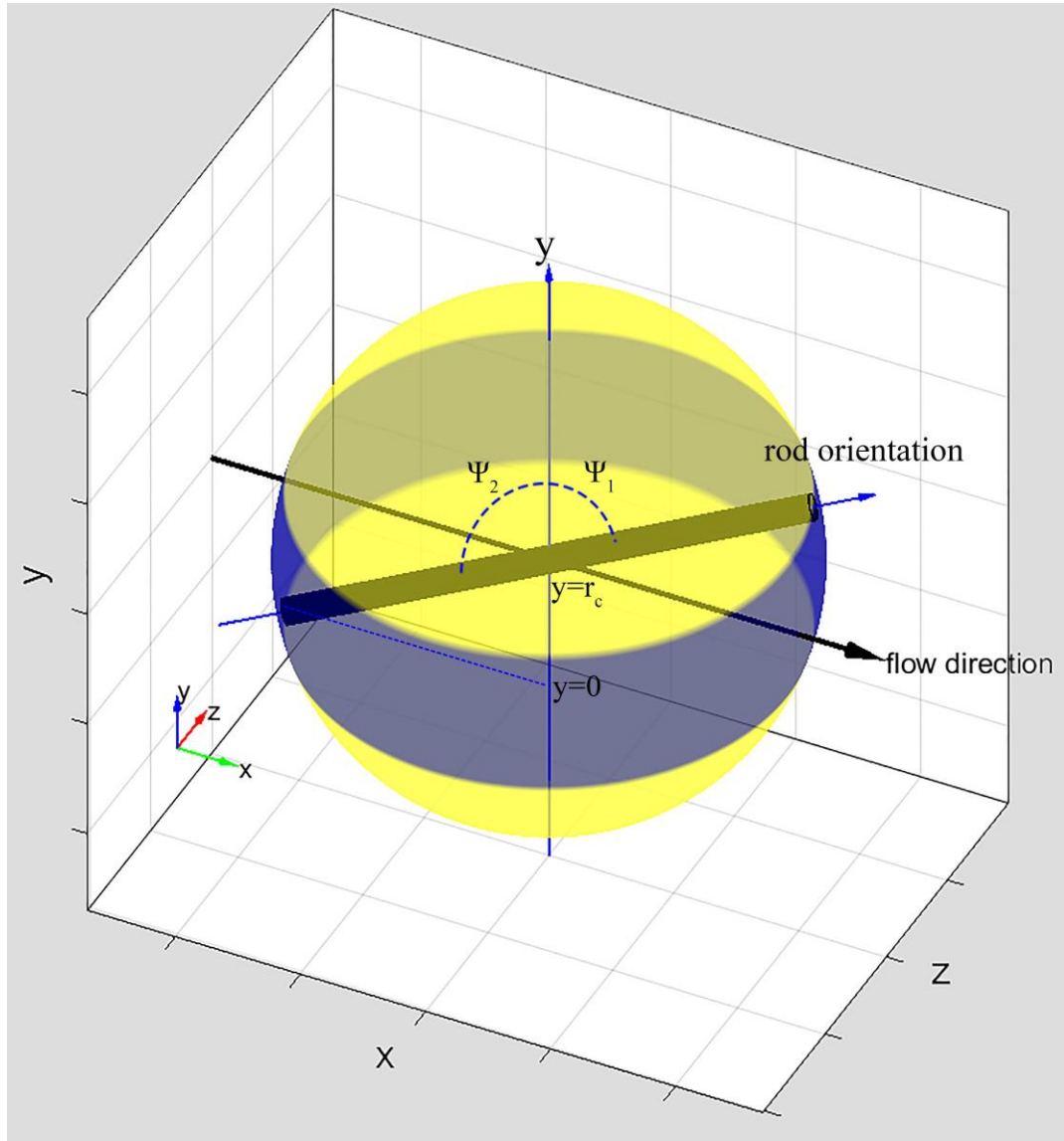
Figure 2. Demonstration of a rod orientation at $Pe \ll 1$: If a rod orientation is not restricted in the bulk at $Pe \ll 1$, the rod tip will swipe the entire sphere surface evenly. However, if r_c locates near a wall, the rod orientation is restricted within $\psi_1 < \psi < \psi_2$ (the shaded sphere surface), where the restriction angles are $\psi_1 = arccos[\frac{2y}{L}]$ and $\psi_2 = \pi - \psi_1$.

However, this is true only for Pe≪1 where the Brownian rotation of a rod tip covers the sphere surface evenly. As seen in Fig. 3, the rod orientation distribution becomes inhomogeneous with increasing Pe. Therefore, $S_B(y; Pe)$ must be evaluated

considering the rod orientation distribution at Pe of interest. The orientation distributions

on sphere surfaces in Fig. 2, Fig. 3 were obtained by performing Brownian rod

simulations shown in the algorithm given by Cobb and Butler, 2005, Park, 2009. The rod

orientation distribution on a sphere surface can be decomposed into the probability

distribution functions, PDF, of two angles which were defined in Fig. 1 to describe the

rod orientation: PDF(ψ;Pe) and PDF(χ;Pe). Since PDF(χ;Pe) is not affected by the wall

confinement, PDF(ψ;Pe), shown in Fig. 4, can be used to describe a rod orientation

distribution at $y = r_c$ and Pe as $PDF(\psi_1 < \psi < \psi_2; Pe)$. This notion is based on

previous simulation studies (Park and Butler, 2009, Hijazi and Khater, 2001, Monjezi et

al., 2018) and our investigation of the orientation distributions at a certain r_c, obtained

from the previous BD simulations (Park and Butler, 2009, Park, 2009).

Using the $PDF(\psi; Pe)$, the steric factor at $Pe > 0, S_B(y; Pe)$, can be obtained in

the following way:

$$S_B(y; Pe) = \frac{\int_{\psi_1}^{\psi_2} PDF(\psi;Pe) sin\psi d\psi}{\int_0^{\pi} PDF(\psi;Pe) sin\psi d\psi} \tag{3}$$

Note that $(0.5L)^2$ and integration of $PDF(\chi; Pe)$ cancel each other on both numerator

and denominator. It is also noted that Eq. (3) at Pe≪1 recovers Eq. (2). Although

Eq. (3) can be obtained by numerically integrating the $PDF(\psi; Pe)$, we used a semi-

analytical approach utilizing an approximate function, which is demonstrated

in Appendix A. An analytical expression for orientation distributions is considered in our

future work. Nonetheless, this work is based on having detailed knowledge of the

orientation distribution by any means, and implementation of a "steric factor" approach
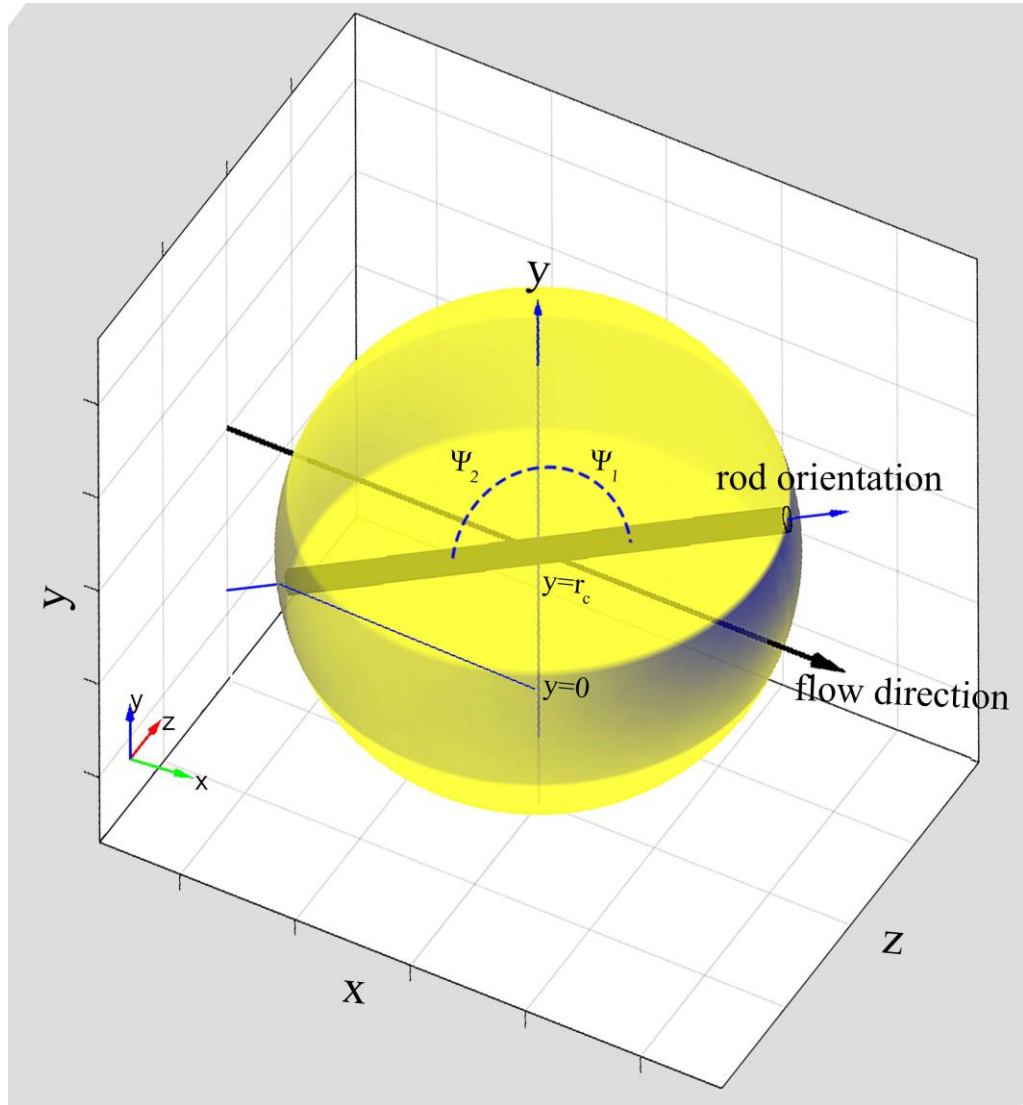
Figure 3. Demonstration of the rod orientation at $Pe = 10$: The rod orientation becomes uneven and concentrated (shaded darker) around a certain position and restricted within $\psi_1 < \psi < \psi_2$.

to predict the depletion layer near the wall for the first time to remove the *Pe* range limitation of previously proposed models.

We also discovered that $S_B(y; Pe)$ alone cannot describe the depletion layer change in a high *Pe* range. Therefore, we introduce another steric factor due to shear collision, $S_S(y; Pe)$. Note that the subscripts *B* and *S* represent "Brownian" and "Shear"
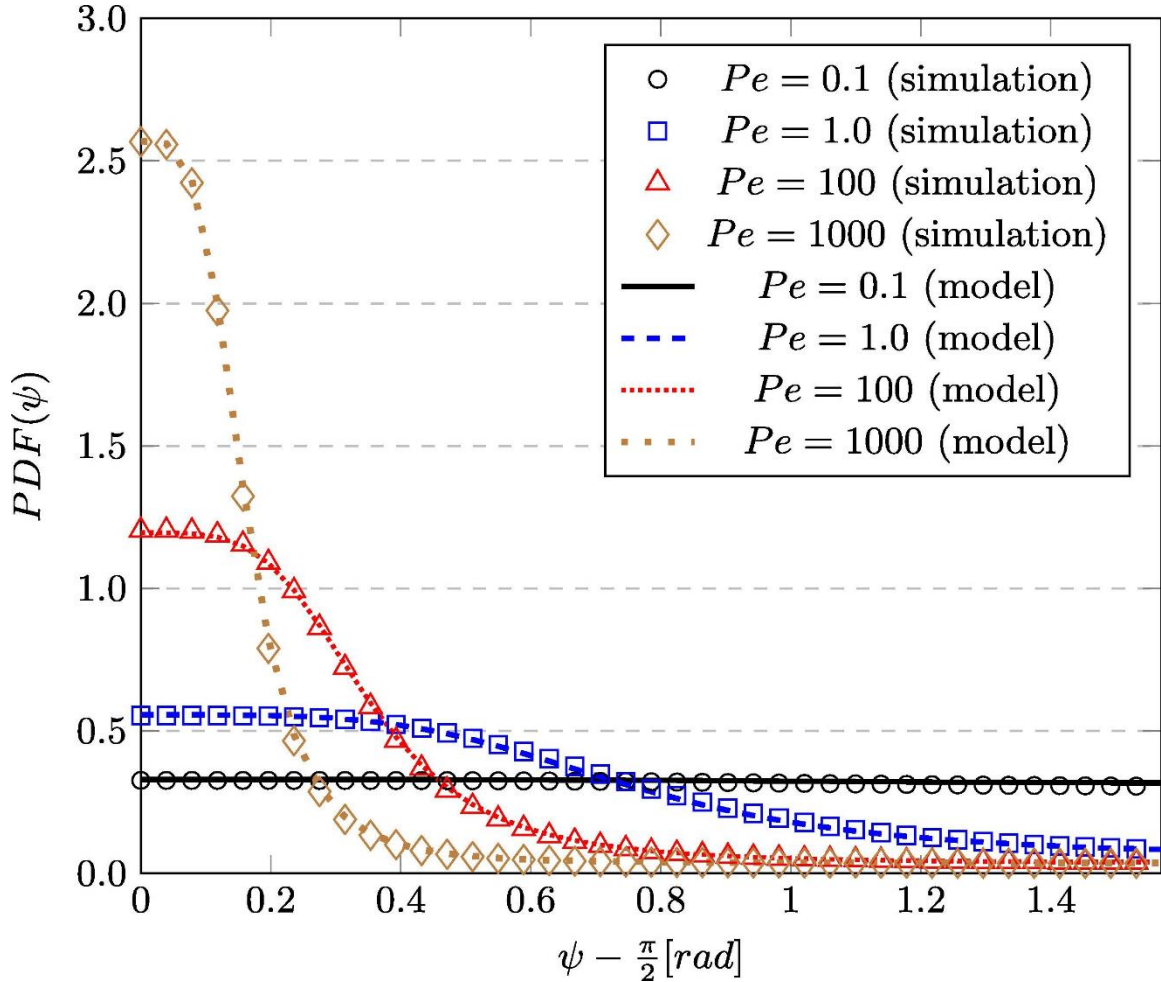
Figure 4. $PDF(\psi; Pe)$: Symbols represent PDFs obtained from the BD simulation (Park, 2009). Lines indicate the prediction using Eq. (A.1). The distribution is symmetric with the vertical axis at $\psi - \pi/2 = 0$. Each curve is normalized. For the integration on a sphere surface, $sin\,\psi$ must be multiplied.

contributions, respectively. $S_S(y; Pe)$ can be derived from the "penetration time" concept used in the discussion of Pablo et al. (1992). A rod can stay in the near-wall region while Jeffery orbit type rotation does not make its tip hit the wall (within the Jeffery orbit period: T_J). The diffusion time for a rod to penetrate into the near-wall region from $y = L/2$ to a certain y position, τ_p, can be estimated as:

$$\tau_p = \frac{(0.5L-y)^2}{2D_y}. \tag{4}$$

Here, D_y is the translational diffusivity of a rod in the cross-sectional y-direction. We

approximate D_y as the perpendicular diffusivity of a slender body (Cobb and Butler,

2005).

$$D_y \approx D_\perp = \frac{k_B T \ln(2Ar)}{4\pi\mu L} = \frac{L^2}{12} D_R. \tag{5}$$

Here, $k_B T$ is the thermal energy. Based on the Pe of the flow and the rod type (such as a

prolate spheroid), D_y is different from $D_\perp$ but our results will show that it is an adequate

approximation.

It can be inferred that the ratio between τ_p and T_J determines the probability for a

rod to stay in the near-wall region:

$$\frac{\tau_p}{T_J} = \frac{3(0.5L-y)}{2\pi L^2 (Ar + Ar - 1)} Pe. \tag{6}$$

This ratio can be used to construct $S_S(y; Pe)$ so that $S_S = 0$ for very small T_J and $S_S =$

1 for very small τ_p:

$$S_S(y; Pe) = \frac{1}{1 + \frac{\tau_p}{T_J}}. \tag{7}$$

Using $S_B(y; Pe)$ and $S_S(y; Pe)$, Eq. (1) now can be:

$$c(y) = C_N c_0(y) S_B(y; Pe) S_S(y; Pe). \tag{8}$$

C_N is a normalization constant which is obtained by integrating $c_0(y) S_B(y; Pe) S_S(y; Pe)$

between y=0 and y=H.

3. RESULTS AND DISCUSSION

We apply our model, Eq. (8) along with $S_B(y; Pe)$ and $S_S(y; Pe)$ to reproduce the

concentration profiles from the previous works (Pablo et al., 1992, Park et al., 2007, Park

and Butler, 2009). The system for the simulation in Pablo et al. (1992) has H=2L.

Without considering HI between the particle and walls, $c_0(y) = \frac{1}{2L}$. A rigid dumbbell,

which was used to model a rod, has the distance between two beads of L with a diameter

of d. The relaxation time of this dumbbell, λ_{db}, can be rewritten in terms of the variables

of a slender-body rod:

$$\lambda_{db} = \frac{6\pi\mu d L^2}{k_B T} = \frac{18 ln(2Ar)}{Ar} \frac{1}{D_R} .$$ (9)

Therefore, the dumbbell simulations at the flow conditions of $\lambda_{db}\dot{\gamma}$ =0.5,50, and 2500

correspond to the slender body of Ar=10 at Pe=0.0927,9.27,

and 463.0. $S_B(y; Pe)$ and $S_S(y; Pe)$ are calculated at those values of Pe. The results

of $c(y)$ prediction are compared with the simulation results in Pablo et al. (1992). As

seen in Fig. 5, our model predictions show good agreement with the results from Pablo et

al. (1992). At low Pe of 0.0927 or $\lambda_{db}\dot{\gamma} = 0.5$, both profiles show linear decrease from

bulk (y=0.5L) to the wall surface (y=0). This corresponds to the steric factor derived

in Beckett and Giddings (1997) for $Pe \ll 1$, as in Eq. (2).

At moderate Pe of 9.27 or $\lambda_{db}\dot{\gamma}$=50.0, the profiles show concave up and the depletion

layer becomes smaller than that at a low Pe. This is because more aligned rod

configurations at higher shear rates can stay closer to the wall in the depletion layer

(Pablo et al., 1992). The concave-up profile shape is mainly due to $S_B(y; Pe)$ because

$S_S(y; Pe)$ is still almost 1.0 at this moderate Pe range.

Finally, $S_S(y; Pe)$ becomes dominantly effective at very high Pe of 463.0 or

$\lambda_{db}\dot{\gamma}$=2500. More aligned rod configurations may fit in the closer location to the wall but
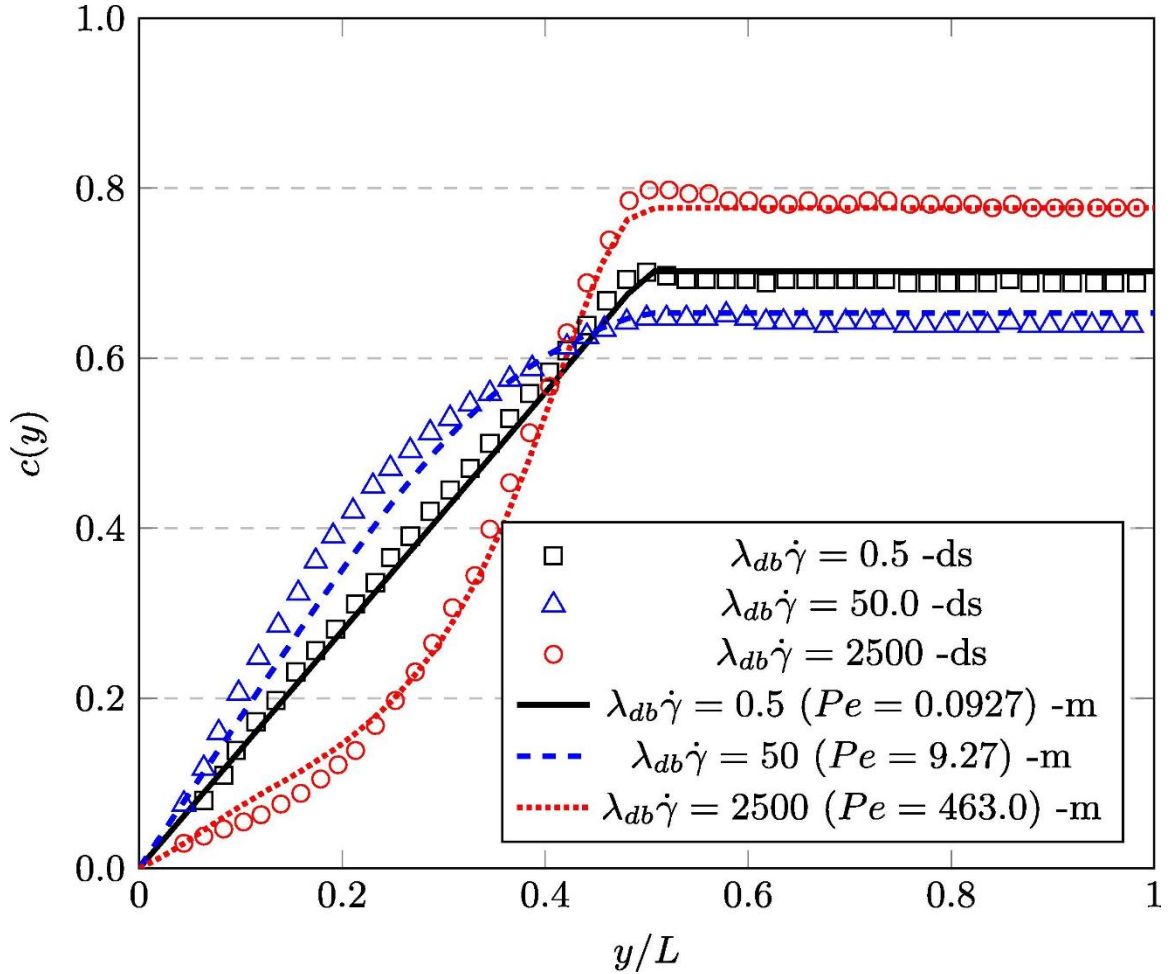
Figure 5. Comparison of $c(y)$ under simple shear flows in H=2L: Symbols indicate the dumbbell simulations with different $\lambda_{db}\dot{\gamma}$ by Pablo et al. (1992). Lines indicate the predictions at corresponding Pe for a slender body of Ar=10. All distributions were normalized for comparison.

more frequent shear rotation causes the rod to be expelled from the depletion layer. Some

discrepancies may be attributed to the approximation of D_y in Eq. (5) and the difference

in the dynamics of the dumbbell model from the slender body (Cobb and Butler, 2005).

Our model is also applied to predict the concentration profile considering HI with

a wall. As seen in Fig. 6, Park et al. (2007) derived a rod migration model to

predict $c_0(y)$ in a pressure driven flow of Pe^*=100.0 (Pe^* is a cross sectional

average *Pe* in the channel) considering HI between the wall and the rod (The actual

expression for the distribution in Fig. 6 was Eq. 3.18 of Park and Butler (2009)). HI

between a rod and a wall generates a flow disturbance resulting in a lift of the rod away

from the wall. Since the HI is a long-range interaction, the rod migration due to HI can

extend the depletion layer thickness beyond the near-wall region (Park et al., 2007).
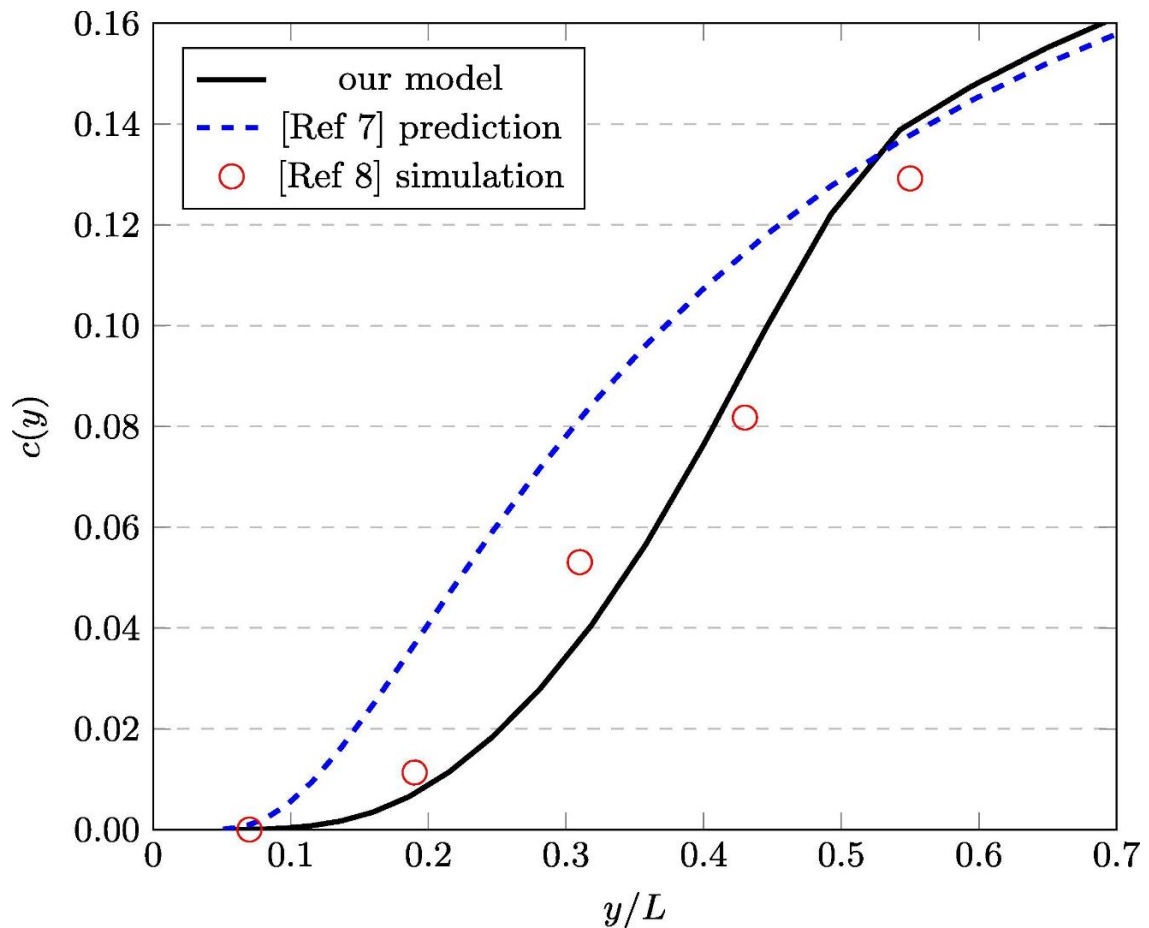
Figure 6. Comparison of $c(y)$ in a pressure driven flow of Pe^*=100.0 and H=6L: The predictions by our model and by Park et al. (2007) and the simulation by Park and Butler (2009) were compared. Note that each $c(y)$ is shifted to y=0.05d to consider the rod thickness effect.

However, the BD simulation at the same condition showed discrepancy in $c(y)$, as in Fig.
6. Park and Butler (2009) also compared $c(y)$ obtained from the simulations with/without
HI to conclude that the excluded volume effect on the $c(y)$ is always dominant in the
near-wall region. Therefore, it is expected that the addition of the excluded volume effect
to the rod migration model can improve its depletion layer prediction. We
apply $S_B(y; Pe)$ and $S_S(y; Pe)$ to the model to correct the excluded volume effect. Our
model shows the improvement in the agreement with the simulation data. The
discrepancy may be attributed to the approximation in the D_y or the original error in the
simulation.
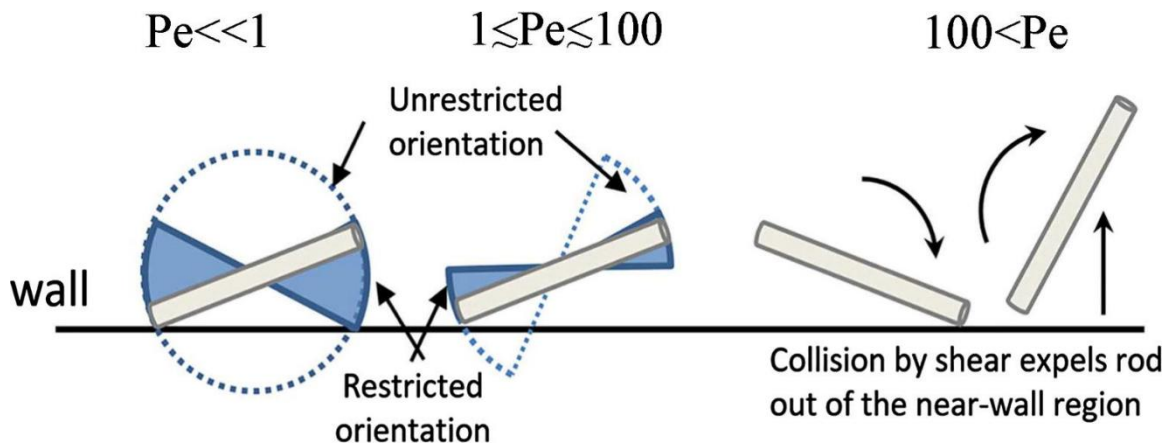
Figure 7. Summary of each excluded volume mechanism for a rod at low Pe≪1,
moderate 1<Pe<100, and high Pe>100 regimes. The values for each range are
approximate.

ACKNOWLEDGEMENTS

APPENDIX: ORIENTATION DISTRIBUTION APPROXIMATION

We found an approximate function which fits the $PDF(\psi; Pe)$s from the BD simulations in Fig. 4. Additionally, coefficients were also obtained from the distributions at various values of Pe for the best regression possible, which were not all presented in Fig. 4. Hence, the approximate PDF can be applied to make Eq. (3) calculated analytically in the entire ranges of Pe. $PDF(\psi; Pe)$ can be approximated to the following form:

$$PDF(\psi; Pe) = \frac{a_1(Pe)a_2(Pe) + a_3(Pe)\left|\psi - \frac{\pi}{2}\right|^{-4}}{a_2(Pe) + \left|\psi - \frac{\pi}{2}\right|^{-4}} \tag{A.1}$$

This function is defined in $0 < \psi < \pi$. Here, $a_i(Pe)$ indicates the parameter, which is a function of Pe. The following is the expression for a1:

$$Log_{10}(a_1(Pe)) = f_1 + \frac{g_1 \boldsymbol{Pe}^{m_1}}{h_1^{m_1} + \boldsymbol{Pe}^{m_1}} \tag{A.2}$$

The next expression holds for a2 and a3:

$$Log_{10}(a_i(Pe)) = f_i + \frac{g_i\{\boldsymbol{Pe} + h_i\}}{1 + exp(m_i\{\boldsymbol{Pe} + h_i\})} \tag{A.3}$$

Note that $\boldsymbol{Pe} = log_{10}(Pe) + 10$ and the parameters, f_i, g_i, and h_i, corresponding to a_i are listed in Table A.1.

Note that each PDF was obtained from more than 5000 samples to have the seemingly smooth curve (standard deviations at each angle value are almost 0). The correlation coefficients of each fitting function are determined to be 0.999 at each Pe. Numerical integration using trapezoidal method with the step size smaller than 0.0002 rad gives convergent results.

Table A.1. Parameters for Eqs. (A.2), (A.3) corresponding to a_i.

	$(i=1)a_1$	$(i=2)a_2$	$(i=3)a\_3$
f_i	−0.4980	−0.2994	−0.4831
g_i	−0.9524	1.3420	0.3325
h_i	10.7500	−10.4102	−10.3125
m_i	54.5300	31.0000	31.0000

REFERENCES

[1]   D. Ausserr´e, J. Edwards, J. Lecourtier, H. Hervet, F. Rondelez, Hydrody- namic
       thickening of depletion layers in colloidal solutions, Europhys. Lett. (EPL) 14 (1)
       (1991) 33–38. doi:10.1209/0295-5075/14/1/006. URL
       https://doi.org/10.1209%2F0295-5075%2F14%2F1%2F006.

[2]   U. Agarwal, A. Dutta, R. Mashelkar, Migration of macromolecules under flow:
       the physical origin and engineering implications, Chem. Eng. Sci. 49 (11) (1994)
       1693–1717. doi:10.1016/0009-2509(94)80057-x. URL
       https://doi.org/10.1016%2F0009-2509%2894%2980057-x.

[3]   J. J. D. Pablo, H. C. O¨ttinger, Y. Rabin, Hydrodynamic changes of the depletion
       layer of dilute polymer solutions near a wall, AIChE J. 38 (2) (1992) 273–283.
       doi:10.1002/aic.690380213. URL https://doi.org/10.1002%2Faic.690380213.

[4]   Hijazi, A. Khater, Brownian dynamics simulations of rigid rod-like
       macromolecular particles flowing in bounded channels, Comput. Mater. Sci. 22
       (3-4) (2001) 279–290. doi:10.1016/s0927-0256(01)00241-5. URL
       https://doi.org/10.1016%2Fs0927-0256%2801%2900241-5.

[5]   R. L. Schiek, E. S. G. Shaqfeh, Cross-streamline migration of slender brownian
       fibres in plane poiseuille flow, J. Fluid Mech. 332 (1997) 23–39.
       doi:10.1017/s0022112096003291. URL
       https://doi.org/10.1017%2Fs0022112096003291.

[6]   L. C. Nitsche, E. J. Hinch, Shear-induced lateral migration of brownian rigid rods
       in parabolic channel flow, J. Fluid Mech. 332 (1997) 1–21.
       doi:10.1017/s0022112096003369. URL
       https://doi.org/10.1017%2Fs0022112096003369.

[7] J. Park, J. M. Bricker, J. E. Butler, Cross-stream migration in dilute solu- tions of rigid polymers undergoing rectilinear flow near a wall, Phys. Rev. E 76 (2007) 040801. doi:10.1103/PhysRevE.76.040801. URL https://link.aps.org/doi/10.1103/PhysRevE.76.040801.

[8] J. Park, J. E. Butler, Inhomogeneous distribution of a rigid fibre undergoing rectilinear flow between parallel walls at high p´eclet numbers, J. Fluid Mech. 630 (2009) 267. doi:10.1017/s0022112009006545. URL https://doi.org/10.1017%2Fs0022112009006545.

[9] J. Gigault, T. J. Cho, R. I. MacCuspie, V. A. Hackley, Gold nanorod separation and characterization by asymmetric-flow field flow fractionation with UV–vis detection, Anal. Bioanal. Chem. 405 (4) (2012) 1191–1202. doi:10.1007/s00216-012-6547-9. URL https://doi.org/10.1007%2Fs00216-012-6547-9.

[10] T. Nguyen, J. Liu, V. Hackley, Fractionation and characterization of high aspect ratio gold nanorods using asymmetric-flow field flow fractionation and single particle inductively coupled plasma mass spectrometry, Chro- matography 2 (3) (2015) 422–435. doi:10.3390/chromatography2030422. URL https://doi.org/10.3390%2Fchromatography2030422.

[11] J. Park, A. Mittal, An improved model for the steric-entropic effect on the retention of rod-like particles in field-flow fractionation: Discussion of aspect ratio-based separation, Chromatography 2 (3) (2015) 472–487. doi:10.3390/chromatography2030472. URL https://doi.org/10.3390%2Fchromatography2030472.

[12] R. Beckett, J. Giddings, Entropic contribution to the retention of nonspher- ical particles in field-flow fractionation, J. Colloid Interface Sci. 186 (1) (1997) 53–59. doi:10.1006/jcis.1996.4612. URL https://doi.org/10.1006%2Fjcis.1996.4612.

[13] P. D. Cobb, J. E. Butler, Simulations of concentrated suspensions of rigid fibers: Relationship between short-time diffusivities and the long- time rotational diffusion, J. Chem. Phys. 123 (5) (2005) 054908. doi: 10.1063/1.1997149. URL https://doi.org/10.1063%2F1.1997149.

[14] J. Park, Dynamics of suspensions of rodlike polymers with hydrodynamic interactions, Ph.D. thesis, University of Florida (2009). URL https://search.proquest.com/docview/304876186.

[15] S. Monjezi, J. D. Jones, A. K. Nelson, J. Park, The effect of weak con- finement on the orientation of nanorods under shear flows, Nanomaterials 8 (3) (2018) 130. doi:10.3390/nano8030130. URL https://doi.org/10.3390%2Fnano8030130.

[16]   K. Asokan, T. R. Ramamohan, V. Kumaran, A novel approach to computing the orientation moments of spheroids in simple shear flow at arbitrary p´eclet number, Phys. Fluids 14 (1) (2002) 75–84. doi:10.1063/1.1426391. URL https://doi.org/10.1063%2F1.1426391.

[17]   S. B. Chen, D. L. Koch, Rheology of dilute suspensions of charged fibers, Phys. Fluids 8 (11) (1996) 2792–2807. doi:10.1063/1.869085. URL https://doi.org/10.1063%2F1.869085.

III. THE SHAPE EFFECT ON THE RETENTION BEHAVIORS OF ELLIPSOIDAL PARTICLES IN FIELD-FLOW[3]

Saman Monjezi[a], Mason Schneier[a], Jaeyeong Choi[b], Seungho Lee[b*], and Joontaek Park[a*]

[a] Missouri University of Science and Technology, Chemical and Biochemical

Engineering Department, N State St 1101, Rolla, MO, 65409, USA

[b] Hannam University, Chemistry Department, Daejeon 34054, Republic of Korea

[*] corresponding authors: E-mails: slee@hnu.kr (S.Lee) and parkjoon@mst.edu (J.Park)

ABSTRACT

A theoretical model is proposed to analyze the shape effect on the retention behaviors of rod-like particles in field-flow fractionation. This model is improved from a previous model by Park and Mittal [Chromatography (2015) 2: 472-487]: The model can predict the retention behaviors of the rods, of which shape is assumed as a prolate ellipsoid, with low and high aspect ratios in various flow conditions of the flow-field flow fractionation. The effects of rod aspect ratio on the retention behaviors of the rods with the same volume are investigated in each operation mode. In normal mode, the retention rate decreases with increasing aspect ratio. In steric-entropic mode, where we substantially improved the model to evaluate the rod orientation and the concentration distribution more rigorously based on our recent studies on the distributions of the rod orientation and concentration [Nanomaterials (2018) 8:130; Chem. Eng. Sci. (2018) 189:396-400], the retention ratio increases with the increasing aspect ratio. In steric

---

[3] This paper was submitted to *Chromatography A* journal, 2018

mode, the retention ratio decreases with increasing aspect ratio again. Those results are

discussed based on how the cross-sectional concentration distributions are affected by the

aspect ratio. The criteria for the prediction of each mode is also discussed. Comparison

with the experimental data shows the qualitative agreement.

1. INTRODUCTION

The importance of shape-based micro/nanoparticle separation techniques has

consistently increased because micro/nanoparticles with shape-specific physico-chemical

properties, such as metal nanorods [1, 2] and polystyrene nanorods for drug delivery [3],

have become prevalent in industry with many practical applications and can be also

found in nature [4]. However, studies and development for methods separating these

particles by shape are still relatively unexplored compared to those of typical size-based

particle separations. Shape-based particle separations have been considered as special

applications of corresponding size-based separation method [5]. Therefore, clear

understanding of the particle shape effect on the separation behaviors in a size-based

separation device is the basis for the development of shape-based separation theory and

method.

In this study, we propose a theoretical model to elucidate the shape effects of rod-

like particles on the elution behaviors in field-flow fractionation (FFF). FFF, one of the

most popular size-based particle separation techniques, is versatile and adaptable in its

design and operating conditions [6-8]. Therefore, its extension to shape-based particle

separation has gained interests. Furthermore, analysis of experimentally observed separation behaviors of non-spherical particles has required a theory for shape-based separation. It was observed that the separation of non-spherical particles using SdFFF (FFF using sedimentation as a cross force) resulted in the different elution behaviors from those of the spherical particles with the same volume [9]. There was an experiment where sphere-shaped bacteria were separated from rod-shaped bacteria using SdFFF. However, the separation seemed to be mainly caused by the size difference (the rod volume was 6 times larger than the sphere volume) [10]. The lengths of carbon nanotubes have been measured using FlFFF (FFF using a cross flow field) [11]. The effect of aspect ratio (Ar: the ratio of the rod length and the rod thickness) on the gold nanorod (GNR) elution behaviors in AsFlFFF (FlFFF with asymmetric flow field) has been studied but classic separation theory based on spherical particles cannot be used in explaining the experimental results [12-14].

The rod shape's effect on the separation behaviors in FlFFF has been theoretically studied in a series of works by Alfi and Park [15] and Park and Mittal [16]. These works were developed based on previous theoretical model by Beckett and Giddings [17] as well as a numerical simulation study by Phelan and Bauer [18]. Various separation principles in FFF (a.k.a operation modes) were discussed in terms of the rod dynamics and configurations distinguished from those of spherical particles. The "steric-entropic mode" has been especially focused as a possible separation mechanism for the experimentally observed Ar-dependent elution behaviors [13, 17]. However, only the qualitative explanation has been possible and further improvement of the theoretical model is required. The previous model by Park and Mittal is limited in that the valid Ar

range is high (>5) and the rod orientation distributions were roughly estimated. The

model in this study is improved so that it can be applied to the rods with low Ar ($1<Ar<5$)

and the rod orientation distributions can be evaluated rigorously based on the recent

studies on the rod configuration in channel flows [18, 19].

2. THEORY/CALCULATION

2.1. BASIC CONDITION

As demonstrated in Fig. 1, the FFF system for this study is assumed as a FlFFF

with the channel thickness of w, the average axial flow rate of $<v_x>$ ($< >$ indicates the

cross-sectional average), and the cross-flow rate of U_y. The axial flow, cross-sectional,

and vorticity directions are in x,y,z directions, respectively. The rod-like particles are

assumed as rigid prolate ellipsoid with the hydrodynamic rod length and thickness of $2a$

and $2b$, respectively. The unit vector, $\mathbf{p}$, describes the rod orientation. The angle between

the rod tip and the y-axis is defined as ψ. Hence, the y-component of $\mathbf{p}$, p_y, is equivalent

to $\cos\psi$. The restriction angle, ψ_1, defined as the angle when an ellipsoid, with its center-

of-mass position at y, touches the accumulation (bottom) wall, can be derived as:

$$\psi_1 = \arccos\left(\sqrt{\frac{y^2-b^2}{a^2-b^2}}\right) \tag{1}$$

It is assumed that the carrier liquid is a Newtonian, incompressible liquid in the

Stokes flow condition. The effect in the z-direction is neglected. It is also assumed that

the particle concentration is not high enough to consider the interaction among particles.

Since the separation principle of FFF is related to the interplay of the axial flow

field, the cross-force field and the particle diffusivity, the dynamic behaviors specific to

rods, distinguished from the dynamics of spherical particle, must be considered. Our model predicts the cross-sectional rod concentration profile, $c(y)$, which will be combined with the parabolic axial flow profile, $v_x(y)$,

$$v_x(y) = 6\langle v_x \rangle \frac{y}{w}\left(1 - \frac{y}{w}\right) \tag{2}$$

To get the retention ratio, R:

$$R = \frac{\langle c(y) \rangle \langle v_x \rangle}{\langle c(y) v_x(y) \rangle}, \tag{3}$$

which will be used for the elution order prediction.
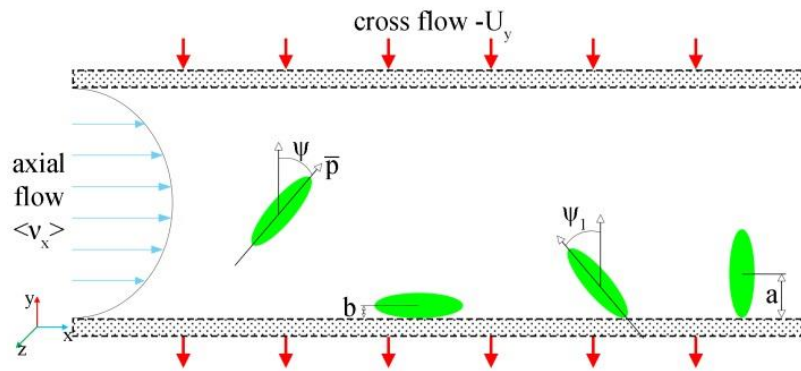
Figure 1. Schematic diagram for the ellipsoidal particles in FlFFF.

2.2. DIFFUSIVITY TERM CORRECTION

We start from modifying the model equation for $c(y)$ of rod-like particles, previously derived by Park and Mittal [16] assuming the rod as slender-body [17]. The modification of the model equation for ellipsoidal particles becomes:

$$c(y) = c_o exp\left[\int_b^y \frac{-U_y}{\langle\langle D_y(\bar{y})\rangle\rangle} d\bar{y}\right] S(y) \tag{4}$$

Here, c_o is typically set as a concentration at the accumulation wall. However, we define that as a normalization constant to make $c(y)$ in the form of a probability distribution

function (integrating $c(y)$ over $y=0$ to w gives 1). D_y is the diffusivity coefficient of a

prolate ellipsoid effective in the cross-sectional direction. Since the orientation of a rod

tumbles by shear of the axial flow and fluctuates by the Brownian rotation, the ensemble

average $<<D_y>>$ is required for the evaluation of $c(y)$. Additionally, due to the

inhomogeneous position-dependent local shear rate,

$$\dot{\gamma}(y) = \frac{6\langle v_x \rangle}{w}\left(1 - \frac{2y}{w}\right) \tag{5}$$

which is the derivative of $v_x(y)$ in terms of y, $<<D_y>>$ is also a function of the distance

from the accumulation wall and must be integrated from b to y. Note that y with the over

bar indicates the dummy variable for the integration in Eq (4) and $y=b$ is the closest

distance of the rod center-of-mass from the accumulation (bottom) wall [18] (see Fig 1).

Using the expression for the diffusivity tensor of an ellipsoid [22], the expression for

$<<D_y>>$ can be written:

$$\langle\langle D_y(y)\rangle\rangle = D_a\left(\frac{1}{Y^A} + \left[\frac{1}{X^A} - \frac{1}{Y^A}\right] \ll p_y{}^2(y) \gg\right), \text{where } D_a = \frac{k_B T}{6\pi\mu a} \tag{6}$$

Here, D_a is a diffusion coefficient equivalent to that of a sphere with its radius of a, k_B is

a Boltzmann constant, T is an absolute temperature of the system, μ is a dynamic

viscosity of the carrier liquid. X^A and Y^A are the coefficients in the diffusivity tensor

expression of an ellipsoid [22]. Details of the expressions are shown in Appendix A. The

ensemble average of the orientation moment, $<<p_y{}^2>>$, is determined by the flow

condition and the Brownian rotation. Therefore, it can be obtained as a function of Peclet

number, Pe, which is defined as a ratio of the shear rate and the rotational diffusivity

coefficient of a rod [23-25]. All the previous calculations of $<<p_y{}^2>>$ in terms of Pe are

for the rods in bulk flow. Therefore, $<<p_y{}^2>>$ of a rod in the near-wall region ($b<y<a$),

where the rod orientation is affected by the geometric restriction from a wall, has not

been available. However, very recently, more accurate calculation of the average

orientation moments considering the wall restriction was presented [19]. Therefore,

$<<p_y^2>>$ can be obtained as a function of the rod position as well. How to get $<<p_y^2>>$ in

terms of Pe and y is also summarized in Appendix A. In this work, local Peclet number,

$Pe(y)$, is defined as the ratio between the local shear rate of the axial flow and the

rotational diffusivity coefficient of an ellipsoidal particle, D_R, [22] for being used in the

analysis of the results.

$$Pe(y) = \frac{\dot{\gamma}(y)}{D_R}, \text{where } D_R = \frac{k_B T}{8\pi\mu a^3 Y^C} \tag{7}$$

The expression for Y^C, a coefficient for the rotational diffusivity expression, is also given

in Appendix A.

2.3. STERIC ENTROPIC CORRECTION

In Eq. (4), $S(y)$ is the steric entropic term, which considers the rod configuration

under a geometric restriction by a wall. In the original model by Beckett and Giddings,

that term was defined as the ratio between the restricted and unrestricted surface areas on

a sphere with a diameter of the rod length (see Fig. 2A) [17]. However, Park and Mittal

argued that the steric entropic term must be evaluated considering the change of the rod

orientation distribution due to the flow condition [16]. Based on the recent studies on the

rod configurations near a wall [19, 20, 26], as schematically demonstrated in Fig. 2B, the

rod orientation distribution becomes shallower along the axial flow direction with

increasing Pe. Furthermore, as seen in Fig. 2C, if Pe becomes much higher, the "pole-

vault" type rotation causes the rod to be expelled from the near-wall region [27].

However, the prediction of the rod orientation distribution by Park and Mittal was made

with a coarse approximation. That limitation was due to the lack of study on the effect of

the wall confinement on the rod distribution at that time. Although how the rod

orientation distribution is changed under various conditions has been studied by many

researchers [23, 24, 28], those were either only performed for the rods in a bulk flow

(unrestricted by wall) or not enough information or model equation to be used in further

applications [29]. It is important to note that the rod behavior at $Pe>100$ in FlFFF, shown

in Fig. 2C, is different from that in a typical channel flow without any cross flow. More

details will be discussed in the later section.
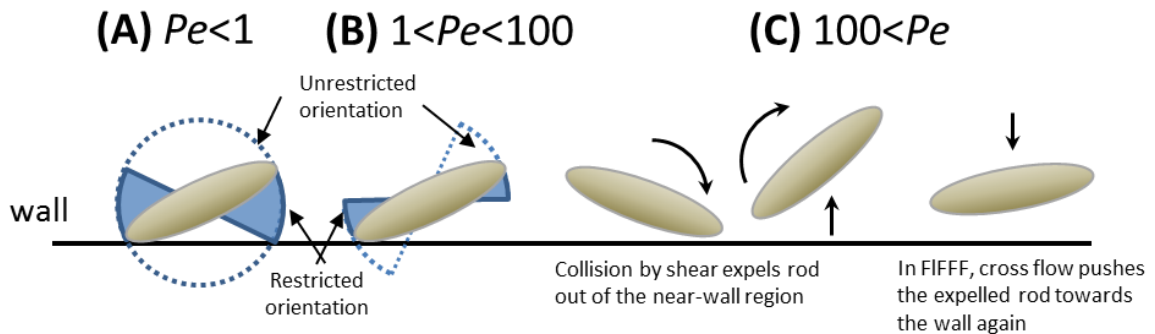
Figure 2. Schematic diagrams of how the rod orientations and rotations are sterically restricted by a wall to result in the change in the cross sectional distribution of a rod in each Pe region in FlFFF: (A) Pe<1, (B) 1<Pe<100, and (C) Pe>100. The mechanism in the right is different from that in channel flows without cross flow.

Recently, it was systemically presented the rod orientation distributions in terms

of various rod angles as a function of Pe and the wall confinement [19]. Moreover, this

work suggested an approximate expression for the rod orientation distribution as a

probability distribution function, $PDF(\psi;Pe)$, as a function of with a parameter of Pe, of

which expressions are also presented in Appendix A. More recently, it was also proposed

that $S(y)$ can be evaluated more rigorously using the mathematical expression for $PDF(\psi;Pe)$ [20]. $S(y)$ is decomposed into two new terms of $S_B(Pe,y)$ and $S_S(Pe,y)$ according to each rod-wall interaction mechanism:

$$S(y) = S_B(Pe,y)S_S(Pe,y) \tag{8}$$

Here, $S_S(Pe,y)$ is the steric factor due to shear contribution, which will be explained in the next paragraph. $S_B(Pe,y)$ is the steric factor due to Brownian contribution, which is equivalent to the original steric-entropic term at $Pe<1$. For $Pe>1$, $S_B(Pe,y)$ can be generalized using $PDF(\psi;Pe)$:

$$S_B(Pe,y) = \frac{\int_{\psi_1}^{0.5\pi} PDF(\Psi;Pe) \sin \Psi d\Psi}{\int_0^{0.5\pi} PDF(\Psi;Pe) \sin \Psi d\Psi} \tag{9}$$

Here, the numerator corresponds to the probability of the rod orientations restricted by the wall (recall that ψ_1 is the restriction angle defined in Eq. (1)) and the denominator indicates the probability of the unrestricted orientations. The $\sin\psi$ terms in the integrals are for performing the integration on a spherical surface. For $Pe<1$, PDF becomes a constant to recover the original steric-entropic term by Beckett and Giddings. As Pe increases larger than 1, PDF becomes concentrated near $\psi=0.5\pi$, as seen in Fig. 2 as well as in Fig. A2. This is because a rod is aligned along the axial flow direction with increased Pe. Consequently, the more aligned rod orientations are less restricted by the wall ($S_B(Pe,y)$ increases). However, it was identified that a new mechanism takes place at higher Pe [20].

As demonstrated in Fig. 2C, it was found that "pole-vault" rotation makes the center-of-mass position of a rod is lifted to $y=a$ [27]. Hence, this exclusion effect is incorporated into the evaluation of $S(y)$ using $S_S(Pe,y)$ in Eq (8). The concept for deriving

$S_S(Pe,y)$ is that a rod is expelled from the near-wall region, $y<a$, if the rod tumbling period is shorter than an average time when rod can stay in the near-wall region. The time that a rod can stay in the near-wall region can be defined as the "penetration time", τ_p, which it takes for a rod located at y to move out of the near-wall region by diffusion:

$$\tau_p = \frac{(a-y)^2}{2D_y} \tag{10}$$

Note that D_y here is approximated as

$$D_y \approx D_\perp = \frac{D_a}{Y_A} = \frac{4a^2 Y_C}{3Y_A} D_R \tag{11}$$

It was shown that this assumption is valid because this pole-vault motion happens more frequently in high Pe [20]. The rod tumbling period, which is also known as Jeffery orbit period, was found as:

$$T_J = \frac{2\pi(Ar + Ar^{-1})}{\dot{\gamma}} \tag{12}$$

Combining Eq. (10) through Eq. (12), $S_S(Pe,y)$ is made decrease to 0 at higher *Pe* (more rod is expelled):

$$S_s(Pe, y) = \frac{1}{1+\frac{\tau_p}{T_J}} = \frac{1}{1+\frac{3Y_A(a-y)^2 Pe}{16\pi Y_C a^2 (Ar+Ar^{-1})}} \tag{13}$$

Using the both $S_B(Pe,y)$ and $S_S(Pe,y)$, $S(y)$ can be evaluated for the entire ranges of *Pe*, which was validated for channel flows.

2.4. NUMERICAL CALCULATION

In this study, our model will be mainly used to investigate the effect of *Ar* on *R* for the rods with the same volume under a same flow condition. The chosen flow conditions will be described in each result. The rod geometries (*a* and *b*) of each *Ar* with

the same volume are calculated using an effective radius, r_{eff}, of the sphere with the equivalent volume:

$$a = r_{eff}Ar^{2/3} \text{ and } b = r_{eff}Ar^{-1/3} \text{ because } \frac{4}{3}\pi r_{eff}^3 = \frac{4}{3}\pi\frac{a^3}{Ar^2} \tag{14}$$

A Carrier liquid with properties of T=298K, μ=0.00106Pa.s, and density of ρ=1000kg/m^3 is chosen, considering a surfactant solution property [30]. The channel gap is chosen as w=350μm. For a given flow condition and the particle volume, Eq (4) is calculated along with Eq (5) through Eq (13) as described in the previous sections. The $c(y)$ obtained from Eq (4) is combined with Eq (2) to give the result of R.

Note here that we neglect the lift/hyper-layer term, which was derived by Alfi and Park [15] based on the shear-induced rod migration [25, 31, 32], in Eq (4). This study focuses on the steric-entropic effect which is much advanced than the previous models by Beckett and Giddings as well as Park and Mittal. Additionally, based on the numerical study by Park and Butler [32], the migration effect only becomes distinguishable at a very high Pe (>1000) condition, which occurs with particles that are larger than a microscale, and at a higher axial velocity than is typically acceptable for FFF flow conditions, so long as the proper excluded volume mechanism is considered as in this study.

3. RESULTS AND DISCUSSION

This is a sentence to take up space. This is a sentence to take up space. This is a sentence to take up space. This is a sentence to take up space. This is a sentence to take up space. This is a sentence to take up space. This is a sentence to take up space.

3.1. THE RETENTION BEHAVIOR IN NORMAL MODE

Our model is used to investigate the effect of *Ar* of the rods with a same volume on *R*. We chose three different volumes corresponding to r_{eff}=100, 200 and 300 nm. The flow condition is chosen as U_y=0.1μm/s and $<v_x>$=0.002m/s for the best demonstration of the trend. The results are shown in Fig 3.

Figure 3. Model prediction of R as a function of Ar for the rods with different volumes equivalent to those of the spheres of reff=100, 200, and 300nm. The flow condition is chosen as Uy=0.1μm/s and <vx>=0.002m/s.

For the rods with the same *Ar*, as the particle volume increases, *R* is reduced, which coincides with the normal mode trend of spherical particles. For each volume, *R* decreases (slower elution) as *Ar* increases (*Ar*-delayed elution trend). These trends have already been found for the rods with *Ar*>5 by the previous model based on slender-body

rods [16]. In the chosen condition in Fig 3, most of the results are within the normal

mode region based on the criteria suggested by Beckett and Giddings ($D_\perp/U_y > a$). The

values of $<<D_y>>$ scale asymptotically as $\sim Ar^{-2/3}\ln(2Ar)$, further approximated to $\sim Ar^{-0.3}$

by fitting. Therefore, as the rods have higher Ar for a same volume, $<<D_y>>$ gets smaller.

This result confirms that the trend in normal mode is not changed for low Ar of $1<Ar<5$.

Also, it is worth note that all the retention values at $Ar=1$ match the theoretical retention

ratio calculation considering the steric effect, derived by Giddings.

Figure 4. Normalized c(y) as a function of y/w for the rods of Ar=1.5, 7.0 and 20. Those
rods have the same volume equivalent to those of a sphere with reff=300nm.

To understand the effect of Ar on R in more detail, how the cross-sectional

concentration distribution is affected by the change of Ar was investigated. Fig 4

compared the $c(y)$ resulting from the calculation of Eq (4) for the rods r_{eff}=300nm and

Ar=1.5, 7.0, and 20 under the same flow condition as in Fig 3, $c(y)$. All the $c(b<y<a)$ in the near wall region has an increasing trend towards the maximum at $y=a$ (a/w= 0.00112, 0.00314 and 0.00632 for Ar=1.5, 7.0. and 20 respectively), which is due to the steric-entropic correction described in Section 2.3. All the $c(a<y<w)$ in the bulk decays towards the upper wall, as in the typical concentration distribution of FFF. Comparing the $c(y)$ of each Ar, more particles near the wall, $c(b<y<a)$, are pushed away from the wall with higher Ar but the particles in the bulk, $c(y> 0.02w)$, show the opposite trend: As Ar increases, more particles in the bulk are pushed towards the wall due to the increased $<<D_y>>$. As a result, the overall particles with higher Ar are distributed closer towards the wall. Consequently, the reduced R with increased Ar is predicted in the normal mode.

3.2. THE RETENTION BEHAVIORS IN STERIC-ENTROPIC MODE AS WELL AS STERIC MODE

We extended the study of the effect of Ar of the rods with a same volume on R to the particle with larger volumes to investigate the retention behaviors beyond the normal mode, especially the steric-entropic mode, where the rod orientation sterically restricted by the wall affects the concentration distribution. We performed the same model calculation for r_{eff}=500nm and 1000nm under the same flow condition as in Fig 3. The results are shown in Fig 5.

For the rods with r_{eff}=500nm, the Ar-delayed elution trend was found at 1<Ar<6 while the Ar-enhanced elution trend (R increases with higher Ar) emerged at Ar>6. For the rods with r_{eff}=1000nm, the Ar-enhanced elution trend was found for 1<Ar<13 and the Ar-delayed elution trend happened again for Ar>13. As observed in the experimental work by Gigault et al. [13], the Ar-enhanced trend can be predicted using this model. In

this condition, the rods with a same $Ar>6$ do not show the trend of the reduced R with increased volume as in Fig 3. In other words, the shape or Ar effect becomes more dominant on R in this condition than the size effect does in the normal mode.

In terms of the mode region criteria, suggested by Beckett and Giddings, the steric-entropic mode range ($a>D_{\perp}/U_y>b$) corresponds to $Ar>10$ for $r_{eff}=500$nm and $Ar>2.1$ for $r_{eff}=1000$nm. If we try a different range such as $b> D_{\perp}/U_y >a$, the steric-entropic modes of each rod are predicted as $Ar>4.5$ for $r_{eff}=500$nm and $Ar>1.6$ for $r_{eff}=1000$nm. It is not surprising because neither $D_{\perp}$ or D_a but a value somewhere between those two diffusivities, considering the average orientation, are actually involved in the particle diffusion opposite to the cross flow, as mentioned in Section 2. Therefore, $Ar>6$ for $r_{eff}=500$nm and $Ar>1.5$ $r_{eff}=1000$nm seem to be reasonable enough. Therefore, we suggest to use $(D_a+D_{\perp})/2U_y$ for predicting the operation mode of rods. Also confirm that this suggested criterion is applicable to the normal mode.

We first investigate the Ar-enhanced elution trend by comparing the $c(y)$ of the rods with $r_{eff}=1000$ nm and $Ar=1.5$ and 7.0. As shown in Fig 6, the particles distributions in the near-wall region, $c(b<y<a)$, are pushed further away from the wall for higher Ar, due to the steric-entropic effect and the broader near-wall region for higher Ar rod ($a/w=0.00374$ and 0.0104 for $Ar=1.5$ and 7.0 respectively). However, in contrast to the normal mode in Fig 4, fewer particles are distributed in the bulk region, $c(y>0.02w)$, for higher Ar rod, where the steric-entropic mode is dominant. Consequently, more particles are lifted away from the wall for higher Ar rods to result in the increased R.
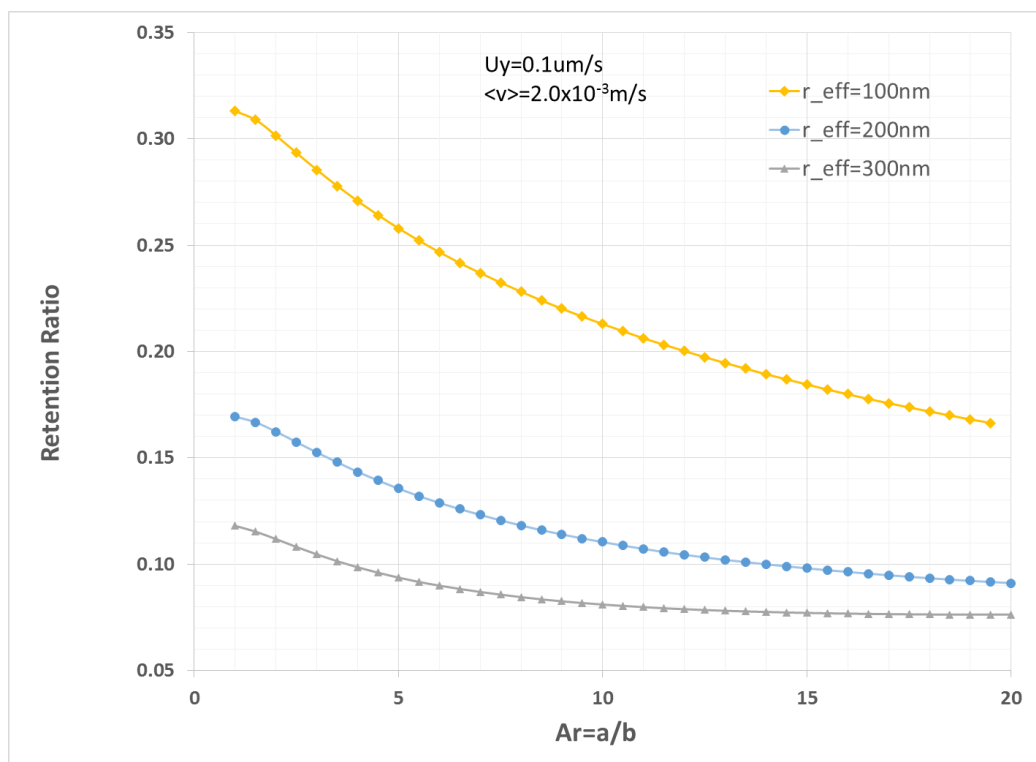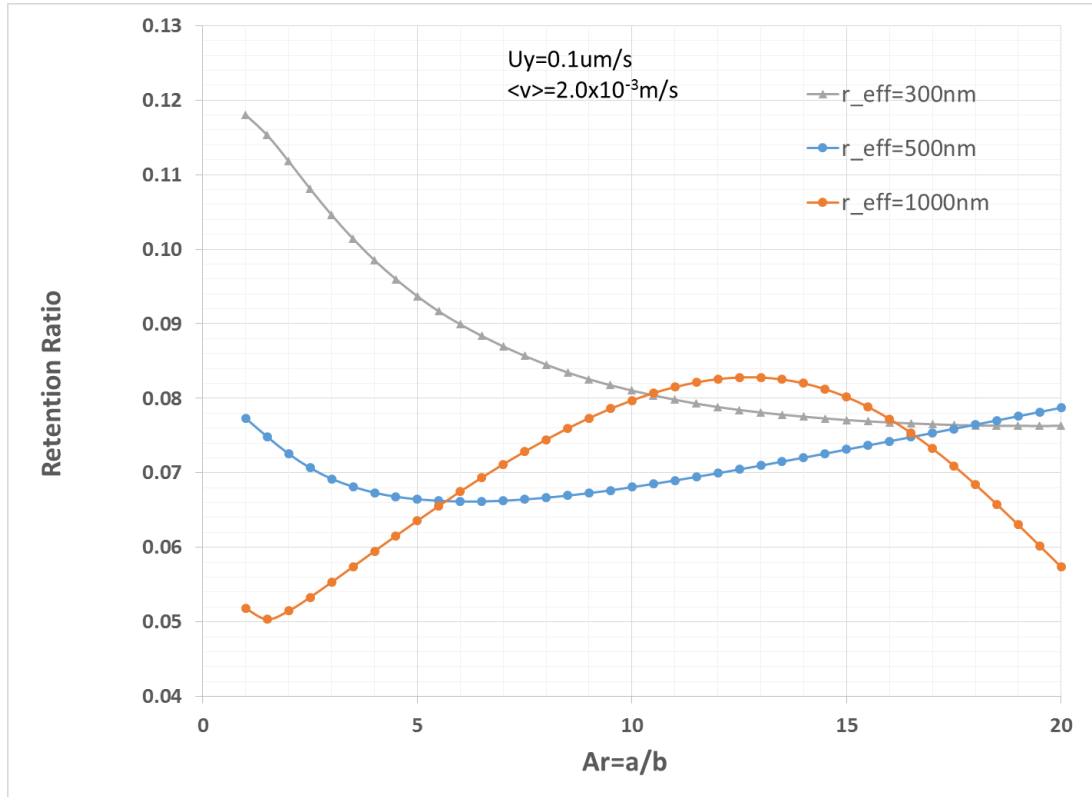
Figure 5. Model prediction of R as a function of Ar for the rods with different volumes equivalent to those of the spheres of reff=300, 500, and 1000nm. The flow condition is chosen as Uy=0.1μm/s and <vx>=0.002m/s.

Secondly, we also investigated the *Ar*-delayed elution trend by comparing the $c(y)$ of the rods with r_{eff}=1000 nm and *Ar*=16 and 20. As shown in Fig 7, the value of $c(y=a)$ is no longer maximum but a shoulder peak. The maximum values of $c(y)$ are found near $y>b$. These trends can be explained by the rod-wall interaction mechanisms depicted in Fig 2c. The second maximum at $y=a$ (a/w=0.0181 and 0.0210 for *Ar*=16 and 20 respectively) is due to the rods expelled by the pole-vault motion. However, as $<<D_y>>$ decreases with higher *Ar*, U_y becomes relatively stronger to result in the transition of the steric-entropic mode into the steric mode. This also explains why the second maximum becomes smaller for higher *Ar*. Consequently, most of the rods expelled to $y=a$ are

pushed down to the wall again by U_y. In this mechanism, the rods move down to a

position where those average orientations (mostly aligned along the axial flow direction

in this condition) are allowed as demonstrated in Fig 2b. Since more particles are pushed

down towards the wall for higher *Ar*, the *Ar*-delayed elution trend happens at the higher

Ar with the larger particle volume. It is interesting to note that the second maximum peak

was not detected for the distribution in a channel flow [20]. The unique condition of the

cross flow in FFF causes the second maximum, which is expected to give a more

dispersed elution peak. More studies such as Brownian dynamics simulation are planned

to confirm the results from the model prediction.
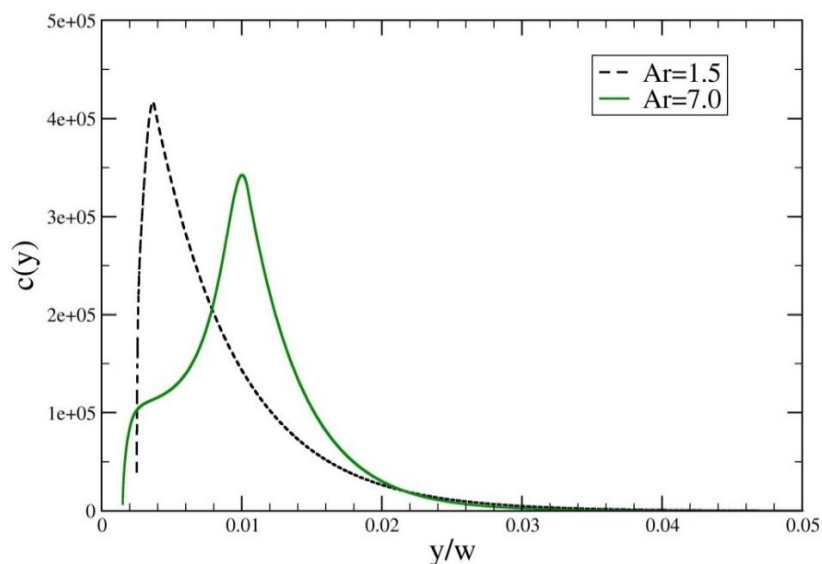
Figure 6. Normalized c(y) as a function of y/w for the rods of Ar=1.5 and 7.0. Those rods
have the same volume equivalent to those of a sphere with reff=1000nm.
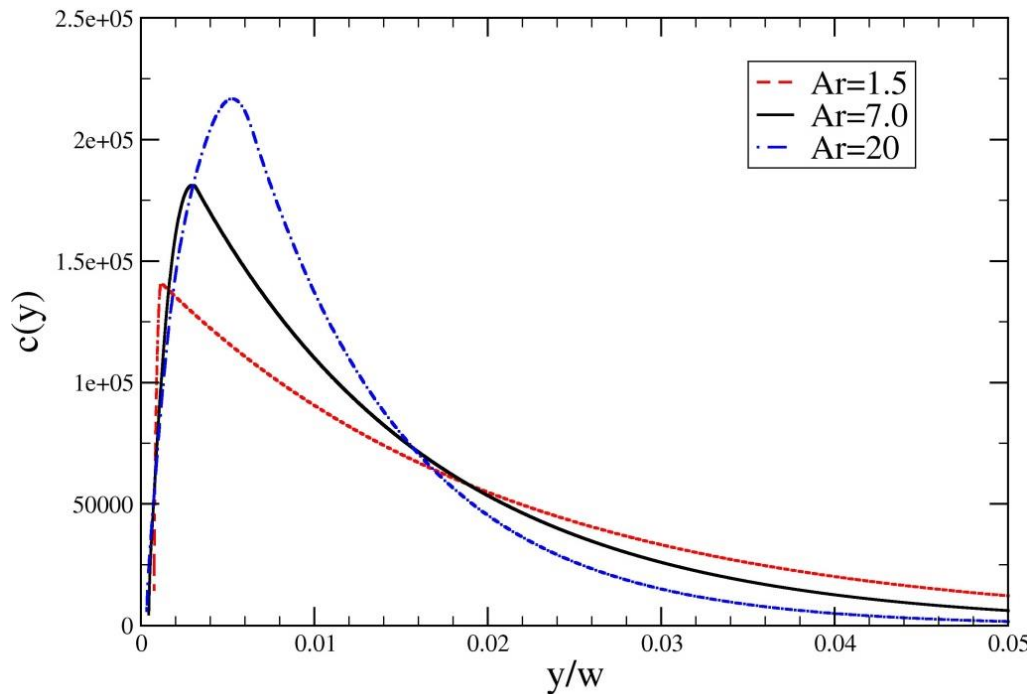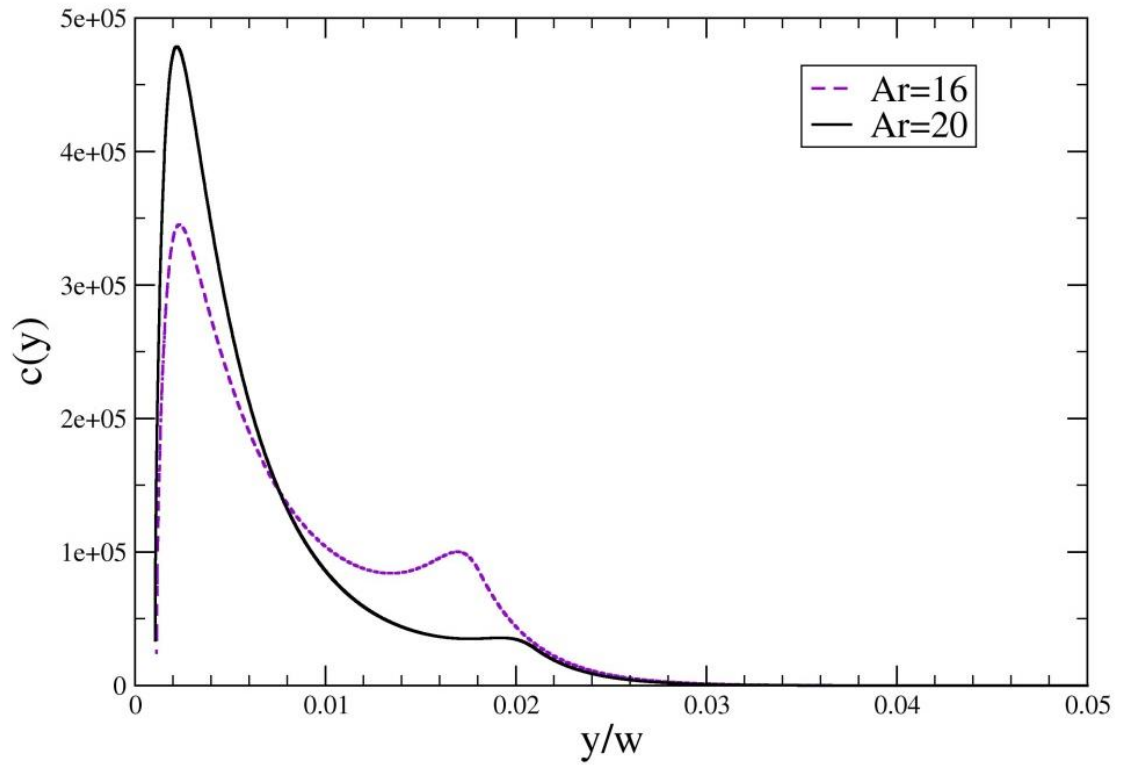
Figure 7. Normalized c(y) as a function of y/w for the rods of Ar=16 and 20. Those rods have the same volume equivalent to those of a sphere with reff=1000nm.

In terms of the mode region criteria, suggested by Beckett and Giddings, the steric mode range ($b>U_y/D_\perp$) corresponds to $Ar>>20$ for $r_{eff}=1000nm$. For the different range we tried in the steric-entropic mode, $b>U_y/D_a$, the steric-entropic mode is predicted as $Ar>8.6$ $r_{eff}=1000nm$. The reason for this discrepancy is attributed to the difference in the mechanism. The typical steric mode is where all the particles are rolling on the accumulation wall, but in this condition some rods are bouncing as in Fig 2c. However, as in the steric-entropic mode, it is a good estimation somewhere between the range predicted by ($b> D_\perp/U_y$) and ($b> D_a/U_y$). Therefore, we propose a criteria to predict the operating modes for rods using $(D_\perp+ D_a)/2U_y$.

3.3. COMPARISON WITH THE EXPERIMENTAL DATA

Ar-dependent elution trend was reported by Gigault and coworkers [13]. Regardless of the particle volume size, the elution order is dependent on the *Ar*. This trend was identified as feasible in our model prediction in Fig 6. However, the particle sizes are different. Still we cannot quantitatively match at this particle size. Our model was derived based on the rod orientation under a geometric restriction by a wall. This disagreement with the experimental data leads to a conjecture the particle surface charge effect must be considered in the shape effect on the retention behaviors.

Runyon and coworkers reported the separation results of various geometries of GNR using AsFlFFF [12]. We applied our model to one of their data sets to discuss the size and the *Ar* effects on the elution order. Since the experimental data is only presented in terms of the elution time, t_R, we had to convert the data to $R=t_o/t_R$ using the void time, $t_o=3$min, reported in that paper. Particle geometries were used with the dry particle sizes added 12nm considering a surfactant layer covering the particle. The experimental data set named as "G5" is plotted as a function of *Ar* in Fig. 8. For the model prediction results, not only the particular R value at a corresponding *Ar* of each particle, a range of R for the same volume within the range 1.1<*Ar*<10.6 are calculated. This is to distinguish the size effect and the *Ar* effect on R. For those particles with around *Ar*=2, the model predicts the R values pretty well. There is a discrepancy between the experimental value and the model prediction for *Ar*=1.77. Considering the agreement of other particles, that particular discrepancy is conjectured to be simple measurement error or an error in the choice of t_o. Additionally, the estimated experimental R values are too large (typically recommended R values are 0.02~0.1). Considering the differences in R for the particle

with similar *Ar* values, we can say that the size effect is more sensitive to *R* in this low *Ar*

and normal mode condition. It is also noticeable that *R* of the particle with high *Ar*=9.17

is well predicted by the model. Therefore, we confirm that the particle shape effect is

more obvious when the *Ar* difference is more than an order of magnitude. This is due to

the weak *Ar* dependence discussed in the previous section (~$Ar^{-0.3}$).
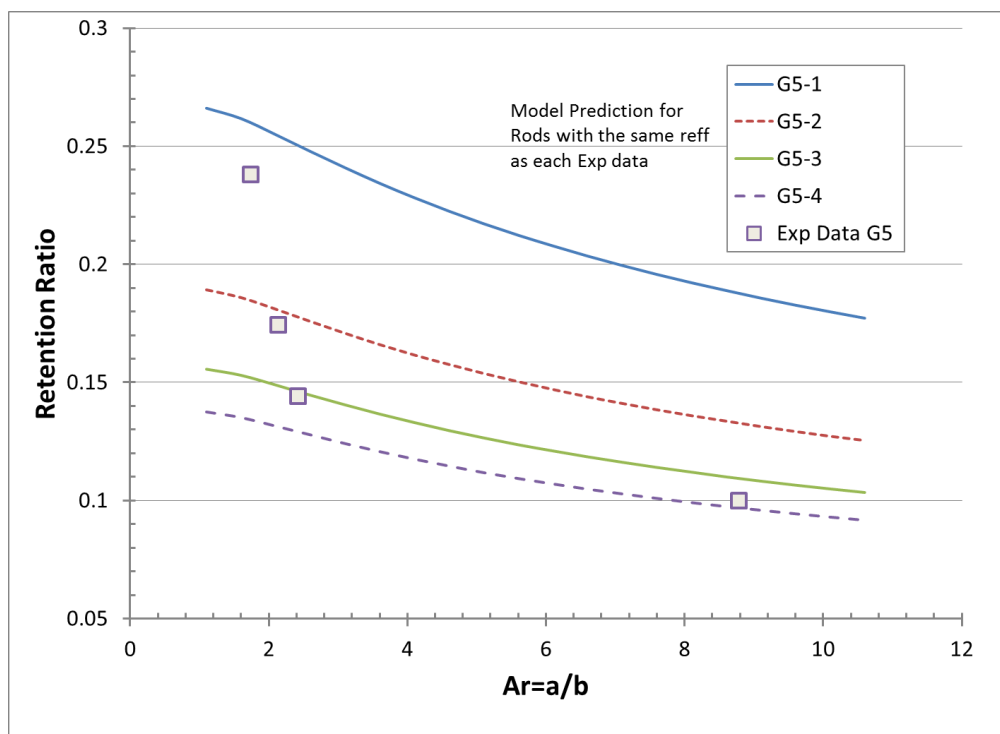
Figure 8. Comparison of the R vs Ar values from experiments by Runyon et al. (2012) and our model prediction. Experimental data are in symbols. Each line indicates the R vs Ar for each reff of particles.

Ar-dependent elution trend was reported by Gigault and coworkers [13].

Regardless of the particle volume size, the elution order is dependent on the *Ar*. This

trend was identified as feasible in our model prediction in Fig 5. However, the particle

sizes must be set differently. Still, we cannot quantitatively match at this particle size.

Our model was derived based on the rod orientation under a geometric restriction by a wall. This disagreement with the experimental data leads to a conjecture the particle surface charge effect must be considered in the shape effect on the retention behaviors.

4. CONCLUSIONS

We developed a theoretical model to predict the retention behaviors of rod-like particle in FFF. This model is improved from the previous model by Park and Mittal [16]: extended to the low Ar rods and incorporated rigorous evaluation of the rod orientation in wider ranges of flow conditions. The investigation on the effect of Ar on R for the rods with a same volume showed that the Ar-delayed elution trend was detected in normal mode, of which suggested range is $a<(D_a+D_\perp)/2U_y$. The Ar-enhanced elution trend is possible for a certain condition of the steric-entropic mode, where $b<(D_a+D_\perp)/2U_y<a$. The Ar-delayed trend is also possible for the steric mode, where $(D_a+D_\perp)/2U_y<b$. Comparing with the available experimental data, the normal mode trend is well matched. The Ar-enhanced elution trend is possible for qualitative matters, but a quantitative agreement requires more study. Surface charge effect and the actual flow field in the AsFlFFF must be considered for further development. Considering the recent experimental verification of the steric-entropic mode for disk-like particles [33], extension of this model to disk-like particle is also planned for future.

Conflict of interests

The authors have declared no conflict of interests.

ACKNOWLEDGEMENT

APPENDIX: DETAILS OF MATHEMATICAL EXPRESSIONS

Based on the diffusivity expression derived for a prolate ellipsoidal particle [22], the terms in Eq. (6) and Eq. (7) are

$$X^A = \frac{8}{3}e^3 \left[-2e + (1 + e^2) \ln \left(\frac{1+e}{1-e} \right) \right]^{-1} \tag{A.1}$$

$$Y^A = \frac{16}{3}e^3 \left[2e + (3e^2 - 1) \ln \left(\frac{1+e}{1-e} \right) \right]^{-1} \tag{A.2}$$

$$Y^C = \frac{4}{3}e^3(2 - e^2) \left[-2e + (1 + e^2) \ln \left(\frac{1+e}{1-e} \right) \right]^{-1} \tag{A.3}$$

$$\text{where } e = \frac{\sqrt{a^2 - b^2}}{b} \tag{A.4}$$

The average orientation moment, $<<p_y^2>>$, was calculated as a function of y and Pe by Monjezi et al. [19] and shown in Fig. A1. As the rod approaches the wall (y decreases), all the moment values vanish to 0. The calculation of the moment can be done in either the interpolation of the data in Fig A1, deriving an approximate fitting function, or using $PDF(\psi;Pe)$:

$$\langle\langle p_y^2 \rangle\rangle (Pe, y) = \frac{\int_{\Psi_1}^{0.5\pi} \cos^2 \Psi PDF(\Psi;Pe) \sin \Psi d\Psi}{\int_0^{0.5\pi} PDF(\Psi;Pe) \sin \Psi d\Psi} \tag{A.5}$$

$PDF(\psi;Pe)$ were also calculated by Monjezi et al. [19] and shown in Fig A2. It

was found that it can be expressed in the following form [20]:

$$PDF(\Psi; Pe) = \frac{a_1(Pe)a_2(Pe)+a_3(Pe)\left|\Psi-\frac{\pi}{2}\right|^{-4}}{a_2(Pe)+\left|\Psi-\frac{\pi}{2}\right|^{-4}} \tag{A.6}$$
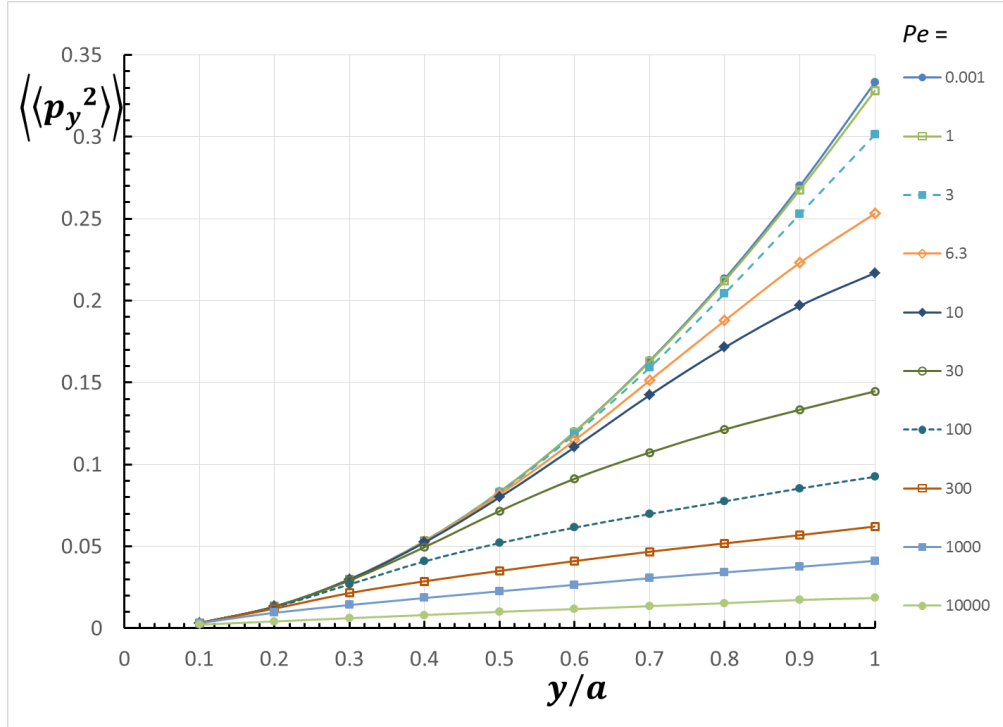
Figure A.1. <<py2>> as a function of y with various Pe, calculated by Brownian
dynamics simulation [19, 25].

This function is defined in $0<\psi<\pi/2$. Here, $a_i(Pe)$ indicates the parameter, which is a

function of Pe. The following is the expression for a_1:

$$\log_{10} a_1(Pe) = -0.498 + \frac{-0.9524[\log_{10} Pe+10]^{54.53}}{10.75^{54.53}+[\log_{10} Pe+10]^{54.53}} \tag{A.7}$$

The next expression holds for a_2 and a_3:

$$\log_{10} a_i(Pe) = f_i - 1 + \frac{g_i[\log_{10} Pe+10]+h_i-f_i}{1+exp\left[-31\left\{\log_{10} Pe+10+\frac{h_i-f_i}{g_i}\right\}\right]} \tag{A.8}$$

Note that the parameters, f_i, g_i, and h_i, corresponding to a_i are obtained from regression methods and listed in Table 1.

Table A.1. Parameters for Eq. (A.8) corresponding to a_i.

	(i=2) a_2	(i=3) a_3
f_i	0.7006	0.5169
g_i	1.342	0.3325
h_i	-13.27	-2.912
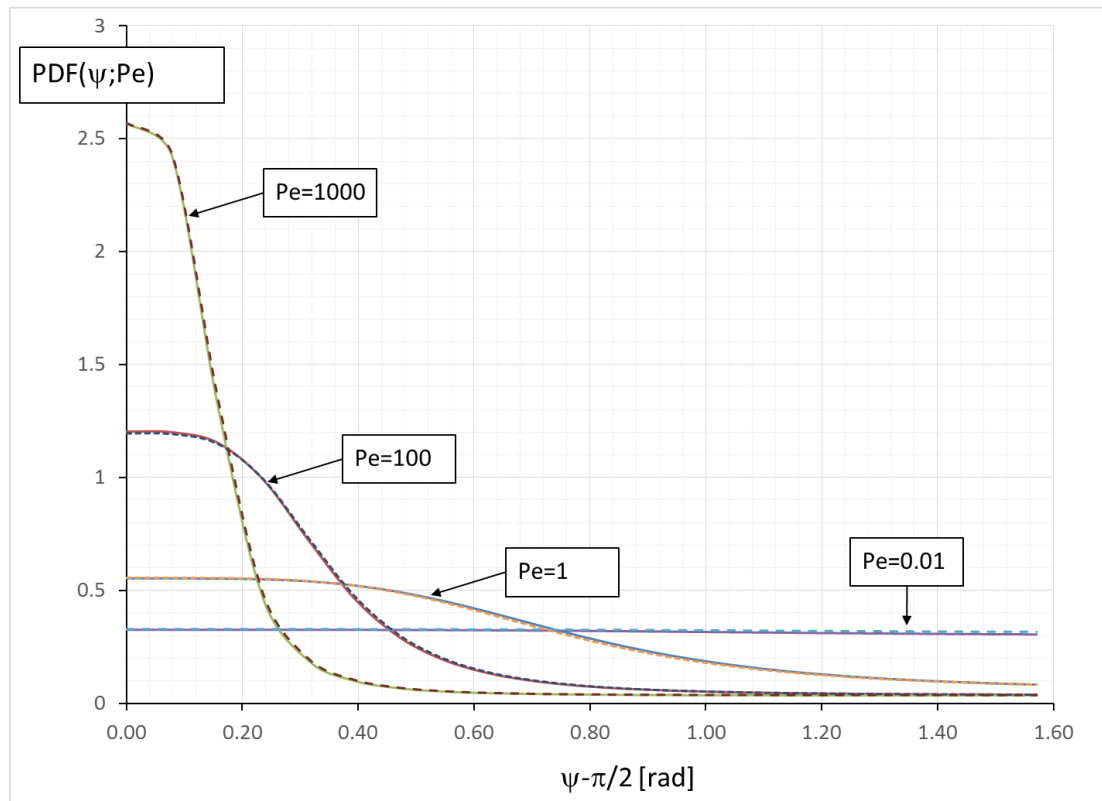
Figure A.2. PDF(ψ;Pe): Solid lines represent PDF obtained from Brownian dynamics simulation [19, 25]. Dotted lines indicate the approximate function, Eq. (A.6). The distribution is symmetric with the vertical axis at ψ-π/2=0. Each curve is normalized. For the integration on a sphere surface, $\sin\psi$ must be multiplied.

REFERENCES

[1]   V. Sharma, K. Park, M. Srinivasarao, Colloidal dispersion of gold nanorods: Historical background, optical properties, seed-mediated synthesis, shape separation and self-assembly, Mat. Sci. Eng. R, 65 1-38 (2009).

[2]   N.E. Hjerrild, R.A. Taylor, Boosting solar energy conversion with nanofluids. Phys. Today 70 40-45 (2017).

[3]   S. Barua, S. Mitragotri, Synergistic targeting of cell membrane, cytoplasm, and nucleus of cancercells using rod-shaped nanoparticles. ACS Nano 7 9558-9570 (2013).

[4]   Lenshof, A., and Laurell, T., "Continuous separation of cells and particles in microfluidicsystems", Chem. Soc. Rev., 39 (2010) 1203-1217.

[5]   B. Kowalczyk, I. Lagzi, B.A. Grzybowski, Nanoseparations: Strategies for size and/or shape selective purification of nanoparticles, Curr. Opin. Colloid Interface Sci. 16 135–148 (2011).

[6]   M.E. Schimpf, K. Caldwell, J.C. Giddings, Field-Flow Fractionation Handbook, John Wiley & Sons (2000).

[7]   F.A. Messauda, R. D. Sandersona, J. R. Runyon, T. Ottec, H. Pasch, S. K. R. Williams, An overview on field-flow fractionation techniques and their applications in the separation and characterization of polymers, Prog. Poly. Sci. 34 351-368 (2009).

[8]   K.-G. Wahlund, Flow field-flow fractionation: critical overview, J. Chromatogr. A 1287 391 97–112 (2013).

[9]   M.H. Moon, Miscellaneous particles □1□m in diameter, in: M. Schimpf, K. Caldwell, J.C. Giddings (Eds.), Field-Flow Fractionation Handbook, Wiley-Interscience, New York, pp383-395 (2000).

[10]   R. Sharma, R. Beckett, Biological particles of environmental interest, in: M. Schimpf, K. Caldwell, J.C. Giddings (Eds.), Field-Flow Fractionation Handbook, Wiley-Interscience, New York, pp537-560 (2000).

[11]   Chun, J., Fagan, J.A. , Hobbie, E.K., Bauer, B.J., "Size Separation of Single-Wall Carbon Nanotubes by Flow-Field Flow Fractionation" Anal. Chem. 80 2514-2523 (2008).

[12]   Runyon, J. R., Goering, A., Yong, K., Williams, S. K. R., "Preparation of Narrow Dispersity Gold Nanorods by Asymmetrical Flow Field-Flow Fractionation and Investigation of Surface Plasmon Resonance" Anal. Chem. 85: 940-948 (2013).

[13]   Gigault, J., Cho, T.J., MacCuspie, R.I., Hackely, V.A., "Gold nanorod separation and characterization by asymmetric-flow field flow fractionation with UV–Vis detection" Anal. Bioanal. Chem. 405: 1191-1202 (2013).

[14]   Nguyen, T.M., J. Liu, V. A. Hackley, "Fractionation and Characterization of High Aspect Ratio Gold Nanorods Using Asymmetric-Flow Field Flow Fractionation and Single Particle Inductively Coupled Plasma Mass Spectrometry" Chromatography 2: 422-435 (2015).

[15]   Alfi, M., and Park, J., "Theoretical analysis of the local orientation effect and the lift-hyperlayer mode of rod-like particles in field-flow fractionation", J. Sep. Sci. 37: 876–883 (2014).

[16]   Park, J. and Mittal, A., "An improved model for the steric entropic mode for separation of rod like particle in field flow fractionation", Chromatography, 2: 472-487 (2015).

[17]   Beckett, R., Giddings, J.C.,"Entropic contribution to the retention of nonspherical particles in field-flow fractionation", J. Colloid Interface Sci. 186: 53-59 (1997).

[18]   Phelan Jr., F. R. and Bauer, B.J., "Comparison of steric effects in the modeling of spheres and rod-like particles in field-flow fractionation" Chem Eng Sci, 64, 1747-1758 (2009).

[19]   S. Monjezi, J.D. Jones, A.K. Nelson, and Joontaek Park, "The effect of weak confinement on the orientation of nanorods under shear flows", Nanomaterials, 8 (3): 130 (2018).

[20]   S. Monjezi, G. K. Patterson, A. K. Nelson, and Joontaek Park, "A model for the depletion layer prediction in a dilute suspension of rigid rod-like particles under shear flows in the entire range of Peclet numbers", Chem. Eng. Sci. 189, 394-400 (2018).

[21]   Batchelor, G. K. "Slender-body theory for particles of arbitrary cross-section in Stokes flow". J. Fluid Mech., 44, 419-440 (19700.

[22]   Kim, S. and Karrila, S. J., Microhydrodynamics, Elsevier, New York (1991).

[23]   Asokan, K, Ramamohan, T.R., Kumaran, V. "A novel approach to computing the orientation moments of spheroids in simple shear flow at arbitrary Peclet number", Phys. Fluid, 14: 75-84 427 (2002).

[24]   Chen, S.B.; Jiang, L. Orientation distribution in a dilute suspension of fibers subject to simple shear flow. Phys. Fluids, 11, 2878-2890 (1999).

[25]   Park, J., "Dynamics of Suspensions of Rod-like Polymers with hydrodynamic interactions", PhD Thesis, University of Florida, Gainesville, FL (2009).

[26]   J. J. de Pablo, H. C. Ottinger, and Y. Rabin, AIChE J. 38, 273 (1992).

[27]   Stover, C.A., Cohen, C. The motion of rodlike particles in the pressure-driven flow between two flat plates. Rheol. Acta, 29, 192-203 (1990).

[28]   Stover, C.A., Koch, D.L., Cohen, C. Observations of fibre orientation in simple shear flow of semi-dilute suspensions. J. Fluid Mech., 238, 277-296 (1992).

[29]   Hijazi, and A. Khater, A. Simulations of distribution functions for rod-like macromolecules in linear flow near solid surfaces. Comput. Mater. Sci, 20, 213-227 (2001).

[30]   Woo, I.S., Jung, E.S., Lee, S. "Retention behavior of microparticles in gravitational field-flow fractionation (GrFFF): Effect of ionic strength" Talanta132 945–953 (2015).

[31]   Park, J., Bricker, J. M. and Butler, J. M., "Cross-stream migration in dilute solutions of rigid polymers undergoing rectilinear flow near a wall", Phys. Rev. E, 76(4): 040801 (2007).

[32]   Park, J., and Butler, J. E., "Inhomogeneous distribution of a rigid fibre undergoing rectilinear flow between parallel walls at high Peclet numbers", J. Fluid Mech., 630: 267-298 (2009).

[33]   Tadjiki, S.,and Beckett, R., "Experimental verification of the steric-entropic mode of retention in centrifugal field-flow fractionation using illite clay plates", J. Chromtgr. A 1538, 60-66 (2018).

IV. COMPUTATIONAL STUDIES OF DNA SEPARATIONS IN MICRO-FABRICATED DEVICES: REVIEW OF GENERAL APPROACHES AND RECENT APPLICATIONS

Saman Monjezi, Behrouz Behdani, Meyyammai B. Palaniappan, James D. Jones,

Joontaek Park[*]

Department of Chemical and Biochemical Engineering, Missouri University of Science

and Technology, Rolla, Missouri, USA

Email: [*]parkjoon@mst.edu

ABSTRACT

DNA separation techniques utilizing micro-fabricated structures have been studied and improved because of their uses in applications such as gene analysis and manipulation. Computational study has played a pivotal role in this development by identifying separation mechanisms and by finding optimal designs for efficient separation conditions. The simulation of DNA separation methods in micro-fabricated devices requires the correct capture of the dynamics and the structure of a single polymer molecule influenced by flow, or electric, field in complex geometries. In this work, we summarize the polymer models and the methods, focusing on Brownian dynamics simulation, used to calculate inhomogeneous fields with consideration to complex boundaries. We also review the applications of these simulation approaches in various separation methods and devices: gel electrophoresis, post arrays, capillary electrophoresis, microchannel flows, entropic traps, nanopores, and rotational flows.

Keywords: DNA separation, single polymer dynamics, Brownian dynamics simulation, microfluidics, electrophoresis, entropic trap, microchannel

1. INTRODUCTION

Gene analysis is one of the essential tasks for advances in biotechnology. Gene analysis would not be possible without DNA manipulation techniques. With the advent of lab-on-a chip technology in the early 2000s, manipulation of DNA molecules in micro-fabricated microfluidic devices began to flourish [1-3]. The manipulation of DNA using these devices led to further research about the properties and the dynamics of DNA in micro or nano-scale geometries [4-6]. Among the DNA manipulation techniques, DNA separation is a crucial step in gene analysis, such as genome mapping and sequencing [7]. It has also been used in other applications such as DNA sorting, diagnosis and fingerprinting [8].

The mobility of DNA molecules is an important transport property in DNA separation techniques. DNA molecules tend to have similar mobility in free solution independent of their size because overall charge to mass ratio does not change much with molecular weight. This leads to difficulties in separating longer molecules [9, 10]. It has been found however that size-dependent flow behaviors are possible in a flow system where DNA molecules interact with complex geometries. Examples of this include the porous structure in gel electrophoresis and microscale flows with inhomogeneous force (or flow) fields [11, 12]. Indeed, microfluidic devices have become increasingly attractive in the field of DNA separation due to their ability to operate rapidly with only a small volume of sample [11]. However, it is expensive and time consuming to optimize the geometry of the device through new fabrications and numerous runs [13], or slab gel modifications in the case of gel electrophoresis [14]. Hence, several theoretical models have been developed to estimate overall mobility and diffusion coefficients [15-17].

However, computer simulations can give details of DNA trajectory and structure, rather than simplified ensemble average properties. Therefore, computational simulation of DNA dynamics in microscale flows have contributed to the development of experimental separation techniques and in identifying separation mechanisms [13, 18]. We review the computational simulation approaches for DNA dynamics, specifically the size-based separation of double stranded DNA, in microscale flows in this study.

As mentioned earlier, for DNA separation to be feasible, size-dependent dynamics or mobility must be caused by interaction with solid boundaries in the flow system. Therefore, single polymer dynamics and inhomogeneous force field calculations must be calculated simultaneously and self-consistently [19]. Through these combined simulations, separation mechanisms can be identified. This approach can be applied to other recent studies of DNA in confinements [2], such as DNA within nanochannels [5]. It can also be applied to flowing colloidal systems, such as drug delivery particles in the bloodstream [20].

2. SINGLE POLYMER DYNAMICS

The time and length scales for DNA separations are typically in similar or larger ranges of a single DNA molecule in a free space (length scales of $10 - 100$ μm and relaxation times of $0.01 - 1$ s). These scales are also larger than the base-pair molecular level so molecular dynamic simulation is not suitable. Indeed, the sequence of base-pairs does not affect the physical properties of DNA. Additionally, DNA separations are usually performed in a dilute concentration of DNA solution, which leads to an assumption that interaction with other DNA molecules can be neglected in modeling. In

those situations, Brownian dynamics (BD) simulation of a coarse-grained single polymer model is used for DNA separation simulation [21-23]. One of the advantages of utilizing coarse grained models is reduced complexity. This allows for model properties to be calculated quickly while maintaining sufficient accuracy for molecular properties. However, the polymer model must be carefully chosen to minimize the loss of polymer physics details required to describe the separation behaviors in interest [21-24,43,44]. In this section, we summarize the polymer models and corresponding BD simulation methods used in DNA separation simulations by focusing on the commonly used bead-spring model and briefly mentioning other models. Note here that we excluded Monte-Carlo (MC) approaches, which were used in earlier times [25, 26] or in recent studies on DNA structure in nano-scale confinements [5, 27].

2.1. BEAD-SPRING MODEL

The most common polymer model for DNA separation is the "bead-spring" model. Each "bead" represents a sub-chain larger than a Kuhn length, b_k (a shortest polymer segment length which is not bent or stretched by thermal fluctuation. DNA has $b_k\sim0.1$ nm which is much larger than that of typical polymer), and the "springs" lie between these beads. These springs are used to maintain the conformational entropy inside a sub-chain (represented by the beads). This is shown in Figure 1(a) [28, 29]. This model is a basic model used for many other polymer systems, such as entangled polymeric liquids [30], or networks [31]. The number of beads, N, (or the number of springs, N-1) must be carefully chosen so that computational time and the details of dynamics are balanced.
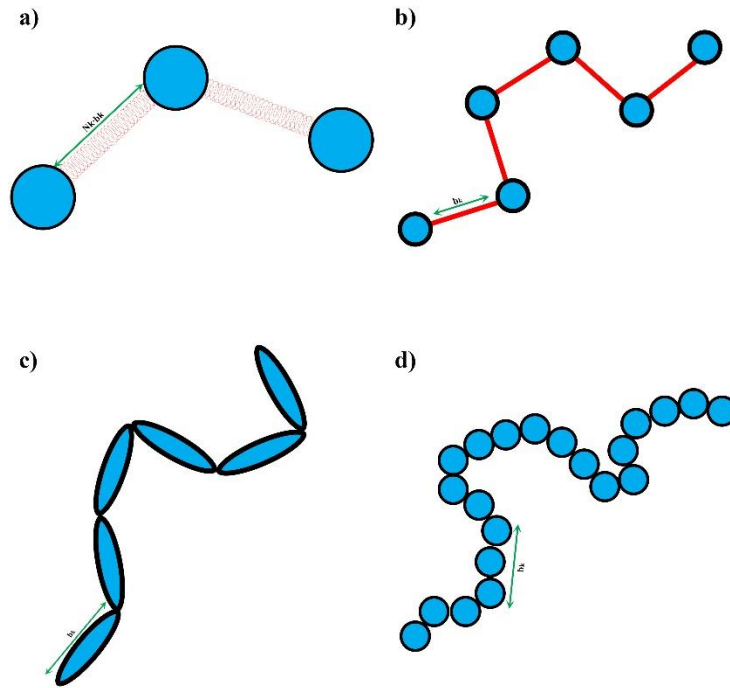
Figure 1. Schematic demonstration of the polymer models: Example of a DNA molecule with 6 Kuhn segments and its representations by (a) bead-spring model, (b) bead-rod model, (c) slender-body model, and (d) touching-bead model. The number of Kuhn segments per each spring is Nk.

The force balance on the i-th bead in a bead-spring chain model is given by Equation (1):

$$m_i \frac{d^2 r_i}{dt^2} = F_i - \zeta \frac{dr_i}{dt} \tag{1}$$

Here, m is the mass of the bead, r_i is the position vector of the bead, t is the time, F is the total net hydrodynamic force acting on the bead, and ζ is the drag coefficient. Stokes flow condition is usually applicable to microscale flows, hence, to DNA separations, too. When using Stokes flow condition, inertial effect is considered negligible (overdamping system). Thus, the left hand side of Equation (1) can be assumed to be 0. Electric fields are used in gel electrophoresis, a common method of DNA separation. Thus, along with

considering flow field, electric field (non-hydrodynamic force) is also evaluated to give

an equation of motion:

$$\frac{d\boldsymbol{r}_i}{dt} = \boldsymbol{U}(\boldsymbol{r}_i) + \mu\boldsymbol{E}(\boldsymbol{r}_i) + \frac{1}{\zeta}\left[\boldsymbol{F}_i^B(t) + \boldsymbol{F}_i^S(t) + \boldsymbol{F}_i^{EB}(t) + \boldsymbol{F}_i^{EW}(t)\right] \tag{2}$$

Here, $\boldsymbol{U}(\boldsymbol{r}_i)$ is the unperturbed fluid velocity at the bead position, μ is the electrophoretic

mobility, $\boldsymbol{E}(\boldsymbol{r}_i)$ is the electric force at the bead position, $\boldsymbol{F}_i^B$ is the Brownian force, $\boldsymbol{F}_i^S$ is

the net spring force, $\boldsymbol{F}_i^{EB}$ is the net excluded volume force between the other beads, $\boldsymbol{F}_i^{EW}$

is the excluded volume force with a wall (solid boundary). In many DNA separation

studies only one field is applied, either the electric or flow field. Therefore, either $\boldsymbol{U}(\boldsymbol{r}_i)$ or

$\boldsymbol{E}(\boldsymbol{r}_i)$ becomes 0. The evaluation of $\boldsymbol{U}(\boldsymbol{r}_i)$ or $\boldsymbol{E}(\boldsymbol{r}_i)$ with consideration to the micro-

fabricated structure of the device is one of the most important parts in DNA separation

simulations. This is discussed further in Section 3. The drag coefficient, ζ, is related to

the bead diffusivity, D_i. For typical electrophoresis conditions, DNA, which is a

negatively charged molecule, is always surrounded by counter ions. This cancels the

hydrodynamic interactions (HI) in strong ionic concentration [32-34]. Therefore, the

diffusivity can be regarded as a free-draining (not affected by other particles) property,

based on the Stokes-Einstein law:

$$D_i = \frac{k_B T}{\zeta} = \frac{k_B T}{6\pi\eta a} \tag{3}$$

Here, k_B is the Boltzmann constant, T is the absolute temperature, η is the solvent

viscosity, and a is the bead radius. The bead radius, a, is typically chosen to match the

experimental diffusivity data [21, 23]. Including HIs requires the use of a different tensor

form instead of the scalar coefficient. This will be discussed later in this section.

The Brownian force for a free-draining bead is evaluated at each time step from the fluctuation dissipation theorem, which must satisfy the following conditions:

$$\langle \boldsymbol{F}_i^B(t) \rangle = 0 \tag{4}$$

$$\langle \boldsymbol{F}_i^B(t) \boldsymbol{F}_j^B(t') \rangle = 2k_B T \zeta \delta(t - t') \boldsymbol{I} = \frac{2k_B T \zeta}{\Delta t} \boldsymbol{I} \tag{5}$$

Here, $<...>$ is the ensemble average. $\delta(t\text{-}t')$ is a delta function, which is non-zero at $t=t'$. $\boldsymbol{I}$ is the identity tensor. The actual expression to evaluate Brownian force used in simulation is:

$$\boldsymbol{F}_i^B(t) = \sqrt{\frac{2k_B T \zeta}{\Delta t}} \boldsymbol{w} \tag{6}$$

Here, $\boldsymbol{w}$ is a random vector, of which average is 0 and variance is 1, evaluated by any random vector generator algorithm [21, 23]. The discretized time step size is Δt.

The net spring force is the sum of the spring forces between adjacent beads:

$$\boldsymbol{F}_i^S(t) = \boldsymbol{f}_{i,i+1}^S + \boldsymbol{f}_{i,i-1}^S \tag{7}$$

Here, the sub-index $i,i+1$ represents the force between the i-th and the $i+1$ th beads. For the beads at both ends ($i=1$ and $i=N$), only one of these spring forces exists. There are various models used to describe the spring force, which is closely related to polymer conformation. The simplest spring force model is the Gaussian chain model also known as the Hookean spring model [24]. Streek et al. used this basic model for their simulations of DNA separation [21, 35, 36]. A disadvantage of this model is that the spring can violate its maximum stretch length, l. To overcome this problem, the finite extensibility nonlinear elastic chain (FENE) spring model is also used in some simulations [37, 38] or an additional constraint force is added [39]. However, for an

accurate simulation of polymer finite extensibility and stiffness, the use of Worm-Like

Chain (WLC) model was proposed [40, 41]:

$$\boldsymbol{f}^S_{i,i-1} = \frac{k_B T}{2 b_k} \left[\left(1 - \frac{|r_{i-1} - r_i|}{l} \right)^{-2} - 1 + 4 \frac{|r_{i-1} - r_i|}{l} \right] \frac{r_{i-1} - r_i}{|r_{i-1} - r_i|} \qquad (8)$$

Note here that the persistence length for WLC model is the half length of b_k.

Underhill and Doyle examined the nonlinearity of the extension-force relation further to

propose a correction method by incorporating the "effective" persistence length [28]. The

WLC model has become one the most popular polymer models for DNA dynamics.

The excluded volume force is the sum of each excluded volume force between

each bead:

$$\boldsymbol{F}^{EB}_i(t) = \sum_{j=1 \ (i \neq j)}^{N} \boldsymbol{f}^{EB}_{i,j} \qquad (9)$$

Streek et al. used a force derived from a truncated Leonard-Jones potential

equation [21, 35, 36]. However, Jendrejack et al. proposed a model based on

experimental observation [42]:

$$\boldsymbol{f}^{EB}_{i,j} = \frac{9 k_B T}{2l} v^E \left(\frac{3}{4\sqrt{\pi}} \right)^3 \left(\frac{2l}{b_k} \right)^{9/2} exp \left[-\frac{9}{4} \left(\frac{2l}{b_k} \right) |r_j - r_i|^2 \right] (r_i - r_j) \quad (10)$$

Here, v^E is the excluded volume parameter. Equation (10) is derived from a Gaussian

excluded volume potential. This is softer than the truncated Leonard-Jones potential and

is used to prevent small time step sizes [43, 44]. The excluded force from a wall can be

evaluated from the same equation by replacing r_j with the nearest boundary position [45],

whereas Jendrejack et al. used its simplified form [43, 44].

Numerical integration of Equation (2) is required to get the new bead position at a

new time step $t+\Delta t$. An explicit Euler scheme requires a very small Δt to prevent

numerical instability attributed to new spring lengths exceeding l or new bead positions

overlapping the solid boundaries of the model. Although an implicit Euler scheme can be used to avoid spring overstretch, the new position must be solved using Newton-Raphson iterations. This also results in long computational times. Therefore, Jendrejack et al. devised a semi-implicit scheme where an implicit Euler scheme is applied only to the integration of the term related to the spring force and the rest of the terms are integrated by an explicit Euler scheme [41]. Kim and Dolye also adapted the semi-implicit scheme [45]. They included an additional "re-position" step to consider the bead-wall overlap for irregular boundaries based on Heyes and Melrose's algorithm [46].

As mentioned earlier, Equation (3) can be only used when HIs are neglected. This assumes that DNA undergoing gel electrophoresis is uniformly negatively charged and the Debye length is smaller than the persistence length of DNA. With these conditions, HIs are assumed to be screened due to counterion movement [32-34]. However, an experimental study [47] and later simulation studies including HIs claimed that the HI effects cannot be negligible, where the channel size is on a Debye length scale [48-50]. Due to these concerns, whether inclusion of HIs within DNA separation simulations is important or not has been a controversial topic.

Inclusion of HIs for the bead-spring model is described by Jendrejack et al. [41-44]. Diffusivity in Equation (3) must be evaluated in a tensor form, D, in order for HIs to be considered:

$$D = \frac{k_B T}{6\pi\eta a}(I + \Omega) \tag{11}$$

Here, Ω is the HI tensor. For HIs with beads to be evaluated, the Oseen-burger tensor or Rotne-Prager tensor is used [24, 51]. The latter is used to avoid situations when D becomes a non-positive definite tensor. Bead-wall HIs are numerically evaluated from

each grid point. The diffusivity tensor from Equation (11) is then used with Equation (2), which can be rewritten as:

$$\frac{d\boldsymbol{r}_i}{dt} = \boldsymbol{U}(\boldsymbol{r}_i) + \mu\boldsymbol{E}(\boldsymbol{r}_i) + \frac{1}{k_B T}\boldsymbol{D}\cdot\left[\boldsymbol{F}_i^S(t) + \boldsymbol{F}_i^{EB}(t) + \boldsymbol{F}_i^{EW}(t)\right] + \nabla\cdot\boldsymbol{D} + \sqrt{2}\boldsymbol{B}\cdot\boldsymbol{w} \quad (12)$$

Here, $\boldsymbol{B}$ is the decomposed tensor of $\boldsymbol{D}=\boldsymbol{B}\cdot\boldsymbol{B}^T$. Note that the last term is the Brownian displacement term considering HIs. The position gradient of $\boldsymbol{D}$ is a correction term for numerical integration that considers the change of $\boldsymbol{D}$ over a time step. Despite the importance of HIs, including HIs in the bead-spring model has limitations: (1) HIs are concentrated on each bead. (2) multi-body interaction is not included as much level as in Stokesian dynamics [19] (3) it is computationally expensive to evaluate these Equations (11) and (12) at each time step. To overcome these problems other approaches have been applied. These include slender-body model and other simulation methods, which will be presented in later sections.

2.2. OTHER POLYMER MODELS

While the bead – spring model is the most widely used model in DNA separation simulations, other polymer models can be applied to simulation of DNA. Below we discuss bead-rod model, slender-body model, and touching-bead model.

a) Bead-rod model: As shown in Figure 1(b), this model defines a polymer molecule as a chain of beads connected by rigid rods, instead of flexible springs as in the bead-spring model. The vectors which represent the orientation of connecting rods are not dependent on each other. Thus, this can be considered as a freely-jointed chain. The connecting rod length is set as b_k, which leads to a less coarse-grained model than when using the bead-spring model. Compared to when using the bead-spring model,

penetration between chains is not allowed. Constraint forces are assigned to maintain a constant rod length between beads and prevents an overstretch of the chain [5, 24]. With the bead-spring model, various spring force models and numerical scheme for the equation of motions were proposed to prevent the overstretch, as discussed in Section 2.1. In the absence of a stretching force and the presence of strong longitudinal stiffness in the polymers the freely-jointed chain model can describe the dynamic behavior of the chain well. These conditions correspond to an entropy-dominated situation [52]. On the other hand, this model is not suitable under strong deformation or confinement situations less than $4b_k$ because bending within the rods is neglected [52]. Therefore, this model was used to study DNA structures confined within nanochannels, of which channel size is larger than $4b_k$ [53]. Patel and Shaqfeh used this model for simulation of DNA flowing in post arrays, where a DNA molecule hooked on a post is highly stretched [18].

b) Slender-body model: As shown in Figure 1(c), a DNA chain is represented by a series of connected rods (slender-bodies). In contrast to the bead-rod model, which carries resistance on each bead, the slender body model includes continuous resistance over contour length. This is a better representation of a real DNA molecule. Additionally, based on the HIs included on the slender-body connectors, multibody HIs can be included, which is the similar level as in Stokesian dynamics simulations. Bead based models have difficulties with including these interactions [19, 54]. However, for this model to be the freely-jointed chain, as in the bead-rod model, additional correction forces must be added [54]. In later studies, this model was applied to the simulation of DNA flows in pressure driven flow. HI with walls was also included using a Green's function for a point source between two boundaries [55, 56]. This allowed for shear-

induced migration to be simulated. Even DNA fragments shorter than b_k can be simulated as single slender-bodies [57, 58]. Michelleti further modified this model by incorporating the bending energy between connecting rods to study linear and circular DNA chains in slit confinement structures [59].

Touching-bead model: As shown in Figure 1(d), all the beads in this model are connected to each other without any springs or connecting rods in between. The length between beads is set to $a < b_k$ and can allow for bending within the model. This aspect makes this model more accurate than the bead-rod model. This flexibility within b_k enables us to calculate rotational diffusivity more accurately [5]. However, a larger number of beads is required for this model compared to the bead-rod or bead-spring models. This causes an increase in the computational time needed to evaluate the model. If a is set too large ($a \approx b_k$), the actual effective persistence length becomes smaller than $0.5 b_k$, which results in inaccurate prediction of DNA stretch [5]. Tree et al. computed the relaxation times of bacteriophage λ –DNA in a high ionic strength buffer confined in a nanochannel using this model. They also proved that as channel size decreases, there is a significant drop in relaxation time. This is due to a major decline in chain extension fluctuation [27]. Muralidhar et al. tested the underlying assumption under this method. They showed that their predictions for the chain extension and confinement free energy in the system agree with the simulation data for adequately long chains [60]. Dai et al. predicted DNA diffusivity in slit confinement using MC simulations using this model. Simulated DNA diffusivities are validated by experimental data [61].

2.3. COMPARISON OF POLYMER MODELS

In summary, bead-spring models, more specifically WLC model, have been widely used in simulations of DNA separations due to their efficiency. However, too much coarse-graining, in other words not enough beads, may result in an inaccurate description of dynamics and crossing of polymer chains. The bead-rod model can prevent the overstretch issue and the slender-body model can include HI more accurately. However, connector rigidity can cause limitations in the length scale of confinement. The touching-bead model can simulate DNA properties on a more realistic scale, but at the cost of a high computational load. Therefore, this model is mainly used in the study of DNA structure in nano-confinement.

3. FIELD CALCULATION IN COMPLEX GEOMETRY

As explained earlier, DNA separation simulations require local flow or force values , as in $U(\boldsymbol{r}_i)$ and $E(\boldsymbol{r}_i)$ in Equations (2) and (12), for polymer motion in the flow or force field of the separation device. If the geometry of the separation device is simple, such as a straight microchannel, its force or flow values at each position can be solved analytically. However, advances in DNA separation methods utilize DNA flows in complex geometries which induce nonlinear force or flow fields. These must be solved numerically. Therefore, DNA separation simulations require a proper combination of DNA dynamics predictions and field calculations.

3.1. FINITE ELEMENT METHOD

The finite element method (FEM) is a numerical method for solving differential equation within a boundary. This method discretizes the domain of the problem into smaller sub-domains, called finite elements or meshes, as shown in Figure 2(a). The discretized form of the governing equation results in a system of equations. Approximate solutions of these equations are obtained at each node of each element. Once the unknowns are solved, the values at the positions of interest are evaluated by interpolation. FEM is especially useful for complex geometries. For example, if the domain can be divided into a series of rectangles, as with structured microchannels, the finite difference method can be used [21, 35, 36]. However, for a domain near a circular object, which can be easily discretized with fine triangular shaped elements, it is suitable to use FEM [62].

As mentioned earlier, FEM can be used for electric field calculations with DNA electrophoresis simulations. The electric field of potential is denoted by Φ. The governing Laplace equation, in the fluid domain, Ω, is shown below:

$$\nabla^2 \Phi = 0 \tag{13}$$

The boundary where the electric potential is explicitly applied, given as $\Phi = \Phi_{given}$, is $\partial \Omega_1$. The boundary condition on the insulating walls, where potential is not applied, is $\mathbf{n} \cdot \nabla \Phi = 0$. Here $\mathbf{n}$ is a normal vector pointing out of the fluid domain. The solutions of equation (13) along with the boundary conditions obtained by FEM are then used to evaluate $\mathbf{E}(\mathbf{r}_i) = -\nabla \Phi(\mathbf{r}_i)$. Figure 2 shows an example of a meshed fluid domain and the calculated electric field in a microfluidic device with entropic traps, arrays of microchannels with different sizes [12, 63]. This is then combined with BD simulations of DNA polymer models by being used in Equation (2) or (12). Kim and Doyle tested

this combination of FEM and BD simulations [45]. They used FEM to obtain the

inhomogeneous electrical field around a spherical obstacle. DNA movement and

deformation under the electric field around the obstacle was also simulated [62].
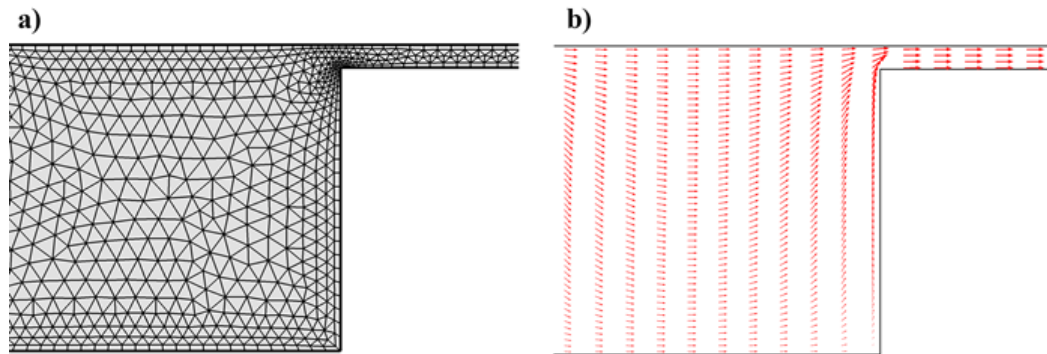
Figure 2. Example of electric field calculation by FEM for a microfluidic device with entropic traps: (a) Domain discretized with triangular mesh and (b) the calculated electric force vectors.

3.2. BOUNDARY ELEMENT METHOD

Boundary element method (BEM) is a numerical method used to solve "linear"

partial differential equation in a boundary. In this method, the fundamental solution of the

linear differential equation (Green's function) must be available first. Compared to FEM,

discretization is only required on boundaries, which results in fewer mesh points and

more efficient calculations. Instead of the interpolation used in FEM, the boundary

integral equation is used in BEM to evaluate flow or electric potential values at the

positions of interest. The surface integrals of the Green's function and its derivative are

utilized for this [13, 64]. The Laplace equation, Equation (13), and the Stokes equation

are linear differential equations and thus this method can be applied to solve

inhomogeneous electric fields [13, 64] and to consider HIs of DNA in microchannel

flows [43, 44]. HIs induced by DNA are difficult to calculate using FEM because DNA strands must be considered as moving boundaries. However, when using BEM, Green's functions for bead-bead interactions (Rotne-Prager solution [51]) or bead-wall interactions (Blake solution [65]) are adapted to consider the HI effects on DNA flow behaviors in microchannels. Jendrejack et al. studied the center-of-mass distribution of DNA in microchannel by evaluating Oseen-burger tensor or Rotne-Prager solution on each grid point on microchannel wall [43, 44]. Without incorporating these effects, the cross-sectional center-of-mass distribution of DNA is different from experimental observations. As explained after Equation (12), inclusion of HI is computationally expensive. However, Zhang et al. proposed more efficient and accurate method to simulate DNA flowing on nanopit arrays [66]. They combined the general-geometry Ewald-like method [67] with a variant of the immersed boundary method [68]. Additionally, instead of using Cholesky decomposition [69], Chebyshev polynomial approximation [70] was used to decompose $D=B \cdot B^{\mathrm{T}}$ much more efficiently. This method can be applied to complex geometries and hydrodynamic interaction is considered as much level as Stokeian dynamics simulation [19, 66].

3.3. LATTICE-BOLTZMANN METHOD

The lattice-Boltzmann Method (LBM) is a numerical method for the simulation of fluid using the discrete Boltzmann equation instead of conservative momentum balance equations like the Navier-Stokes equation [71, 72]. For small Knudsen and Mach numbers, the discrete Boltzmann equation becomes the Navier-Stokes equation. This method is known to be suitable for fluid flow calculations in complex geometries and

colloidal suspensions due to its basis in the Bhatnagar–Gross–Krook model [73]. This is a particle or fluid molecule collision model. For the LBM, a particle velocity distribution function describes the mass density and the velocity of a particle in a discretized lattice. The time evolution of this function is described by the discrete Boltzmann function and it can be converted to evaluate fluid hydrodynamic properties. LBM has been applied to the simulation of DNA dynamics in microfluidic devices by combining the flow field calculated from LBM with BD simulations of polymer chains. LBM can easily include the inertial and the HI effects in the simulation. However, electric field must be calculated explicitly. Therefore, if inertia and HIs are not important or there is no flow (only an electric field), FEM is more efficient. Additionally, LBM is more efficient if polymer concentration is higher [74, 75]. LBM was applied to the simulation of DNA in microchannel flows to show the cross sectional lateral migration of DNA induced by polymer-wall HI [71, 72]. LBM was also used in a study on the translocation of DNA through nanopores [76] and in the calculation of rotational flow fields for DNA separation simulations using streaming flow [77].

3.4. DISSIPATIVE PARTICLE DYNAMICS

As in LBM, mesoscale models can accurately represent the hydrodynamic properties of a flow system and they are not as expensive as atomic models in terms of computation load. Dissipative Particle Dynamics (DPD) is a simulation technique for fluid which utilizes the dynamic simulation of coarse – grained particles on a mesoscale. Mesoscale methods are intermediate methods between atomic scale and microscale [78-80]. Compared to molecular dynamic simulations, the atomic structure of the fluid and

solvent molecules is not considered. Clusters of molecules are defined as individual particles instead. Instead of using the particle velocity distribution function in a lattice used with LBM, fluid and polymer particle positions and velocities are calculated using stochastic differential equations with this method. Solid boundaries are simulated as a layer of "frozen" particles [78-80]. However, the soft potential causes large density fluctuation. Pan et al. adapted a double layer of frozen particles to remove this problem [50].

As in LBM, DPD is suitable for the calculation of flow fields in complex geometries including HIs. Another similarity is that electric force fields must be calculated explicitly. Additionally, the original DPD technique has a low Schmidt number, which is the ratio between kinematic viscosity to diffusivity. This causes slower momentum transfer when compared to mass transfer. This can be a major problem when simulating fluids within complex geometries [37]. Fan et al. proposed a possible solution to this problem. They modified the weight function in the dissipative force and decreased the cut off radius [81]. Litvinov proposed a modified DPD method called Smoothed DPD to study the static and dynamic behavior of DNA molecules in the flow. This method is based on second order discretization of Navier-Stokes equations and is good in better prediction of thermodynamic properties [82].

DPD was applied to DNA separation simulations in microfluidic devices that utilized electrophoresis and structured microchannels to examine the HI effects [50, 83]. Pan et al. found that a specific separation mechanism, corner trapping, that was identified by Streek et al. [35] was not identified while using DPD [50]. They claimed that the difference was due to the HI inclusion [49]. Ranjith investigated the effect of rotational

flow in microchannels on the transport and dynamics of DNA molecules. He utilized a modified DPD model called finite-size DPD which considers the size effects on the dynamic modeling of different particles. Rotational flow in the microchannel is also considered by adding a rotational dissipative force to the dynamics of the system [84].

3.5. COMPARISON OF MODELS

In summary, inhomogeneous electric field considering complex geometry can be calculated either by FEM or BEM. BEM is more efficient but there are many available popular commercial tools for FEM. If flow field considering complex geometry can be calculated by FEM, LBM [85], and DPD [80]. However, BEM can be used only for Stokes flow condition (negligible inertia). BEM, LBM, and DPD are used for the HI inclusion. Accurate and efficient method for including HI in BEM was developed by Zhang et al. [66]. LBM is also widely used but adaptation for irregular boundary is required [85]. DPD is also popular for its flexibility but modifications are required to prevent problems like low Schmidt number or large density fluctuation near a boundary [81]. There were studies comparing the methods for BD with HI as in Equations (11) - (12) and LBM [74, 75]. The agreements of both methods were confirmed. For the situation of highly stretched polymer conformation, small enough spatial and times step sizes are required [75].

4. SIMULATIONS OF DNA SEPARATIONS

In this section, we summarize the simulations of popular DNA separation methods.

4.1. GEL ELECTROPHORESIS

Gel electrophoresis is one of the most popular DNA separation tools. It is still widely used in many DNA related experiments [86]. A gel solution, usually made of agarose or polyacrylamide, is prepared. Once a gel is made from the gel solution, it is considered a porous media. Porous media is defined as a random array of obstacles with colloidal size. DNA samples are applied to the gel and an electric field is applied either in a constant or pulsed field. As mentioned earlier, long DNA molecules have similar electrophoretic mobility in free solution. However, interaction with the gel structure induces differences in mobility according to DNA length. After a certain period, the electric field is stopped and the band positions of the DNA sample are compared to those of a reference sample. A reference sample is a set of molecules with known lengths [14]. Various simulation studies elucidated the DNA-gel structure interaction mechanisms which cause the differences in DNA mobility within the gel.

Duke and Viovy adapted a MC simulation for studying DNA motion in gel electrophoresis [26]. They called the mechanism of the DNA motion as the "hopping rule". The gel structure was considered as a randomly connected 3D network of pores with uniform diameter. DNA motion was simulated as strands moving through the tube-like pores, like a snake, which is called as "reptation" [87]. Using this gel structure, they studied crossed-field electrophoresis, where the direction of the electric field is switched periodically. They studied how DNA responds to different electric fields in the gel structure. Their simulation found that the separation of relatively long DNA is positively affected when the angle between fields is elevated above 90 degrees.

Azuma and Takayama performed a BD simulation of DNA in a constant electric field gel electrophoresis. They modeled DNA as a bead-spring model and the gel structure as immobilized bars, simulated as lines of beads, in a 3D periodic box. They tracked the evolution of the radius of the longer principal axis and the velocity of the center-of-mass and found that those values show periodic behaviors in relatively strong fields. This was inferred as the "elongation-contraction" mechanism in DNA. The period of the elongation-contraction mechanism was also found to be proportional to DNA length. They used this finding to explain why long DNA strands cannot be separated under a constant electric field gel electrophoresis [39]. Streek performed BD simulation of bead-spring model to study the effect of pulsed electric field in gel electrophoresis [21].

4.2. ARRAYS OF POSTS

Although gel electrophoresis is a very common method, its limitations were described previously in this paper: time consuming procedures, inconsistency of random gel structure, and difficulty in the separation of relatively long DNA chains [14]. To overcome these limitations, microlithography techniques have been utilized and introduced to the development of micro-fabricated devices used in DNA separations [29, 88-90]. Instead of a random distribution of the colloidal size obstacles in the gel structure, the arrays and the sizes of the obstacles, or posts, can be fabricated as designed. Devices with post arrays have been used for the separation of relatively large molecules.

With advances in post array devices, simulation studies have been used to both identify separation mechanisms and to explore optimal array designs. Saville and Sevick

performed a BD simulation of a bead-spring model flowing around an obstacle [91]. This study identified two mechanisms: (1) "hooking" and (2) "roll-off", as shown in Figure 3. If a DNA molecule, moving under the influence of an electric field, hits a post, it may get hooked on the obstacle. In that case, the DNA conforms to a U-shape known as a hairpin. The DNA is likely to remain hooked on until it gets unhooked after some time. It has been found that hooking probability is proportional to chain length, therefore DNA molecule mobility is affected by its chain length [18]. However, if the size of a post is relatively larger than the DNA molecule, the molecule hits the obstacle and rolls around the obstacle with little change in conformation. This mechanism is independent of DNA size, and is not a desirable condition for separation [92].
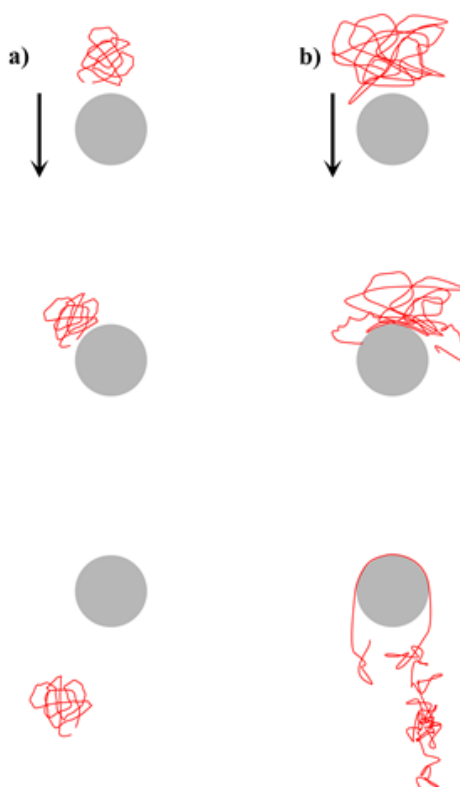
Figure 3. Schematic demonstration of (a) Roll-off and (b) Hooking mechanisms (Redrawn from [91]).
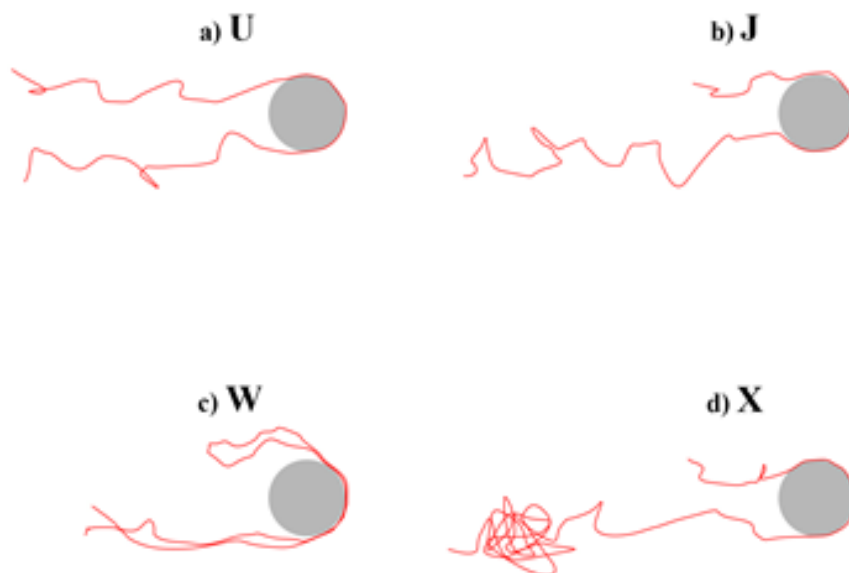
Figure 4. Various types of the hooking mechanisms (Redrawn from [62]).

Randall and Doyle incorporated an analytical expression for the inhomogeneous electric field around a circular object for more accurate DNA motion. They identified the trends of these mechanisms in terms of the radius of gyration of DNA, R_g, the size of the obstacle, and the electric field strength. For example, when the field is strong enough and the obstacle's diameter is small, the dominant mechanism is hooking [93]. They also further investigated the hooking mechanism in more detail. They identified four hooking modes: symmetric U-shaped hook, asymmetric J-shaped hook with constant extension, rare entangled W-hook, and asymmetric X-hook with increasing extension, as shown in Figure 4 [62, 93]. Previously, J-shaped hook, which is similar to a rope-on-pulley motion, was conjectured to be dominant. However, the simulation results validated experimental data that X-hook was the most dominant mode in hooking mechanisms. Kim and Doyle also extended the inhomogeneous electric field calculations for arbitrary objects using

FEM [45]. Later, it was shown that BEM is a more efficient method for electric field calculations [13, 64].

Studies on the effects of different array types have been performed systematically with the help of simulations. Patel and Shaqfeh investigated BD of a freely - jointed bead-rod chain in a sparse array of posts when they are ordered versus randomly dispersed. They concluded that disordered arrays in strong electric fields are optimal conditions for separation [18]. Later, calculations of inhomogeneous electric field values used with post arrays were performed by a commercial FEM solver for more accurate calculations [94]. BEM was also applied to electric field calculations in post arrays [13, 64]. Ou et al. also confirmed the importance of inhomogeneous electric field calculations. The results show a better prediction of mobility but underestimate diffusion coefficient values [95].

4.3. CAPILLARY ELECTROPHORESIS

Capillary electrophoresis (CE) separates macromolecules in a capillary when an electric field is applied to the system. CE needs less time to separate DNA and gives higher resolutions and sensitivities compared to typical gel electrophoresis. CE has mainly contributed to human genome analysis [1] and has taken over as the dominant separation method, especially for smaller DNA strands. CE also has the potential to become automated. The ends of the capillary tube are under a voltage and this creates an electrical field. The capillary is filled with a concentrated entangled polymer solution which substitutes the porous structure used in traditional gel electrophoresis. The DNA samples race through the capillary and their mobility is affected by their chain length, due

to polymeric conformation. As a result, the samples are separated by molecular size into different peaks each with a specific width that characterizes the CE performance [96].

Kekre et al. performed a BD simulation of DNA in CE [49]. While many studies assumed that HI is screened in the electrophoretic condition (high ionic strength limit) [48-50], there exists electrically induced hydrodynamic interaction between charged polymers [97] The simulation used the bead-spring model with the electrically induced HI. It was experimentally observed that DNA migrates across the electric field line and concentrates near the capillary wall if pressure gradient is applied in the opposite direction to the electric field [98]. Their simulation results agreed with the experimental phenomenon and found that DNA conformation is stretched by shear flow and that contributes to the migration towards the wall. Their finding suggests that the weak dependence of DNA mobility on length is mainly due to its average spherical conformation rather than the screened HI [46,47]. Pandey and Underhill recently developed a coarse-grained model for DNA in CE by considering internal DNA strand interactions [99].

4.4. STRAIGHT MICROCHANNEL

Studies on DNA dynamics in "straight" (this is different from the structured microchannel discussed in section 4.5) microchannel flows have been performed for basic understanding of DNA and solid boundary interactions. It is well known that if a pressure drop is applied to a Newtonian fluid between two parallel plates, a parabolic shape velocity distribution is created at steady state. Therefore, the velocities of DNA flowing in a microchannel are dependent on its cross-sectional position (faster elution for

DNA flowing near a center) and any factors affecting the cross-sectional DNA position can be a separation mechanism. Jendrejack et al. performed BD simulation considering DNA-wall HI [43, 44]. They showed that the DNA-wall HI resulted in shear-induced lateral migration of DNA: longer DNA has a tendency to migrate away from the wall, which results in faster elution. This migration has been shown by using slender-body models in different simulation methods [56, 58], and LBM [71, 72]. However, DPD requires adjustment of parameters for showing proper migration behaviors [37, 81]. There is a size-based particle separation technique, called field-flow fractionation. This technique applies an extra flow or force field in the cross-sectional direction while samples are flowing in the parabolic channel flow [100]. The applied field induces the cross-sectional position differences according to particle size. There were theoretical studies for applying this technique to DNA separation [101, 102].

4.5. STRUCTURED MICROCHANNEL ARRAYS FOR ENTROPIC TRAP

Periodically constricted channels were introduced as an effective way of creating entropic traps to separate DNA chains based on their length. The mechanism used in the entropic constriction of polymer molecules was first studied by Arvanitidou et al. [103]. It has been shown that long polymer chains are severely affected by entropic constriction when the size of the confinement is smaller than $2R_g$ of the polymer [12, 63].

As shown in Figure 2 and Figure 5, the device consists of both large and small periodic channels, which are fabricated using a lithographic method. The electric force is applied in the x-direction to move DNA through the channels. The height of the small channel, H_S, is designed to be smaller than $2R_g$ of DNA molecule. Therefore, DNA

molecule will be trapped in the larger channel until they manage to overcome the entropic barrier. However, the amount of free energy lost in this process is dependent on the length of the molecule. Consequently, the mobility of the DNA molecule is also length dependent. Surprisingly, it was shown that longer strands of DNA molecules elute faster. Initially, this was explained by Han et al. [12, 63]. For a DNA molecule to pass through the small channels of the device, it only takes a portion of the molecule to be close to the entrance and the rest of the molecule will be dragged into the channel accordingly. Longer molecules have more surface area and thus they have a higher probability of being dragged into the smaller channels. This causes these long molecules to exit the device faster than shorter DNAs [12, 63].
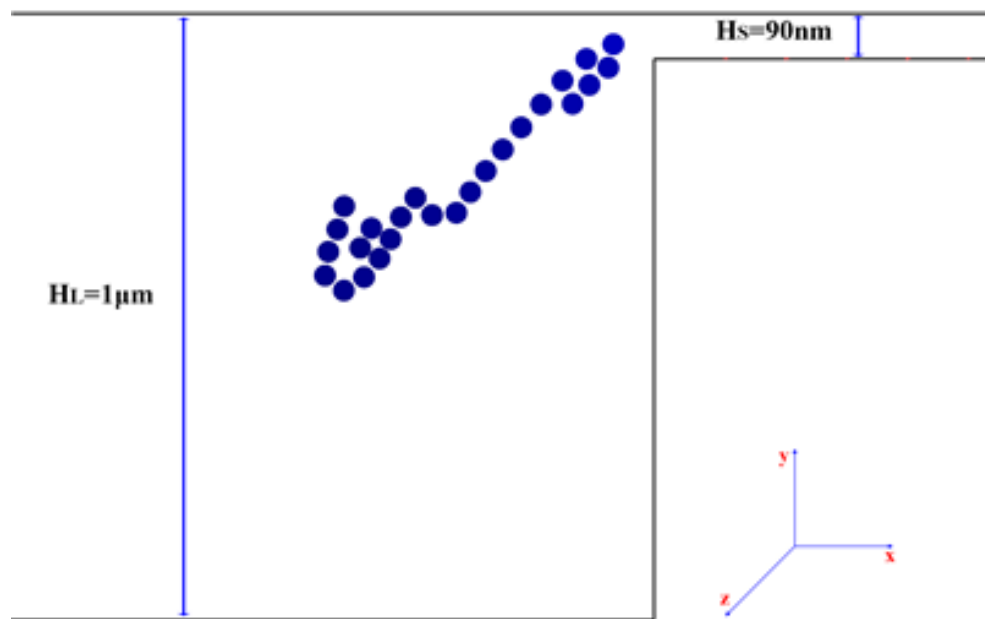
Figure 5. Schematic demonstration of the structured microchannel arrays for entropic trap and WLC flowing in that device: Total contour length of 52μm DNA is simulated as WLC of N=25. Its Rg is estimated as 65μm. Therefore, the smaller channel is an entropic barrier (2Rg > HS=90nm). Redarwn from [21].

The first attempt to simulate the device designed by Han et al. and to prove their theory was done by Tessier et al. [104]. They used a bound fluctuation MC method to simulate the behavior of long strands of DNA through the entropic trap device. The results of the simulation agreed with the experimental results by Han et al. The simulation could show the DNA conformation in the small channel region in detail. It was also found that the strength of the field directly affects deformation of the chain. When the field was weak, the initial energy needed to break the entropic barrier could not be obtained. In a strong field, the escape was rapid but the DNA did not have enough time to conform to the small channel.

Streek et al. performed BD simulation using the bead-spring model with a Hookean spring force. In this work, HI was ignored and the electric field was calculated using FDM [35]. The experimental results by Han et al. were accurately reproduced, although the authors claim that they found a new mechanism which dominated the mechanism, previously proposed by Han et al. The new mechanism was based on the diffusion coefficient of DNA. From the Einstein relation, we can say that smaller molecules have higher diffusion coefficients than larger molecules. Therefore, they are more likely to diffuse to the dead corners of the larger channel and spend more time there without being affected by the weak electrical field. Streek et al. also extended the study to the device with $H_s>2R_g$. The new mechanism was also detected in that device and the elution order was found to be similar (faster elution for longer DNA) at low electric field. However, the reverse elution order and non-equilibrium bistable behavior were found at high electric field [36].

Panwar and Kumar performed BD simulation with the bead-rod model [105]. They investigated the effects of DNA length and field strength on time scales in three distinctive regions: (1) placing the chain near the small channel, (2) breaking the entropic barrier, and (3) transporting the molecules through the small channel. Later, Lee and Joo performed a similar BD simulation to compare the motions of linear and star-branched polyelectrolyte molecules through an entropic array [106]. Their findings showed that the mobility of star branched molecules was significantly lower than linear polymers with the same molecular weight.

In earlier works, HIs were neglected in simulations of DNA separation by electrophoresis. The decision to neglect these interactions was based on the assumption that HIs are screened if the Debye length of the DNA is smaller than the scale of the device confinements. Therefore, this is a questionable assumption in the small channels. Application of DPD to the entropic trap simulation enables to investigate the HI effects. Moeendarbary et al. found that larger molecules have higher probability of hernia (kink) formation entering the smaller channel. These chain dynamics contribute to the higher mobility of longer DNA chains [49]. Pan et al. found that applying small voltages to the device resulted in a longer time required for separation. Higher voltages gave a quick but less efficient separation. They also found that the corner trapping that was reported by Streek et al. did not contribute to the overall separation process [50]. Additionally, electroosmotic effect was also investigated by DPD [107].

Along with investigating the HI effects on separation simulations, the effects of using short DNA fragments and the effects of different entropic trap geometries have also been studied. Laachi et al. investigated the transport of shorter, or rigid, DNA molecules

through periodic arrays of narrow channels [57]. Their theoretical analysis showed that it is unnecessary to operate near equilibrium to separate short DNA strands. According to their findings, long rigid DNA branches elute faster in strong electric fields. Fayad and Hadjiconstantiniou did similar work, but they studied the effects of different geometrics on entropic trap arrays [108]. Fayad and Hadjiconstantiniou used BD simulation with WLC model considering HI to study the effect of device geometry on the separation process for shorter DNAs. Optimization of the device was also studied [109]. Choi et al. used BD simulations to show the separation of shorter DNA chains in an alternating deep-shallow area nanofilter [110]. They suggested a new mechanism responsible for separating molecules in strong electric fields. The effect of the deep region's wall angle was studied on the separation process. They found that the shape of the entropic trap and the size of the rigid molecules were key factors that caused molecules to move along different electrophoretic streamlines. Results showed that the shorter branches were more likely to migrate to the bottom streamlines and stay there. Zhang et al. performed BD simulation with HI to study the separation of DNA using a device with nanoslits and nanopits with a similar design as in the entropic traps, but DNA is moved by flow. They found that HI plays important role in the separation mechanism [66].

4.6. ROTATIONAL FLOW

Microscale rotational flows, or streaming flows, with counter-rotating vortices have been known as another method for trapping particles, or DNA strands [77, 111-113]. The vortices can be generated by acoustically driven bubbles [111] or by local heating [112]. An inhomogeneous shear gradient in the vortices causes a difference in the

deformation of DNA molecules according to DNA lengths. As a result, the position and conformation of DNA molecules in those vortices will also be length dependent.

Watari et al. performed a BD simulation using WLC model and an analytic stream of Taylor-vortex flow. The inclusion of HIs were conducted in the same manner as in the Equations (11) and (12), excluding DNA-wall HI. They investigated the effect of vortex flow conditions on DNA conformations and positions to show the potential for trapping DNA in vortices [113]. Alfahani et al. [77] used the LBM to evaluate the rotating flow field and to include HIs. The LBM followed the same methodology as in the work done by Usta et al. [71, 72]. BD simulation of WLC in the rotating flow was performed. It is noteworthy that one wall of the microfluidic device was modeled as a "stick wall" on which DNA was trapped by a temperature gradient [112]. The simulation showed that there was a condition that needed to be fulfilled to separate DNA strands by length. If flow was strong enough, DNA strands were pushed out of the vortex and compressed against the wall. However, if the wall did not have enough strength to hold the compressed DNA, it was pulled by the hydrodynamic drag force back into the vortex. If the flow strength and the wall trapping force are tuned, short DNA strands are trapped in the trap region, the region between two vortices on the stick wall, and long DNA strands rotate freely in the vortices [77].

4.7. NANOPORE TRANSLOCATION

It was discovered that the sequencing and detection of DNA and RNA strands can be possible by forcing them through a narrow biological nanopore using an electric field, as shown in Figure 6 [114, 115]. If the size difference between the molecules and the

pores is large, molecules are squeezed through the pore. This is called nanopore translocation. This method enables DNA sequencing to be faster than conventional gel electrophoresis methods because base pair identification can be done as soon as strands pass through the pore. In order for the translocation process to be better understood for further applications, the conformational behavior of the DNA chain during the process needs to be investigated using simulation methods.

A BD simulation of this process was done by Tian and Smith and considered the repulsive force from the nanopore's walls [116]. In the simulation, it was assumed that the process was dominated by the force field rather than the entropic barrier effect. Investigation of the conformation difference before and after translocation, found that the polymer chains were not in equilibrium during the process. Izmitli et al. took HI into account in their simulation study [117]. They used a bead-spring model to represent the DNA chain and LBM to simulate the streamlines. They found that HI effects are a minor factor in determining residence time of the polymer. Luo et al. performed a 3D simulation of the process under an external force field to find the correct relation of residence time and external force. For slow and fast translocation processes the dependencies were found to be different [118]. Smiatek and Schmid performed a DPD to consider the effects of solvent choice on translocation. They considered the effect of different salt concentrations and surface slip conditions. The results of simulation showed that the role of surface slippage in polymer migration was very strong and may be considered as an important parameter in future microfluidic designs [119]. A different aspect of DNA translocation through a nanopores was investigated by de Haan et al. They used coarse-grained simulations that took the Peclet number, the ratio between convection and

diffusion, as a regime deterministic parameter in the simulation. They found that the probability of translocation to occur was found to be highly dependent on the Peclet number [120].

Similar to the studies on DNA structure in nanoconfinement [5], many MC simulation approaches have been used to investigate the mechanism [121] and the relation between the average residence time in a pore and the DNA length [122]. Molecular Dynamic simulation can be used in simulating the nanopore translocation of polyelectrolyte molecules [123, 124] as well because structures on a nanopore scale are similar to those on an atomic scale.
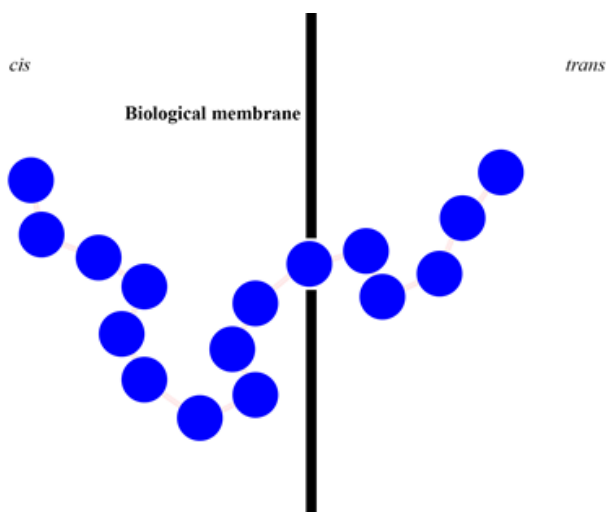
Figure 6. Schematic demonstration of the nanopore translocation: DNA molecule is pushed through a nanopore by electric field. (Redrawn from [115]).

5. CONCLUDING REMARKS AND PERSPECTIVES

In this study, we have reviewed the computational studies of DNA separations in micro-fabricated devices. We focused on the dynamic simulation of double stranded DNA in geometries related to separation methods and devices. The reviewed simulation

approaches can also be extended to the dynamic simulation of other biopolymers in

microscale flows [2]. The simulation approaches covered combining single polymer

dynamic calculations and inhomogeneous field calculations consistently. The general

simulation approach is to use a BD simulation of a WLC model with the calculation of an

inhomogeneous flow, or force, field using FEM. However, other methods may be adapted

depending on specific conditions to maximize efficiency and accuracy. With advances in

the field of micro-fabricated devices, more complex and confined geometries have been

involved in new design of DNA separation/manipulation devices. Therefore, polymer

models and field calculation methods must be developed to accurately capture and predict

DNA behaviors in those new devices. Furthermore, the importance of the inclusion of

HIs has been emphasized in conditions of nano-scale confinement [50] or high shear rate

[49]. In recent advancements, there have been attempts to utilize commercial

computational tools to perform DNA separation simulations. We have been directly

involved with this by utilizing COMSOL Multiphysics®, a physics modeling tool, to

simulate DNA separation [125].

GLOSSARY

BD: Brownian dynamics simulation

BEM: Boundary element method

CE: Capillary electrophoresis

DPD: Dissipative particle dynamics

FDM: Finite difference method

FEM: Finite element method

FENE: Finite extensibility nonlinear elastic chain

HI: Hydrodynamic interaction

LBM: Lattice-Boltzmann method

MC: Monte-Carlo

WLC: Worm-like chain model

ACKNOWLEDGEMENTS

REFERENCES

[1]   Marshall, E. (2000) Human Genome: Rival Genome Sequencers Celebrate a
        Milestone Together. Science, 288, 2294-2295.
        http://dx.doi.org/10.1126/science.288.5475.2294.

[2]   Marciel, A.B. and Schroeder, C.M. (2013) New Directions in Single Polymer
        Dynamics. Journal of Polymer Science Part B: Polymer Physics, 51, 556-566.
        http://dx.doi.org/10.1002/polb.23264.

[3]   Tegenfeldt, J.O., Prinz, C., Huang, R.L., Austin, R.H., Chou, S.Y., Cox, E.C.,
        Sturm, J.C. and Cao, H. (2004) Micro- and Nanofluidics for DNA Analysis.
        Analytical and Bioanalytical Chemistry, 378, 1678-1692.
        http://dx.doi.org/10.1007/s00216-004-2526-0.

[4]   Chen, Y.L., Graham, M.D., de Pablo, J.J., Randall, G.C., Gupta, M. and Doyle,
        P.S. (2004) Conformation and Dynamics of Single DNA Molecules in Parallel-
        Plate Slit Microchannels. Physical Review E, 70, 60901.
        http://dx.doi.org/10.1103/physreve.70.060901.

[5]   Dai, L., Renner, C.B. and Doyle, P.S. (2016) The Polymer Physics of Single DNA
        Confined in Nanochannels. Advances in Colloid and Interface Science, 232, 80-
        100. http://dx.doi.org/10.1016/j.cis.2015.12.002.

[6]   Hsieh, C.-C. and Doyle, P.S. (2008) Studying Confined Polymers Using Single-Molecule DNA Experiments. Korea-Australia Rheology Journal, 20, 127-142.

[7]   Alberts, B., Johnson, A., Lewis, J., Raff, M., Roberts, K. and Walter, P. (2002) Isolating, Cloning, and Sequencing DNA, 4th ed., Garland Science,New York.

[8]   Tian, H. (2000) Rapid Detection of Deletion, Insertion, and Substitution Mutations Via Heteroduplex Analysis Using Capillary- and Microchip-Based Electrophoresis. Genome Research, 10, 1403-1413. http://dx.doi.org/10.1101/gr.132700.

[9]   Slater, G.W., Holm, C., Chubynsky, M.V., de Haan, H.W., Dubé, A., Grass, K., Hickey, O.A., Kingsburry, C., Sean, D., Shendruk, T.N. and Zhan, L. (2009) Modeling the Separation of Macromolecules: A Review of Current Computer Simulation Methods. Electrophoresis, 30, 792-818. http://dx.doi.org/10.1002/elps.200800673.

[10]   Patrinos, G.P., Danielson, P.B. and Ansorge, W.J. (2017) Molecular Diagnostics: Past, Present, and Future, in: Molecular Diagnostics, Elsevier, pp. 1-11.

[11]   Ashton, R., Padala, C. and Kane, R.S. (2003) Microfluidic Separation of DNA. Current Opinion in Biotechnology, 14, 497-504. http://dx.doi.org/10.1016/s0958-1669(03)00113-7.

[12]   Han, J. and Craighead, H.G. (2002) Characterization and Optimization of an Entropic Trap for DNA Separation. Analytical Chemistry, 74, 394-401. http://dx.doi.org/10.1021/ac0107002.

[13]   Cho, J. and Dorfman, K.D. (2010) Brownian Dynamics Simulations of Electrophoretic DNA Separations in a Sparse Ordered Post Array. Journal of Chromatography A, 1217, 5522-5528. http://dx.doi.org/10.1016/j.chroma.2010.06.057.

[14]   Pasciak, P., Krawczyk, M.J., Gudowska-Nowak, E. and Kulakowski, K. (2005) Diffusion of DNA Molecules in Gel at High Electric Fields. Journal of Biological Physics, 31, 365-373. http://dx.doi.org/10.1007/s10867-005-7287-2.

[15]   Dorfman, K.D. and Viovy, J.-L. (2004) Semiphenomenological Model for the Dispersion of DNA During Electrophoresis in a Microfluidic Array of Posts. Physical Review E, 69, 11901. http://dx.doi.org/10.1103/physreve.69.011901.

[16]   Duke, T., Viovy, J.-L. and Semenov, A.N. (1994) Electrophoretic Mobility of DNA in Gels. I. New Biased Reptation Theory Including Fluctuations. Biopolymers, 34, 239-247. http://dx.doi.org/10.1002/bip.360340210.

[17]   Minc, N., Bokov, P., Zeldovich, K.B., Fütterer, C., Viovy, J.-L. and Dorfman, K.D. (2005) Motion of Single Long DNA Molecules through Arrays of Magnetic Columns. Electrophoresis, 26, 362-375. http://dx.doi.org/10.1002/elps.200410115.

[18]   Patel, P.D. and Shaqfeh, E.S.G. (2003) A Computational Study of DNA Separations in Sparse Disordered and Periodic Arrays of Posts. The Journal of Chemical Physics, 118, 2941-2951. http://dx.doi.org/10.1063/1.1532729.

[19]   Park, J.D., Myung, J.S. and Ahn, K.H. (2016) A Review on Particle Dynamics Simulation Techniques for Colloidal Dispersions: Methods and Applications. Korean Journal of Chemical Engineering, 33, 3069-3078. http://dx.doi.org/10.1007/s11814-016-0229-9.

[20]   Vidal-Meza, M.P., Zhou, R., Barua, S., Wang, C. and Park, J. (2016) Simulation of Interstitial Nanoparticle Flow for Development of Tumor-on-a-Chip Device. Proceedings of 2016 COMSOL Conference in Boston, https://www.comsol.com/paper/download/362411/park_paper.pdf.

[21]   Streek, M.A. (2005) Brownian Dynamics Simulation of Migration of DNA in Structured Microchannels. Bielefeld University, Bielefeld.

[22]   Knotts, T.A., Rathore, N., Schwartz, D.C. and de Pablo, J.J. (2007) A Coarse Grain Model for DNA. The Journal of Chemical Physics, 126, 084901. http://dx.doi.org/10.1063/1.2431804.

[23]   Zhang, Y. (2011) Brownian Dynamics Simulation of DNA in Complex Geometries. University of Wisconsin -Madison, Madison.

[24]   Bird, R.B., Curtiss, C.F., Armstrong, R.C. and Hassager, O. (1987) Dynamics of Polymeric Liquids.Volume 2: Kinetic Theory, John Wiley & Sons, Inc,New York.

[25]   Hagerman, P.J. and Zimm, B.H. (1981) Monte Carlo Approach to the Analysis of the Rotational Diffusion of Wormlike Chains. Biopolymers, 20, 1481-1502. http://dx.doi.org/10.1002/bip.1981.360200709.

[26]   Duke, T.A.J. and Viovy, J.L. (1992) Simulation of Megabase DNA Undergoing Gel Electrophoresis. Physical Review Letters, 68, 542-545. http://dx.doi.org/10.1103/physrevlett.68.542.

[27]   Tree, D.R., Wang, Y. and Dorfman, K.D. (2013) Modeling the Relaxation Time of DNA Confined in a Nanochannel. Biomicrofluidics, 7, 054118. http://dx.doi.org/10.1063/1.4826156.

[28]   Underhill, P.T. and Doyle, P.S. (2004) On the Coarse-Graining of Polymers into Bead-Spring Chains. Journal of Non-Newtonian Fluid Mechanics, 122, 3-31. http://dx.doi.org/10.1016/j.jnnfm.2003.10.006.

[29]   Liu, B., Wang, J., Fan, X., Kong, Y. and Gao, H. (2008) An Effective Bead–Spring Model for Polymer Simulation. Journal of Computational Physics, 227, 2794-2807. http://dx.doi.org/10.1016/j.jcp.2007.11.012.

[30]   Park, J., Mead, D.W. and Denn, M.M. (2012) Stochastic Simulation of Entangled Polymeric Liquids in Fast Flows: Microstructure Modification. Journal of Rheology, 56, 1057-1081. http://dx.doi.org/10.1122/1.4720086.

[31]   Banerjee, N. and Park, J. (2015) Modeling and Simulation of Biopolymer Networks: Classification of the Cytoskeleton Models According to Multiple Scales. Korean Journal of Chemical Engineering, 32, 1207-1217. http://dx.doi.org/10.1007/s11814-015-0071-5.

[32]   Barrat, J.-L. and Joanny, J.-F. (1996) Theory of Polyelectrolyte Solutions. Advances in Chemical Physics, 94, 1-66. https://doi.org/10.1002/9780470141533.ch1.

[33]   Long, D. and Ajdari, A. (2001) A Note on the Screening of Hydrodynamic Interactions, in Electrophoresis, and in Porous Media. The European Physical Journal E, 4, 29-32. http://dx.doi.org/10.1007/s101890170139.

[34]   Long, D., Viovy, J.-L. and Ajdari, A. (1996) A Zimm Model for Polyelectrolytes in an Electric Field. Journal of Physics: Condensed Matter, 8, 9471-9475. http://dx.doi.org/10.1088/0953-8984/8/47/047.

[35]   Streek, M., Schmid, F., Duong, T.T. and Ros, A. (2004) Mechanisms of DNA Separation in Entropic Trap Arrays: A Brownian Dynamics Simulation. Journal of Biotechnology, 112, 79-89. http://dx.doi.org/10.1016/j.jbiotec.2004.04.021.

[36]   Streek, M., Schmid, F., Duong, T.T., Anselmetti, D. and Ros, A. (2005) Two-State Migration of DNA in a Structured Microchannel. Physical Review E, 71, 11905. http://dx.doi.org/10.1103/physreve.71.011905.

[37]   Fan, X., Phan-Thien, N., Yong, N.T., Wu, X. and Xu, D. (2003) Microchannel Flow of a Macromolecular Suspension. Physics of Fluids, 15, 11-21. http://dx.doi.org/10.1063/1.1522750.

[38]   Cifra, P., Benková, Z. and Bleha, T.s. (2009) Chain Extension of DNA Confined in Channels. The Journal of Physical Chemistry B, 113, 1843-1851. http://dx.doi.org/10.1021/jp806126r.

[39]   Azuma, R. and Takayama, H. (2002) Brownian Dynamics Studies on DNA Gel
        Electrophoresis. I. Numerical Method and "Periodic" Behavior of Elongation-
        Contraction Motions. The Journal of Chemical Physics, 117, 6863-6872.
        http://dx.doi.org/10.1063/1.1505867.

[40]   Larson, R.G., Perkins, T.T., Smith, D.E. and Chu, S. (1997) Hydrodynamics of a
        DNA Molecule in a Flow Field. Physical Review E, 55, 1794-1797.
        http://dx.doi.org/10.1103/physreve.55.1794.

[41]   Jendrejack, R.M., Graham, M.D. and de Pablo, J.J. (2000) Hydrodynamic
        Interactions in Long Chain Polymers: Application of the Chebyshev Polynomial
        Approximation in Stochastic Simulations. The Journal of Chemical Physics, 113,
        2894-2900. http://dx.doi.org/10.1063/1.1305884.

[42]   Jendrejack, R.M., de Pablo, J.J. and Graham, M.D. (2002) Stochastic Simulations
        of DNA in Flow: Dynamics and the Effects of Hydrodynamic Interactions. The
        Journal of Chemical Physics, 116, 7752-7759.
        http://dx.doi.org/10.1063/1.1466831

[43]   Jendrejack, R.M., Dimalanta, E.T., Schwartz, D.C., Graham, M.D. and de Pablo,
        J.J. (2003) DNA Dynamics in a Microchannel. Physical Review Letters, 91,
        38102. http://dx.doi.org/10.1103/physrevlett.91.038102.

[44]   Jendrejack, R.M., Schwartz, D.C., de Pablo, J.J. and Graham, M.D. (2004) Shear-
        Induced Migration in Flowing Polymer Solutions: Simulation of Long-Chain
        DNA in Microchannels. The Journal of Chemical Physics, 120, 2513-2529.
        http://dx.doi.org/10.1063/1.1637331.

[45]   Kim, J.M. and Doyle, P.S. (2006) A Brownian Dynamics-Finite Element Method
        for Simulating DNA Electrophoresis in Nonhomogeneous Electric Fields. The
        Journal of Chemical Physics, 125, 074906. http://dx.doi.org/10.1063/1.2222374.

[46]   Heyes, D.M. and Melrose, J.R. (1993) Brownian Dynamics Simulations of Model
        Hard-Sphere Suspensions. Journal of Non-Newtonian Fluid Mechanics, 46, 1-28.
        http://dx.doi.org/10.1016/0377-0257(93)80001-r.

[47]   Balducci, A., Mao, P., Han, J. and Doyle, P.S. (2006) Double-Stranded DNA
        Diffusion in Slitlike Nanochannels. Macromolecules, 39, 6273-6281.
        https://10.1021/ma061047t.

[48]   Butler, J.E., Usta, O.B., Kekre, R. and Ladd, A.J.C. (2007) Kinetic Theory of a
        Confined Polymer Driven by an External Force and Pressure-Driven Flow.
        Physics of Fluids, 19, 113101. http://dx.doi.org/10.1063/1.2801409.

[49]   Kekre, R., Butler, J.E. and Ladd, A.J.C. (2010) Role of Hydrodynamic
        Interactions in the Migration of Polyelectrolytes Driven by a Pressure Gradient
        and an Electric Field. Physical Review E, 82, 50803.
        http://dx.doi.org/10.1103/physreve.82.050803.

[50]   Pan, H., Ng, T.Y., Li, H. and Moeendarbary, E. (2010) Dissipative Particle
        Dynamics Simulation of Entropic Trapping for DNA Separation. Sensors and
        Actuators A: Physical, 157, 328-335. http://dx.doi.org/10.1016/j.sna.2009.11.027.

[51]   Rotne, J. and Prager, S. (1969) Variational Treatment of Hydrodynamic
        Interaction in Polymers. The Journal of Chemical Physics, 50, 4831-4837.
        http://dx.doi.org/10.1063/1.1670977.

[52]   Bustamante, C., Bryant, Z. and Smith, S.B. (2003) Ten Years of Tension: Single-
        Molecule DNA Mechanics. Nature, 421, 423-427.
        http://dx.doi.org/10.1038/nature01405.

[53]   Dai, L. and Doyle, P.S. (2013) Comparisons of a Polymer in Confinement Versus
        Applied Force. Macromolecules, 46, 6336-6344.
        http://dx.doi.org/10.1021/ma400674q.

[54]   Butler, J.E. and Shaqfeh, E.S.G. (2005) Brownian Dynamics Simulations of a
        Flexible Polymer Chain Which Includes Continuous Resistance and Multibody
        Hydrodynamic Interactions. The Journal of Chemical Physics, 122, 014901.
        http://dx.doi.org/10.1063/1.1828432.

[55]   Liron, N. and Mochon, S. (1976) Stokes Flow for a Stokeslet between Two
        Parallel Flat Plates. Journal of Engineering Mathematics, 10, 287-303.
        http://dx.doi.org/10.1007/bf01535565.

[56]   Saintillan, D., Shaqfeh, E.S.G. and Darve, E. (2006) Effect of Flexibility on the
        Shear-Induced Migration of Short-Chain Polymers in Parabolic Channel Flow.
        Journal of Fluid Mechanics, 557, 297-306.
        http://dx.doi.org/10.1017/s0022112006000243.

[57]   Laachi, N., Declet, C., Matson, C. and Dorfman, K.D. (2007) Nonequilibrium
        Transport of Rigid Macromolecules in Periodically Constricted Geometries.
        Physical Review Letters, 98, 98106.
        http://dx.doi.org/10.1103/physrevlett.98.098106.

[58]   Park, J. and Butler, J.E. (2009) Inhomogeneous Distribution of a Rigid Fibre
        Undergoing Rectilinear Flow between Parallel Walls at High Péclet Numbers.
        Journal of Fluid Mechanics, 630, 267-298.
        http://dx.doi.org/10.1017/s0022112009006545.

[59]   Micheletti, C. and Orlandini, E. (2012) Numerical Study of Linear and Circular Model DNA Chains Confined in a Slit: Metric and Topological Properties. Macromolecules, 45, 2113-2121. http://dx.doi.org/10.1021/ma202503k.

[60]   Muralidhar, A., Tree, D.R., Wang, Y. and Dorfman, K.D. (2014) Interplay between Chain Stiffness and Excluded Volume of Semiflexible Polymers Confined in Nanochannels. The Journal of Chemical Physics, 140, 084905. http://dx.doi.org/10.1063/1.4865965.

[61]   Dai, L., Tree, D.R., van der Maarel, J.R.C., Dorfman, K.D. and Doyle, P.S. (2013) Revisiting Blob Theory for DNA Diffusivity in Slitlike Confinement. Physical Review Letters, 110, 168105. http://dx.doi.org/10.1103/physrevlett.110.168105.

[62]   Kim, J.M. and Doyle, P.S. (2007) Brownian Dynamics Simulations of a DNA Molecule Colliding with a Small Cylindrical Post. Macromolecules, 40, 9151-9163. http://dx.doi.org/10.1021/ma0710434.

[63]   Han, J. and Craighead, H.G. (1999) Entropic Trapping and Sieving of Long DNA Molecules in a Nanofluidic Channel. Journal of Vacuum Science & Technology A: Vacuum, Surfaces, and Films, 17, 2142-2147. http://dx.doi.org/10.1116/1.581740.

[64]   Cho, J., Kenward, M. and Dorfman, K.D. (2009) A Boundary Element Method/Brownian Dynamics Approach for Simulating DNA Electrophoresis in Electrically Insulating Microfabricated Devices. Electrophoresis, 30, 1482-1489. http://dx.doi.org/10.1002/elps.200800582.

[65]   Blake, J.R. (1971) A Note on the Image System for a Stokeslet in a No-Slip Boundary. Mathematical Proceedings of the Cambridge Philosophical Society, 70, 303-310. http://dx.doi.org/10.1017/s0305004100049902.

[66]   Zhang, Y., de Pablo, J.J. and Graham, M.D. (2012) An Immersed Boundary Method for Brownian Dynamics Simulation of Polymers in Complex Geometries: Application to DNA Flowing through a Nanoslit with Embedded Nanopits. The Journal of Chemical Physics, 136, 014901. http://dx.doi.org/10.1063/1.3672103.

[67]   Hernández-Ortiz, J.P., de Pablo, J.J. and Graham, M.D. (2007) Fast Computation of Many-Particle Hydrodynamic and Electrostatic Interactions in a Confined Geometry. Physical Review Letters, 98, 140602. http://dx.doi.org/10.1103/physrevlett.98.140602.

[68]   Mittal, R. and Iaccarino, G. (2005) Immersed Boundary Methods. Annual Review of Fluid Mechanics, 37, 239-261. http://dx.doi.org/10.1146/annurev.fluid.37.061903.175743.

[69]   Ermak, D.L. and McCammon, J.A. (1978) Brownian Dynamics with Hydrodynamic Interactions. The Journal of Chemical Physics, 69, 1352-1360. http://dx.doi.org/10.1063/1.436761.

[70]   Fixman, M. (1986) Construction of Langevin Forces in the Simulation of Hydrodynamic Interaction. Macromolecules, 19, 1204-1207. http://dx.doi.org/10.1021/ma00158a043.

[71]   Usta, O.B., Ladd, A.J.C. and Butler, J.E. (2005) Lattice-Boltzmamm Simulations of the Dynamics of Polymer Solutions in Periodic and Confined Geometries. The Journal of Chemical Physics, 122, 94902. https://doi.org/10.1063/1.1854151.

[72]   Usta, O.B., Butler, J.E. and Ladd, A.J.C. (2007) Transverse Migration of a Confined Polymer Driven by an External Force. Physical Review Letters, 98, 98301. http://dx.doi.org/10.1103/physrevlett.98.098301.

[73]   Bhatnagar, P.L., Gross, E.P. and Krook, M. (1954) A Model for Collision Processes in Gases. I. Small Amplitude Processes in Charged and Neutral One-Component Systems. Physical Review, 94, 511-525. http://dx.doi.org/10.1103/physrev.94.511.

[74]   Chen, Y.L., Ma, H., Graham, M.D. and de Pablo, J.J. (2007) Modeling DNA in Confinement: A Comparison between the Brownian Dynamics and Lattice Boltzmann Method. Macromolecules, 40, 5978-5984. http://dx.doi.org/10.1021/ma070729t.

[75]   Kekre, R., Butler, J.E. and Ladd, A.J.C. (2010) Comparison of Lattice-Boltzmann and Brownian-Dynamics Simulations of Polymer Migration in Confined Flows. Physical Review E, 82, 011802. http://dx.doi.org/10.1103/physreve.82.011802.

[76]   Shan, X. and Chen, H. (2007) A General Multiple-Relaxation-Time Boltzmann Collision Model. International Journal of Modern Physics C, 18, 635-643. http://dx.doi.org/10.1142/s0129183107010887.

[77]   Alfahani, F., Antonelli, M. and Kreft Pearce, J. (2015) Separation of DNA by Length in Rotational Flow: Lattice-Boltzmann-Based Simulations. Biomicrofluidics, 9, 044107. http://dx.doi.org/10.1063/1.4926667.

[78]   Moeendarbary, E., Ng, T.Y. and Zangeneh, M. (2009) Dissipative Particle Dynamics: Introduction, Methodology and Complex Fluid Applications — a Review. International Journal of Applied Mechanics, 1, 737-763. http://dx.doi.org/10.1142/s1758825109000381.

[79]   Español, P. and Warren, P. (1995) Statistical Mechanics of Dissipative Particle Dynamics. Europhysics Letters, 30, 191-196. http://dx.doi.org/10.1209/0295-5075/30/4/001.

[80] Hoogerbrugge, P.J. and Koelman, J.M.V.A. (1992) Simulating Microscopic Hydrodynamic Phenomena with Dissipative Particle Dynamics. Europhysics Letters, 19, 155-160. http://dx.doi.org/10.1209/0295-5075/19/3/001.

[81] Fan, X., Phan-Thien, N., Chen, S., Wu, X. and Yong Ng, T. (2006) Simulating Flow of DNA Suspension Using Dissipative Particle Dynamics. Physics of Fluids, 18, 063102. http://dx.doi.org/10.1063/1.2206595.

[82] Litvinov, S. (2014) Mesoscopic Simulation of DNA Using Smoothed Dissipative Particle Dynamics. Universität München, München.

[83] Moeendarbary, E., Ng, T.Y., Pan, H. and Lam, K.Y. (2010) Migration of DNA Molecules through Entropic Trap Arrays: A Dissipative Particle Dynamics Study. Microfluidics and Nanofluidics, 8, 243-254. http://dx.doi.org/10.1007/s10404-009-0463-0.

[84] Ranjith, S.K. (2015) Mesoscopic Simulation of Single DNA Dynamics in Rotational Flows. The European Physical Journal E, 38, 1-11. http://dx.doi.org/10.1140/epje/i2015-15089-0.

[85] Zhang, J. (2010) Lattice Boltzmann Method for Microfluidics: Models and Applications. Microfluidics and Nanofluidics, 10, 1-28. http://dx.doi.org/10.1007/s10404-010-0624-1.

[86] Peña, L.C., Argarañá, M.F., Zan, M.M.D., Giorello, A., Antuña, S., Prieto, C.C., Veaute, C.M.I. and Müller, D.M. (2017) New Amphiphilic Amino Acid Derivatives for Efficient DNA Transfection in Vitro≪/I&Gt. Advances in Chemical Engineering and Science, 7, 191-205. http://dx.doi.org/10.4236/aces.2017.72014.

[87] de Gennes, P.G. (1971) Reptation of a Polymer Chain in the Presence of Fixed Obstacles. The Journal of Chemical Physics, 55, 572-579. http://dx.doi.org/10.1063/1.1675789.

[88] Dorfman, K.D. (2010) Electrophoresis in Microfabricated Devices. REview of Modern Physics, 82, 2903-2947. https://doi.org/10.1103/RevModPhys.82.2903.

[89] Volkmuth, W.D. and Austin, R.H. (1992) DNA Electrophoresis in Microlithographic Arrays. Nature, 358, 600-602. http://dx.doi.org/10.1038/358600a0.

[90] Volkmuth, W.D., Duke, T., Wu, M.C., Austin, R.H. and Szabo, A. (1994) DNA Electrodiffusion in a 2d Array of Posts. Physical Review Letters, 72, 2117-2120. http://dx.doi.org/10.1103/physrevlett.72.2117.

[91]   Saville, P.M. and Sevick, E.M. (1999) Collision of a Field-Driven Polymer with a
         Finite-Sized Obstacle: A Brownian Dynamics Simulation. Macromolecules, 32,
         892-899. http://dx.doi.org/10.1021/ma981049g.

[92]   Randall, G.C. and Doyle, P.S. (2004) Electrophoretic Collision of a DNA
         Molecule with an Insulating Post. Physical Review Letters, 93, 58102.
         http://dx.doi.org/10.1103/physrevlett.93.058102.

[93]   Randall, G.C. and Doyle, P.S. (2006) Collision of a DNA Polymer with a Small
         Obstacle. Macromolecules, 39, 7734-7745. http://dx.doi.org/10.1021/ma061375t.

[94]   Teclemariam, N.P., Beck, V.A., Shaqfeh, E.S.G. and Muller, S.J. (2007)
         Dynamics of DNA Polymers in Post Arrays: Comparison of Single Molecule
         Experiments and Simulations. Macromolecules, 40, 3848-3859.
         http://dx.doi.org/10.1021/ma062892e.

[95]   Ou, J., Cho, J., Olson, D.W. and Dorfman, K.D. (2009) DNA Electrophoresis in a
         Sparse Ordered Post Array. Physical Review E, 79, 61904.
         http://dx.doi.org/10.1103/physreve.79.061904.

[96]   Slater, G.W., Desruisseaux, C., Hubert, S.J., Mercier, J.-F., Labrie, J., Boileau, J.,
         Tessier, F. and Pépin, M.P. (2000) Theory of DNA Electrophoresis: A Look at
         Some Current Challenges. Electrophoresis, 21, 3873-3887.
         http://dx.doi.org/10.1002/1522-2683(200012)21:18<3873::aid-elps3873>3.3.co;2-
         #.

[97]   Ennis, J. and White, L.R. (1997) Electrophoretic Mobility of a Semi-Dilute
         Suspension of Spherical Particles with Thick Double Layers and Low Zeta
         Potentials. Journal of Colloid and Interface Science, 185, 157-173.
         http://dx.doi.org/10.1006/jcis.1996.4565.

[98]   Zheng, J. and Yeung, E.S. (2003) Mechanism for the Separation of Large
         Molecules Based on Radial Migration in Capillary Electrophoresis. Analytical
         Chemistry, 75, 3675-3680. http://dx.doi.org/10.1021/ac034430u.

[99]   Pandey, H. and Underhill, P.T. (2015) Coarse-Grained Model of Conformation-
         Dependent Electrophoretic Mobility and Its Influence on DNA Dynamics.
         Physical Review E, 92, 052301. http://dx.doi.org/10.1103/physreve.92.052301.

[100]   Schimpf, M.E., Caldwell, K. and Giddings, J.C. (2000) Field-Flow Fractionation
         Handbook, Wiley-Science,New York.

[101]   Chen, Z. and Chauhan, A. (2005) Separation of Charged Colloids by a
         Combination of Pulsating Lateral Electric Fields and Poiseuille Flow in a 2d
         Channel. Journal of Colloid and Interface Science, 282, 212-222.
         http://dx.doi.org/10.1016/j.jcis.2004.08.059.

[102] Chen, Z. and Chauhan, A. (2005) DNA Separation by Efff in a Microchannel. Journal of Colloid and Interface Science, 285, 834-844. http://dx.doi.org/10.1016/j.jcis.2004.11.061.

[103] Arvanitidou, E. and Hoagland, D. (1991) Chain-Length Dependence of the Electrophoretic Mobility in Random Gels. Physical Review Letters, 67, 1464-1466. http://dx.doi.org/10.1103/physrevlett.67.1464.

[104] Tessier, F., Labrie, J. and Slater, G.W. (2002) Electrophoretic Separation of Long Polyelectrolytes in Submolecular-Size Constrictions: A Monte Carlo Study. Macromolecules, 35, 4791-4800. http://dx.doi.org/10.1021/ma0110406.

[105] Panwar, A.S. and Kumar, S. (2006) Time Scales in Polymer Electrophoresis through Narrow Constrictions: A Brownian Dynamics Study. Macromolecules, 39, 1279-1289. http://dx.doi.org/10.1021/ma051041o.

[106] Lee, Y.M. and Joo, Y.L. (2007) Brownian Dynamics Simulations of Polyelectrolyte Molecules Traveling through an Entropic Trap Array During Electrophoresis. The Journal of Chemical Physics, 127, 124902. http://dx.doi.org/10.1063/1.2777157.

[107] Duong-Hong, D., Wang, J.-S., Liu, G.R., Chen, Y.Z., Han, J. and Hadjiconstantinou, N.G. (2007) Dissipative Particle Dynamics Simulations of Electroosmotic Flow in Nano-Fluidic Devices. Microfluidics and Nanofluidics, 4, 219-225. http://dx.doi.org/10.1007/s10404-007-0170-7.

[108] Fayad, G.N. and Hadjiconstantinou, N.G. (2013) Modeling the Electrophoretic Separation of Short Biological Molecules in Nanofluidic Devices. Journal of Fluids Engineering, 135, 024501. http://dx.doi.org/10.1115/1.4023445.

[109] Fayad, G.N. and Hadjiconstantinou, N.G. (2009) Realistic Brownian Dynamics Simulations of Biological Molecule Separation in Nanofluidic Devices. Microfluidics and Nanofluidics, 8, 521-529. http://dx.doi.org/10.1007/s10404-009-0483-9.

[110] Choi, S., Kim, J.M., Ahn, K.H. and Lee, S.J. (2014) High-Throughput DNA Separation in Nanofilter Arrays. Electrophoresis, 35, 2068-2077. http://dx.doi.org/10.1002/elps.201470130.

[111] Wang, C., Jalikop, S.V. and Hilgenfeldt, S. (2011) Size-Sensitive Sorting of Microparticles through Control of Flow Geometry. Applied Physics Letters, 99, 034101. http://dx.doi.org/10.1063/1.3610940.

[112] Braun, D. (2004) Pcr by Thermal Convection. Modern Physics Letters B, 18, 775-784. http://dx.doi.org/10.1142/s0217984904007049.

[113] Watari, N., Doi, M. and Larson, R.G. (2008) Fluidic Trapping of Deformable Polymers in Microflows. Physical Review E, 78, 011801. http://dx.doi.org/10.1103/physreve.78.011801.

[114] Deamer, D.W. and Akeson, M. (2000) Nanopores and Nucleic Acids: Prospects for Ultrarapid Sequencing. Trends in Biotechnology, 18, 147-151. http://dx.doi.org/10.1016/s0167-7799(00)01426-8.

[115] Kantor, Y. and Kardar, M. (2004) Anomalous Dynamics of Forced Translocation. Physicla Review E, 69, 021806. https://doi.org/10.1103/PhysRevE.69.021806.

[116] Tian, P. and Smith, G.D. (2003) Translocation of a Polymer Chain across a Nanopore: A Brownian Dynamics Simulation Study. The Journal of Chemical Physics, 119, 11475-11483. http://dx.doi.org/10.1063/1.1621614.

[117] Izmitli, A., Schwartz, D.C., Graham, M.D. and de Pablo, J.J. (2008) The Effect of Hydrodynamic Interactions on the Dynamics of DNA Translocation through Pores. The Journal of Chemical Physics, 128, 085102. http://dx.doi.org/10.1063/1.2831777.

[118] Luo, K., Ala-Nissila, T., Ying, S.C. and Metzler, R. (2009) Driven Polymer Translocation through Nanopores: Slow-Vs.-Fast Dynamics. Europhysics Letters, 88, 68006. http://dx.doi.org/10.1209/0295-5075/88/68006.

[119] Smiatek, J. and Schmid, F. (2010) Polyelectrolyte Electrophoresis in Nanochannels: A Dissipative Particle Dynamics Simulation. The Journal of Physical Chemistry B, 114, 6266-6272. http://dx.doi.org/10.1021/jp100128p.

[120] de Haan, H.W., Sean, D. and Slater, G.W. (2015) Using a Péclet Number for the Translocation of a Polymer through a Nanopore to Tune Coarse-Grained Simulations to Experimental Conditions. Physical Review E, 91, 022601. http://dx.doi.org/10.1103/physreve.91.022601.

[121] Muthukumar, M. (1999) Polymer Translocation through a Hole. The Journal of Chemical Physics, 111, 10371-10374. http://dx.doi.org/10.1063/1.480386.

[122] Panja, D. and Barkema, G.T. (2008) Passage Times for Polymer Translocation Pulled through a Narrow Pore. Biophysical Journal, 94, 1630-1637. http://dx.doi.org/10.1529/biophysj.107.116434.

[123] Belkin, M. and Aksimentiev, A. (2016) Molecular Dynamics Simulation of DNA Capture and Transport in Heated Nanopores. ACS Applied Materials & Interfaces, 8, 12599-12608. http://dx.doi.org/10.1021/acsami.6b00463.

[124] Menais, T., Mossa, S. and Buhot, A. (2016) Polymer Translocation through Nano-Pores in Vibrating Thin Membranes. Scientific Reports, 6, 38558. http://dx.doi.org/10.1038/srep38558.

[125]   Monjezi, S., Palaniappan, M., Jones, J.D., Behdani, B. and Park, J. (2017) Dynamic Simulation of a Polymer Molecule Using COMSOL Multiphysics: DNA Separation in a Microchannel. Proceedings of 2017 COMSOL Conference in Boston, 4-6 Oct. 2017.

V. DYNAMIC SIMULATION OF A POLYMER MOLECULE USING COMSOL MULTIPHYSICS: DNA SEPARATION IN A MICROCHANNEL[4]

Saman Monjezi[1], Meyyammai B. Palaniappan[1], James D. Jones[1], Behrouz Behdani[1],

Joontaek Park[1*]

[1] Chemical and Biochemical Engineering Department, Missouri University of Science

and Technology, Rolla, MO, 65409

[*] Corresponding author: parkjoon@mst.edu

1. INTRODUCTION

DNA separation is used in a wide array of applications such as DNA characterization, fingerprinting, diagnosis and genome sequencing. Separating DNA by traditional methods, such as gel electrophoresis, can be time consuming and inefficient. Using microfluidic devices for DNA separation has been studied and deemed a more efficient separation method. However, the design and fabrication of such devices by trial-and-error can be time-consuming and costly. There have been computational studies finding the optimal design and investigating separation mechanisms within these devices. However, to the best of our knowledge, there hasn't been any application using commercial software to perform simulations of these systems. This is the first trial, where COMSOL Multiphysics® is used to simulate polymer dynamics [1]. This simulation study will open a new page for the application of COMSOL Multiphysics to the field of polymer dynamics and microfluidic device design. This study will also have an impact on

---

[4] This paper was published in *COMSOL Conference*, Boston, 2017.

biomedical applications involving the manipulation of biopolymer molecules. Among the many types of DNA separation methods, we focus on the separation of DNA by entropic traps. This type of separation consists of an array of structured microfluidic channels through which polymer molecules flow [2, 3].

2. BACKGROUND

It was found that DNA molecules can be separated based on their chain length using a series of structured microchannels with periodically different channel heights, also known as entropic trap arrays, where the narrow channel gap is much smaller than the gyration diameter ($2R_g$) of a DNA molecule, as depicted in Figure 1.

When negatively charged DNA molecules are driven through the narrow and wide channels by electrophoretic forces, the interactions between the DNA molecules and the channel causes length-dependent elution times. It was observed that longer DNA molecules usually had a larger mobility (faster elution) than smaller DNA molecules. This is opposite to the behavior exhibited by free-draining DNA molecules. The reason behind this counter-intuitive separation mechanism was investigated. It was found that longer DNA molecules have a higher probability of being sucked into the small channels, instead of stagnating in the larger channels, due to the longer molecules occupying more surface area [2, 3].
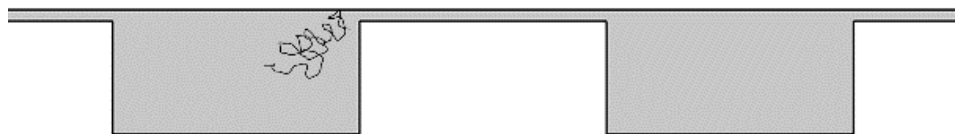

Figure 1. A 2D schematic view of an array of entropic traps. A DNA molecule in a wide channel is flowing into a narrow channel.

Many simulations have been performed to study the details of this separation mechanism. A simulation study by Streek et al. discovered a corner diffusion mechanism for the slower elution of a shorter DNA molecule: If the diffusivity of a DNA molecule is strong relative to the field strength, it tends to stay trapped in the corner of the wider channel [4]. There were simulation studies using the Dissipative Particle Dynamics simulation, which investigated the separation mechanism in 3D simulation and discussed the effect of hydrodynamic interactions [5]. Additionally, various entropic trap designs continue to be created. [6-15].

3. GOVERNING EQUATIONS / NUMERICAL MODEL

In this study, a Brownian dynamics (BD) simulation was performed using a coarse-grained bead-spring model to represent the semi-flexible dynamic nature of a λ-DNA molecule in the entropic trap channel. A coarse-grained model of a λ-DNA molecule consists of N_b beads and $N_b - 1$ springs. The bead-spring model is a well-known model for polymer dynamics and has been commonly used to study DNA dynamics in various type of microfluidic devices [1, 16]. The bead positions are determined by calculating sum of imposed forces on the beads at each time step. This is shown in equation (1).

$$\frac{d\left(m_p \frac{dr_i}{dt}\right)}{dt} = F_i^D + F_i^B + F_i^S + F_i^E + F_i^V \tag{1}$$

Here, m_p represents the mass of a bead, the subindex i denotes each bead, and r_i is the position of the bead at the corresponding time-step. F_i^D is the friction force which can be calculated using Stoke's drag law:

$$F_i^D = \zeta \frac{dr_i}{dt} \tag{2}$$

where ζ is a drag coefficient which represents the fluid friction exerted on the bead, i, which is moving through the solvent. For the case of spherical objects:

$$\zeta = 6\pi\mu r_p \tag{3}$$

In equation (3), μ is the dynamic viscosity of the fluid and r_p is the bead radius. F_i^B is the Brownian force. F_i^S is the net spring force. F_i^E is the electrophoretic force exerted on the charged beads. F_i^V is excluded volume force of the bead that prevents the beads from overlapping in the simulation.

The Brownian force is derived for spherical beads by considering the fluctuation-dissipation theory:

$$F_i^B = \sqrt{\frac{6k_B T \zeta}{\Delta t}} w_i(t) \tag{4}$$

where k_B is Boltzmann constant, T is the absolute temperature in Kelvin, and $w_i(t)$ is a random vector of a uniform distribution with a mean of 0 and a variance of 1. Each bead represents 4850 base pair long segment of the chain. Bead diameters are fixed to be $a = 77\ nm$ and the Worm-Like Chain (WLC) model springs, located between beads, follow the Marko-Siggia force rule:

$$F_{ij}^S = \frac{k_B T}{2b_k}\left[\left(1 - \frac{|r_j - r_i|}{N_{k,s}b_k}\right)^{-2} - 1 + \frac{4|r_j - r_i|}{N_{k,s}b_k}\right]\frac{r_j - r_i}{|r_j - r_i|} \tag{5}$$

where b_k is the Kuhn length for λ-DNA. $N_{k,s}$ is the number of Kuhn lengths in a spring, which is 20 for our simulation. Note here that the WLC model for spring forces is the most commonly used model in dynamic DNA simulations [17, 18].

The force exerted by electrical field can be expressed by:

$$F_i^E = qeE \tag{6}$$

where q is the charge number for each bead, e is electron charge, and E is the electrical field. q was calculated by a method explained in a previous work by Tessier et al. [8], and is -178 for each bead.

The interaction between the beads is described by the Lenard-Jones pairwise repulsion model and simulates the excluded volume of the beads:

$$F_i^V = \frac{24\varepsilon}{\sigma} \left[2 \left(\frac{\sigma}{|r_j - r_i|} \right)^{13} - \left(\frac{\sigma}{|r_j - r_i|} \right)^{7} \right] \left(\frac{r_j - r_i}{|r_j - r_i|} \right) \tag{7}$$

In equation (7), σ is the bead diameter and ε is repulsion energy. By substituting equations (2-5) into equation (1), the empirical model for the DNA chain is created and the DNA conformation through time can be derived. In our simulation, walls are assumed to be bouncy and bead interactions are defined by:

$$v_i = v_i^{old} - 2(\boldsymbol{n} \cdot v_i^{old})\boldsymbol{n} \tag{8}$$

where v_i is a bead's velocity.

4. SIMULATION

The geometry of this device was defined in an earlier work [6] and it is shown in Figure 2. The length of each period was $L = 10\mu m$, and ratio of the wide channel length to that of the narrow channel was 1.0. Height of the wide region and narrow region were respectively, $H_L = 1.0 \ \mu m$ and $H_s = 90 \ nm$. H_s is much smaller than the gyration diameter of a typical λ-DNA molecule (around $760 \ nm$). This fulfills an entropic array structural requirement mentioned earlier in this paper.
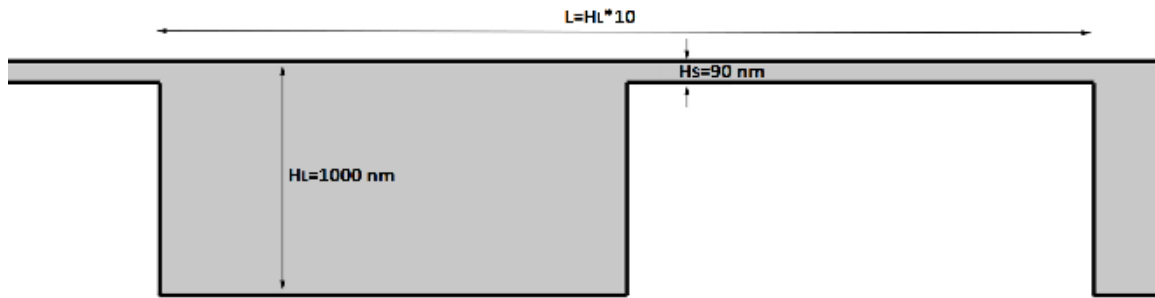
Figure 2. Channel structures used in simulations.

The Electric Currents Physics of the AC/DC module was chosen to calculate the steady state electric field across the channel, of which governing equation can be described as:
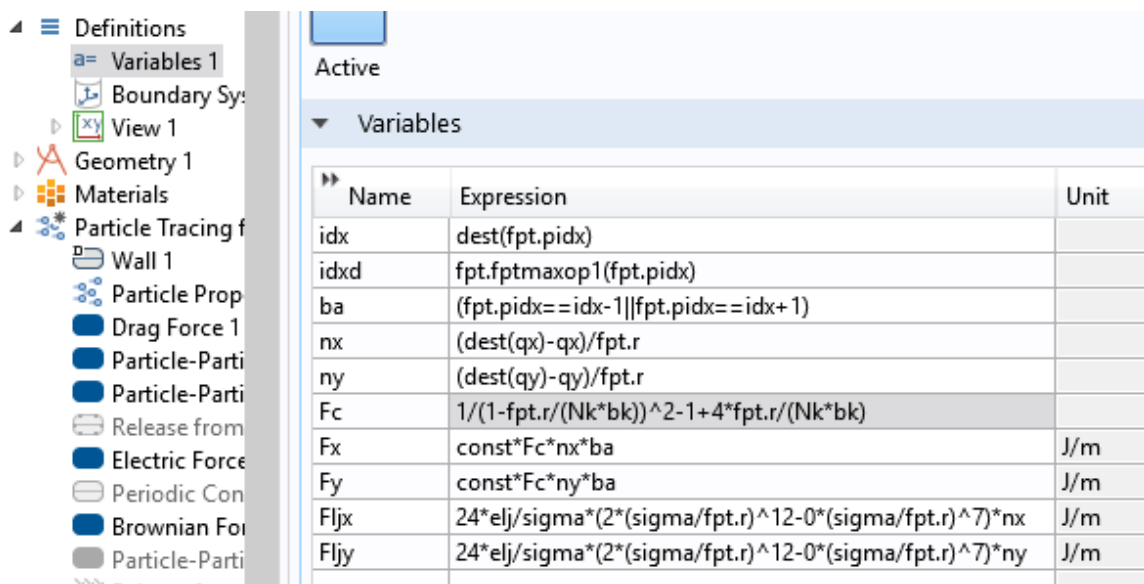
$$\nabla^2 \Phi = 0 \tag{9}$$

Here, the electric field of potential is denoted by Φ. The mesh was selected to be extremely fine considering the large height difference between the wide and narrow channels. While the time needed to calculate simulation results can be adversely affected by increasing the sensitivity of the mesh used, in this case it did not. The electrical field was created by applying a potential of V_0 and $-V_0$ at the two ends of the channel, while the rest of the walls were assumed to be insulated walls.

The Laminar Flow Physics of the Fluid Flow module and the Particle Tracking for Fluid Flow Physics of the Particle-Tracing module were selected to simulate a DNA molecule as a bead-spring model within a Newtonian fluid. The beads are represented as particles and are connected to each other by spring forces. There was no inlet or outlet fluid flow to the channel because DNA is moved only by the electric field, not by flow. Therefore, no slip boundary condition was given to all the walls. Particles, or beads, were assumed to be reflecting whenever they collided with the wall borders. This was done by

selection the bounce option in the Settings for the wall. Brownian and drag forces were

added to the module setting from the force options provided by the module. To couple the

existing electrical field with the main equation of the charged beads, the Electric Force

was added to the forces acting on the beads.

Spring force effect was defined by adding a custom Particle-Particle interaction to

the settings. Particle-Particle Interactions are effective for all present beads. Therefore,

the software does not discriminate between the beads and connects all existing beads with

springs. To avoid this, a custom condition was added to the equation that made the

software recognize the beads within its vicinity. Figure 3 summarizes how the custom

forces were implemented.

Figure 3. Screen capture of the Particle-Particle Interaction custom force definition. (Fx and Fy are spring force, Fljx and Fljy are excluded volume force).

Another custom Particle-Particle interaction was added to the settings to represent

the excluded volume force between the beads. A sort of modified Lennard-Jones equation

was employed in a package, the second term on the right-hand side of equation (7) was removed to prevent the beads from collapsing into each other during simulation.

The absolute error tolerance is a tricky parameter to define. Very large values will result in weak and inaccurate results (abs_err: 1e-6 – 1e-7), while choosing very small values for absolute error tolerance drastically extends the simulation time (abs_err< 2e-8).

5. EXPERIMENTAL RESULTS / SIMULATION RESULTS / DISCUSSION

We simulated the center-of-mass trajectory of N_b=2, 4 and 16 bead long DNA molecules flowing in the periodically constricted channel. The simulated trajectories of those DNA molecules traveling the same distance in the channel (from entering and exiting a larger channel) are shown in Figure 5. As expected from the electric field line in Figure 4, DNAs are moving faster in the narrow channels. As the DNA molecules are longer (more beads) the molecule moves faster. It is also observed that shorter (less beads) DNA molecules have nosier trajectories due to their stronger diffusivity. This indicates that the stronger diffusivity (Brownian force) of shorter DNA molecules slows their flowing through entropic trap channels by moving them off electric field lines.

Figure 6 compares the snapshots of a short (N_b=2) and a long (N_b=16) DNA flowing into and out of a wide channel in an entropic trap channel. It can be seen that the larger the surface area of a DNA molecule the more likely the molecule will be dragged into the smaller channel. These findings from our simulation agree with the findings observed in the study by Han et al. [2].
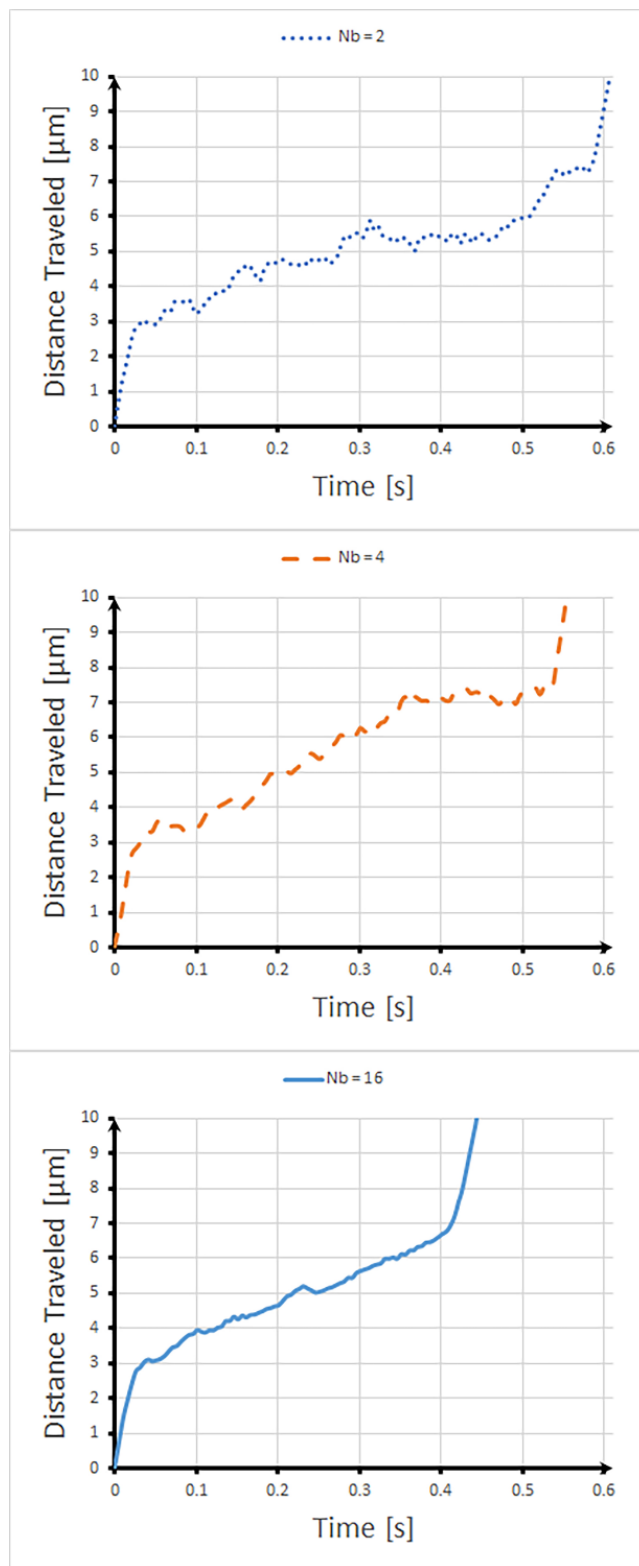
Figure 4. Simulated center-of-mass trajectories of DNA with Nb=2,4 and 16. The starting position and time is set when the center-of-mass of a DNA is passing at the center of a narrow channel.
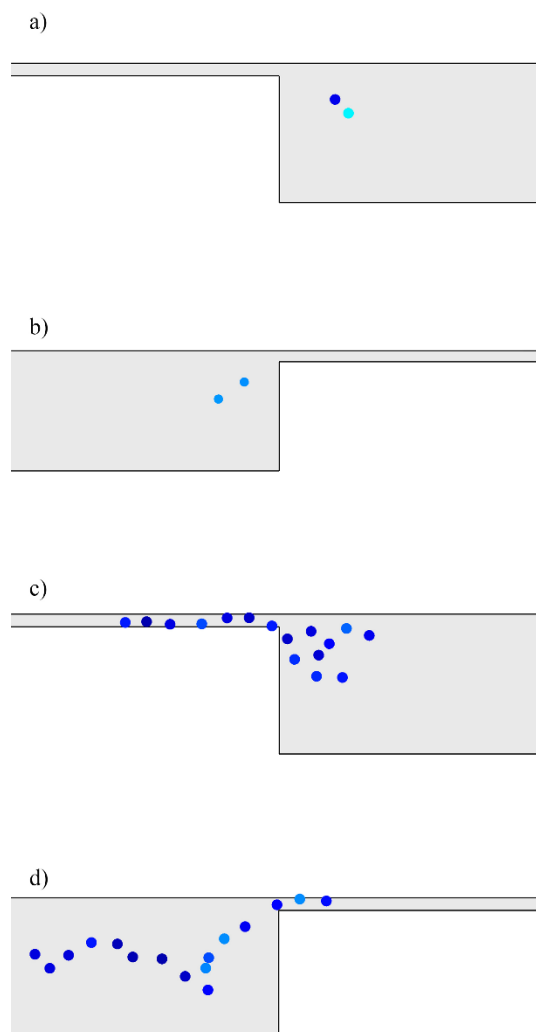
Figure 5. Snapshots of a shorter DNA molecule with Nb=2 and a longer DNA molecule with Nb=16, flowing into and out of a wide channel in an entropic trap channel: a) Nb = 2 at t = 0.040s, b) Nb = 2 at t = 0.55s, c) Nb =16 at t =0.025s, and d) Nb = 16 at t = 0.38s.

6. CONCLUSIONS

We successfully performed a Brownian coarse-grained bead-spring simulation of a λ-DNA molecule with various contour lengths in a periodically constricted channel using COMSOL Multiphysics®. The simulation results show good agreement with the previous results found by other researchers. To our knowledge, this is the first time that a

DNA molecule or a single polymer molecule has been simulated using COMSOL

Multiphysics®. It is expected that the computational time is expected to take much longer

for BD simulation of DNA with more beads. However, due to COMSOL's user-friendly

graphic user interface and the easy analysis tools, we believe that our simulation can be a

good example to be disseminated to the DNA dynamics research communities.

Moreover, nonuniform field calculations in complex geometries can be easily calculated

using COMSOL. This tends to be a time-consuming process in many other software

programs.

The equation of motion of the beads provided in the module contains the inertial

term $\frac{d(m_p v_i)}{dt}$, which is often neglected in typical microfluidic simulations. Therefore, our

simulation result is more accurate in a sense that the inertial effect is considered and an

extended simulation study for investigating the inertial effect can be possible.

Despite the good agreement of our results with previous results, there are some

aspects that can be improved. The inclusion of hydrodynamic interaction effects is still

challenging in FEM-based simulation [1]; including these forces would lead to a more

accurate simulation. The bead-wall collision force is based on the distance from the

center of the bead to the nearest wall surface. This needs to be improved to include the

distance between the bead surface and the wall. Finally, finding a way to include the

attractive force in the Leonard-Jones potential without making the model collapse within

itself should be investigated [2].

ACKNOWLEDGEMENTS

REFERENCES

[1]   Monjezi, S., Behdani, B., Palaniappan, M.B., Jones, J.D., Park, J., Computational Studies of DNA Separations in Micro-fabricated Devices: Review of General Approaches and Recent Applications, Advances in Chemical Engineering and Science, 7, 362-393 (2017).

[2]   2. Han, J., Craighead, H., Entropic trapping and sieving of long DNA molecules in a nanofluidic channel, Journal of Vacuum Science & Technology A: Vacuum, Surfaces, and Films, 17, 2142-2147 (1999).

[3]   Han, J., Craighead, H.G., Characterization and optimization of an entropic trap for DNA separation, Analytical Chemistry, 74, 394-401 (2002).

[4]   Streek, M., Schmid, F., Duong, T.T., Anselmetti, D., Ros, A., Two-state migration of DNA in a structured microchannel, Physical Review E, 71, 011905 (2005).

[5]   Moeendarbary, E., Ng, T., Pan, H., Lam, K., Migration of DNA molecules through entropic trap arrays: a dissipative particle dynamics study, Microfluidics and Nanofluidics, 8, 243-254 (2010).

[6]   Streek, M., Schmid, F., Duong, T.T., Ros, A., Mechanisms of DNA separation in entropic trap arrays: a Brownian dynamics simulation, Journal of Biotechnology, 112, 79-89 (2004).

[7]   Zhang, Y., de Pablo, J.J., Graham, M.D., An immersed boundary method for Brownian dynamics simulation of polymers in complex geometries: Application to DNA flowing through a nanoslit with embedded nanopits, The Journal of chemical physics, 136, 014901 (2012).

[8]   Tessier, F., Labrie, J., Slater, G.W., Electrophoretic separation of long polyelectrolytes in submolecular-size constrictions: a Monte Carlo study, Macromolecules, 35, 4791-4800 (2002).

[9]   Panwar, A.S., Kumar, S., Time scales in polymer electrophoresis through narrow constrictions: A Brownian dynamics study, Macromolecules, 39, 1279-1289 (2006).

[10]   Lee, Y.M., Joo, Y.L., Brownian dynamics simulations of polyelectrolyte molecules traveling through an entropic trap array during electrophoresis, The Journal of chemical physics, 127, 09B618 (2007).

[11]   Duong-Hong, D., Wang, J.-S., Liu, G., Chen, Y.Z., Han, J., Hadjiconstantinou, N.G., Dissipative particle dynamics simulations of electroosmotic flow in nano-fluidic devices, Microfluidics and Nanofluidics, 4, 219-225 (2008).

[12]   Fayad, G.N., Hadjiconstantinou, N.G., A brownian dynamics model of worm-like-biomolecule separation using periodic nanofilter arrays, in: ASME 2009 International Mechanical Engineering Congress and Exposition, American Society of Mechanical Engineers, pp. 391-397 (2009).

[13]   Fayad, G.N., Hadjiconstantinou, N.G., Realistic Brownian Dynamics simulations of biological molecule separation in nanofluidic devices, Microfluidics and Nanofluidics, 8, 521-529 (2010).

[14]   14. Fayad, G.N., Hadjiconstantinou, N.G., Modeling the electrophoretic separation of short biological molecules in nanofluidic devices, Journal of Fluids Engineering, 135, 024501 (2013).

[15]   Choi, S., Kim, J.M., Ahn, K.H., Lee, S.J., High-throughput DNA separation in nanofilter arrays, Electrophoresis, 35, 2068-2077 (2014).

[16]   Larson, R.G., The rheology of dilute solutions of flexible polymers: Progress and problems, Journal of Rheology, 49, 1-70 (2005).

[17]   Kim, J.M., Doyle, P.S., Brownian dynamics simulations of a DNA molecule colliding with a small cylindrical post, Macromolecules, 40, 9151-9163 (2007).

[18]   Jendrejack, R.M., Schwartz, D.C., De Pablo, J.J., Graham, M.D., Shear-induced migration in flowing polymer solutions: Simulation of long-chain DNA in microchannels, The Journal of chemical physics, 120, 2513-2529 (2004).

SECTION

2. CONCLUSION

For the first time, a systematic computational approach was introduced to obtain the average orientation of nanorods as a function of Pe (the ratio of shear rate over rotational diffusion) and distance from the channel wall. The method uses Brownian dynamics simulation results of the orientational moments of the particle as a one-time simulation technique. The method is later fitted into a mathematical model, which removes the need to repeat the simulation for a new condition and to produce any combination of the orientation average moments as a function of Pe and position of the particle in the channel. The results indicated strong agreement with previous reports of translational and rotational Brownian dynamics simulation.

In the second part, the model of the average orientation moments from the first part was used to obtain high aspect ratio (Ar>5) nanorods center-of-mass distribution model along the channel with a single hydrodynamic field. The model derivation was discussed in detail. The model was used to calculate the concentration profile of nanorods in a simple shear and a pressure-driven channel. Both of the results were compared to previously reported Brownian dynamics simulation data and showed good agreement.

In the third part, a model was derived for Field Fractionation of ellipsoidal nanorods in the range of low (1>Ar>5) and high (Ar>5) aspect ratio. Previous anomalies observed in nanorod elution experiment for the lower aspect ratio of nanorods were explained by our model. It was found that three distinct mechanisms may affect the rod distribution that could be explained by normal, steric-entropic and entropic modes. In the

normal mode, as expected the fastest elution of the particles was observed for the smaller particles, as well as particles with lower aspect ratio for the particles of the same size. In the Steric-entropic mode, it was discovered that the particles of an intermediate size, with higher aspect ratio eluted faster than those with lower aspect ratio. The elution order of different sizes of particles depends on the size and aspect ratio of the particles. The steric mode was observed for bigger particles and higher aspect ratio. In this mode, the particles with lower aspect ratio showed faster elution. Finally, our model was validated by results of a previously reported gold nanorod separation experiment.

A review of current challenges numerical DNA separation studies was completed. The recent advances and techniques were investigated. Suggestions were made to create possible new efficient ways of DNA separation. Subsequently, COMSOL Multiphysics®, was used to simulate DNA migration mechanism in a separation device (an array of entropic traps). It was observed that DNA chains with longer size, eluted faster than those with smaller chain size. The results of the simulation were successfully validated with previous experimental data.

3. RECOMMENDATIONS FOR FUTURE WORK

Successful accomplishment of Brownian dynamics simulation of nano-sized semi-flexible λ-DNA in an array of entropic traps using COMSOL Multiphysics® for the first time, paves the way for advancing simulation of DNA migration in more recent separation, sorting and stretching applications. Currently in our lab, Brownian simulation of DNA in a newly proposed DNA trapping and stretching device is advancing by taking advantage of electrophoretic and dielectrophoretic features of the molecule, with the assistance of an additional shear flow. Figure 3.1 shows a schematic view of the device. The electrodes are connected to a high-frequency (e.g., 5 MHz) AC voltage source, creating a time-dependent electric field. The electrodes are cast on a moving part that can be dragged inside the solution, creating a frag force field. Simulation of the DNA stretching is still ongoing.
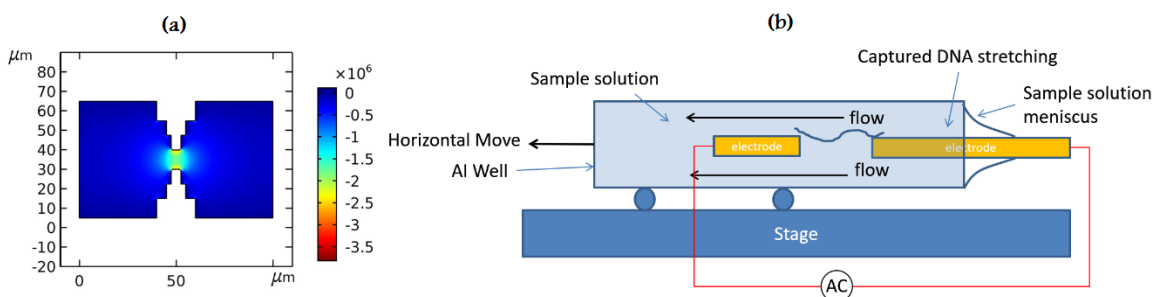
Figure 3.1. Electrophoretic DNA stretching: (a) the electrical field strength. (b) schematic view of the stretching device.

In another project, streamlines of an acoustic micro-bubble vortex flow are being numerically investigated, which so far has been developed for many purposes such as a micropump, micromixer, and microparticle separation. The schematic view of the device

is shown in Figure 3.2. A streaming vortex flow is created as a result of the piezoelectric

oscillation of the device. This research adopts 2D and 3D two-phase flow simulation

using the FEM method of COMSOL Multiphysics®, as well as the FVM method of

OPEN FOAM. In the next step, results of the simulation will be compared to existing

experimental data for validation [41, 42]. Simulation of the flow condition may have a

great contribution to the future design improvement of the device. As a future work, the

result of the simulation will be used to expand the separation capability of the acoustic

microbubble streaming flows to the separation of non-spherical particles.
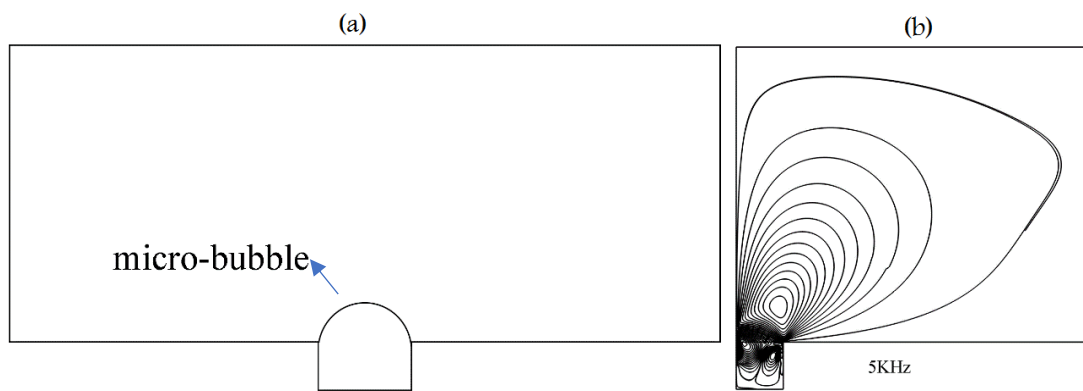

Figure 3.2. Micro-bubble simulation: (a) schematic view of an acoustic bubble streaming channel. (b) result from the simulation of a micro-bubble oscillation at the frequency of 5KHz.

REFERENCES

[1]   Kim, K., Jo, M.-C., Jeong, S., Palanikumar, L., et al., Externally controlled drug release using a gold nanorod contained composite membrane, Nanoscale 2016, 8, 11949-11955.

[2]   Alkilany, A. M., Thompson, L. B., Boulos, S. P., Sisco, P. N., Murphy, C. J., Gold nanorods: their potential for photothermal therapeutics and drug delivery, tempered by the complexity of their biological interactions, Advanced drug delivery reviews 2012, 64, 190-199.

[3]   Lee, J., Kang, B., Hicks, B., Chancellor Jr, T. F., et al., The control of cell adhesion and viability by zinc oxide nanorods, Biomaterials 2008, 29, 3743-3749.

[4]   Barua, S., Mitragotri, S., Challenges associated with penetration of nanoparticles across cell and tissue barriers: a review of current status and future prospects, Nano today 2014, 9, 223-243.

[5]   Shanmukh, S., Jones, L., Driskell, J., Zhao, Y., et al., Rapid and sensitive detection of respiratory virus molecular signatures using a silver nanorod array SERS substrate, Nano letters 2006, 6, 2630-2636.

[6]   Murphy, C. J., Gole, A. M., Hunyadi, S. E., Stone, J. W., et al., Chemical sensing and imaging with metallic nanorods, Chemical Communications 2008, 544-557.

[7]   [Wang, J., Sun, X., Yang, Y., Huang, H., et al., Hydrothermally grown oriented ZnO nanorod arrays for gas sensing applications, Nanotechnology 2006, 17, 4995.

[8]   Lee, S. W., Yabuuchi, N., Gallant, B. M., Chen, S., et al., High-power lithium batteries from functionalized carbon-nanotube electrodes, Nature nanotechnology 2010, 5, 531.

[9]   De las Casas, C., Li, W., A review of application of carbon nanotubes for lithium ion battery anode material, Journal of Power Sources 2012, 208, 74-85.

[10]   Li, W., Liang, C., Zhou, W., Qiu, J., et al., Preparation and characterization of multiwalled carbon nanotube-supported platinum for cathode catalysts of direct methanol fuel cells, The Journal of Physical Chemistry B 2003, 107, 6292-6299.

[11]   Yamada, T., Hayamizu, Y., Yamamoto, Y., Yomogida, Y., et al., A stretchable carbon nanotube strain sensor for human-motion detection, Nature nanotechnology 2011, 6, 296.

[12]   Tofighy, M. A., Mohammadi, T., Adsorption of divalent heavy metal ions from water using carbon nanotube sheets, Journal of hazardous materials 2011, 185, 140-147.

[13]   Kelly, K. L., Coronado, E., Zhao, L. L., Schatz, G. C., ACS Publications 2003.

[14]   Behdani, B., Monjezi, S., Carey, M. J., Curtis G. Weldon, et al., Shape-based separation of micro-/nanoparticles in liquid phases, Biomicrofluidics 12, 051503 2018.

[15]   Caldorera-Moore, M., Guimard, N., Shi, L., Roy, K., Designer nanoparticles: incorporating size, shape and triggered release into nanoscale drug carriers, Expert opinion on drug delivery 2010, 7, 479-495.

[16]   Ahmadi, T. S., Wang, Z. L., Green, T. C., Henglein, A., El-Sayed, M. A., Shape-controlled synthesis of colloidal platinum nanoparticles, Science 1996, 272, 1924-1925.

[17]   Li, M., Schnablegger, H., Mann, S., Coupled synthesis and self-assembly of nanoparticles to give structures with controlled organization, Nature 1999, 402, 393.

[18]   IWAI, N., NAGAI, K., WACHI, M., Novel S-benzylisothiourea compound that induces spherical cells in Escherichia coli probably by acting on a rod-shape-determining protein (s) other than penicillin-binding protein 2, Bioscience, biotechnology, and biochemistry 2002, 66, 2658-2662.

[19]   Shiomi, D., Sakai, M., Niki, H., Determination of bacterial rod shape by a novel cytoskeletal membrane protein, The EMBO journal 2008, 27, 3081-3091.

[20]   Ausserré, D., Edwards, J., Lecourtier, J., Hervet, H., Rondelez, F., Hydrodynamic thickening of depletion layers in colloidal solutions, EPL (Europhysics Letters) 1991, 14, 33.

[21]   Agarwal, U., Dutta, A., Mashelkar, R., Migration of macromolecules under flow: the physical origin and engineering implications, Chemical Engineering Science 1994, 49, 1693-1717.

[22]   Schiek, R. L., Shaqfeh, E. S., Cross-streamline migration of slender Brownian fibres in plane Poiseuille flow, Journal of Fluid Mechanics 1997, 332, 23-39.

[23]   Park, J., Bricker, J. M., Butler, J. E., Cross-stream migration in dilute solutions of rigid polymers undergoing rectilinear flow near a wall, Physical Review E 2007, 76, 040801.

[24]   Park, J., Mittal, A., An improved model for the steric-entropic effect on the retention of rod-like particles in field-flow fractionation: Discussion of aspect ratio-based separation, Chromatography 2015, 2, 472-487.

[25]   De Pablo, J. J., Öttinger, H. C., Rabin, Y., Hydrodynamic changes of the depletion layer of dilute polymer solutions near a wall, AIChE journal 1992, 38, 273-283.

[26]   Messaud, F. A., Sanderson, R. D., Runyon, J. R., Otte, T., et al., An overview on field-flow fractionation techniques and their applications in the separation and characterization of polymers, Progress in Polymer Science 2009, 34, 351-368.

[27]   Williams, P. S., Carpino, F., Zborowski, M., Characterization of magnetic nanoparticles using programmed quadrupole magnetic field-flow fractionation, Philosophical Transactions of the Royal Society of London A: Mathematical, Physical and Engineering Sciences 2010, 368, 4419-4437.

[28]   Giddings, J. C., Nonequilibrium theory of field-flow fractionation, The journal of chemical physics 1968, 49, 81-85.

[29]   Kowalkowski, T., Buszewski, B., Cantado, C., Dondi, F., Field-flow fractionation: theory, techniques, applications and the challenges, Critical reviews in analytical chemistry 2006, 36, 129-135.

[30]   Nguyen, T. M., Liu, J., Hackley, V. A., Fractionation and characterization of high aspect ratio gold nanorods using asymmetric-flow field flow fractionation and single particle inductively coupled plasma mass spectrometry, Chromatography 2015, 2, 422-435.

[31]   Johnson, K. W., Reproducible electrodeposition of biomolecules for the fabrication of miniature electroenzymatic biosensors, Sensors and Actuators B: Chemical 1991, 5, 85-89.

[32]   Grossman, P. D., Soane, D. S., Capillary electrophoresis of DNA in entangled polymer solutions, Journal of Chromatography A 1991, 559, 257-266.

[33]   Stellwagen, N. C., Nucleic acid electrophoresis, Springer 1998, pp. 1-53.

[34]   Han, J., Craighead, H. G., Separation of long DNA molecules in a microfabricated entropic trap array, Science 2000, 288, 1026-1029.

[35]   Bader, J. S., Hammond, R. W., Henck, S. A., Deem, M. W., et al., DNA transport by a micromachined Brownian ratchet device, Proceedings of the National Academy of Sciences 1999, 96, 13165-13169.

[36]   Monjezi, S., Jones, J. D., Nelson, A. K., Park, J., The Effect of Weak Confinement on the Orientation of Nanorods under Shear Flows, Nanomaterials 2018, 8, 130.

[37]   Monjezi, S., Patterson, G. K., Nelson, A. K., Park, J., A Model for the Depletion Layer Prediction in a Dilute Suspension of Rigid Rod-like Particles under Shear Flows in the Entire Range of Peclet Numbers, Chemical Engineering Science 189, 394-400 2018.

[38]   Monjezi, S., Schneier, M., Choi, J., Lee, S., Park, J., The shape effect on the retention behaviors of ellipsoidal particles in field-flow fractionation: theoretical model derivation considering the steric-entropic mode, Chromatography A (Accepted) 2018.

[39]   Monjezi, S., Behdani, B., Palaniappan, M. B., Jones, J. D., Park, J., Computational studies of DNA separations in micro-fabricated devices: Review of general approaches and recent applications, Advances in Chemical Engineering and Science 2017, 7, 362.

[40]   Monjezi, S., Palaniappan, M. B., Jones, J. D., Behdani, B., Park, J., Proceedings of 2017 COMSOL Conference in Boston, Boston 2017, pp. 4-6.

[41]   Zhou, R., Wang, C., Acoustic bubble enhanced pinched flow fractionation for microparticle separation, Journal of Micromechanics and Microengineering 2015, 25, 084005.

[42]   Wang, C., Jalikop, S. V., Hilgenfeldt, S., Efficient manipulation of microparticles in bubble streaming flows, Biomicrofluidics 2012, 6, 012801.

[43]   Mead, D. W.; Monjezi, S.; Park, J. A constitutive model for entangled polydisperse linear flexible polymers with entanglement dynamics and a configuration dependent friction coefficient. Part II. Modeling "shear modification" following cessation of fast shear flow, Journal of Rheology 2018 62(1), 135-147

[44]   Mead, D. W.; Monjezi, S.; Park, J. A constitutive model for entangled polydisperse linear flexible polymers with entanglement dynamics and a configuration dependent friction coefficient. Part I: Model derivation, Journal of Rheology 2018 62(1), 121-134

VITA

Saman Monjezi is a Chemical Engineer born in Ahvaz, Iran. He received his Bachelor's degree in Chemical Engineering from Razi University, and his Master's Degree in Chemical Engineering from Sharif University of Technology, Tehran, Iran. He has more than 3 years of work experience in petrochemical and gas industries as an operations/process engineer. In Fall 2014, he started his PhD program in Chemical Engineering at Missouri University of Science and Technology. He joined Dr. Joontaek Park's group in Spring 2016. His main research has been focused on non-spherical nano/microparticle modeling and simulation in microfluidic devices since then. However, he had contributions to many other fields. He has published several research papers since he started his PhD at Missouri University of Science and Technology.

In May 2019, he received his Ph.D. under the direction of Dr. Joontaek Park in Chemical Engineering from Missouri University of Science and Technology, Rolla, Missouri, USA.